



O'Hare, Lynne (2008) Continuum Simulation of Fluid Flow and Heat Transfer in Gas Microsystems. PhD thesis, University of Strathclyde.

<http://eprints.cdlr.strath.ac.uk/6501/>

This is an author-produced version of an unpublished thesis.

Strathprints is designed to allow users to access the research output of the University of Strathclyde. Copyright © and Moral Rights for the papers on this site are retained by the individual authors and/or other copyright owners. You may not engage in further distribution of the material for any profitmaking activities or any commercial gain. You may freely distribute both the url (<http://eprints.cdlr.strath.ac.uk>) and the content of this paper for research or study, educational, or not-for-profit purposes without prior permission or charge. You may freely distribute the url (<http://eprints.cdlr.strath.ac.uk>) of the Strathprints website.

Any correspondence concerning this service should be sent to The Strathprints Administrator: eprints@cis.strath.ac.uk

University of Strathclyde

Department of Mechanical Engineering

**Continuum simulation of fluid flow and
heat transfer in gas microsystems**

Lynne O'Hare M.Eng.

2008

A thesis presented in fulfilment
of the requirements of the degree of
Doctor of Philosophy

Declaration of Author's Rights

The copyright of this thesis belongs to the author under the terms of the United Kingdom Copyright Acts as qualified by University of Strathclyde Regulation 3.49. Due acknowledgement must always be made of the use of any material contained in, or derived from, this thesis.

Abstract

The behaviour of gas flows in microscale systems cannot be adequately represented by the Navier-Stokes-Fourier (N-S-F) equations of macroscale fluid dynamics. The key flow features that cannot typically be replicated by continuum-based methods are discontinuities of energy and momentum at system boundaries, known as velocity slip and temperature jump, and the Knudsen layer, a region of flow close to boundary interfaces where the gas and the surface are not in local thermodynamic equilibrium. In this thesis, fluid flow and heat transfer in gas microsystems are simulated numerically using an extended form of the N-S-F relations, which incorporates these non-equilibrium effects.

Constitutive scaling is a phenomenological approach that alters the linear constitutive relationships of the N-S-F shear stress and heat flux closures to incorporate Knudsen layer effects in microflow simulations. This method has been implemented here in a 3D finite-volume numerics package. The aim of the present work is to make use of the constitutive scaling method to produce a computational tool suitable for analysing microscale flows. Both incompressible and compressible numerical solvers featuring constitutive scaling models and a range of appropriate boundary conditions have been developed to this end. Verification and validation processes have been undertaken, comparing the performance of the numerical models to analytical solutions, discrete molecular simulations and experimental results for key engineering case studies.

A detailed assessment of the implications of extending the constitutive scaling method to fully compressible flows has also been carried out. As a result of this study, a new methodology for defining constitutive scaling functions empirically has been produced. The methodology has shown, for a simple test case, that Knudsen layer features can be incorporated in continuum simulations using scaling functions based on the local features of a flow configuration, rather than a global scaling function curve-fit to theoretical data for a single type of case.

Acknowledgements

The author would like to thank supervisors J.M. Reese and T.J. Scanlon for guidance and support throughout this project. Work carried out by D.A. Lockerby, Y. Zheng and C.J. Greenshields that has facilitated this research is also gratefully acknowledged. The work was funded by the Engineering and Physical Sciences Research Council under Grant No. GR/S77196/01.

Contents

Abstract	ii
Contents	iv
List of Figures	viii
List of Tables	xiv
Nomenclature	xv
1 Introduction	1
1.1 Motivation	1
1.2 Rarefied flows	2
1.2.1 Continuum-equilibrium	3
1.3 Scope of this research	5
1.3.1 Availability of data	7
1.4 Outline of thesis	9
2 Modelling rarefied gases	12
2.1 Characterising gas rarefaction	12
2.2 Approaches to modelling rarefied flows	16
2.2.1 Kinetic theory of gases	16
2.2.2 Discrete molecular models — DSMC	18
2.2.3 The Chapman-Enskog expansion	20
2.2.4 Moment models	21

2.2.5	Extending the Navier-Stokes-Fourier equations	22
2.2.6	Summary	24
3	Physics of rarefied flows	26
3.1	Interfacial phenomena	26
3.1.1	Maxwell’s phenomenological model	28
3.1.2	Phenomenological model vs. physical behaviour	33
3.1.3	Boundary effects on temperature	35
3.1.4	Alternative slip and jump models	38
3.2	The Knudsen layer	40
4	Constitutive scaling	44
4.1	Introduction	44
4.1.1	State of the art	47
4.2	OpenFOAM: a CFD framework	52
4.3	Incompressible solver: icoFoam	52
4.3.1	Boundary conditions	54
4.4	OpenFOAM for non-equilibrium flows	54
4.4.1	Implementing effective viscosity	56
4.4.2	Maxwell’s slip and constitutive scaling	57
4.5	Progress summary	58
5	Incompressible flows	60
5.1	Introduction	60
5.2	Poiseuille flow	61
5.2.1	Verifying numerical results	64
5.3	Couette flow	71
5.3.1	Verifying numerical results	74
5.3.2	Validating numerical results	77
5.4	Constricted channels	79
5.4.1	Validating numerical results	82

5.4.2	Extending the analysis	88
5.5	Cylindrical Couette flow	91
5.6	Summary	94
6	Compressible flows	96
6.1	Introduction	96
6.2	Compressible solvers in OpenFOAM	97
6.2.1	Compressible solver: rhoPsonicFoam	98
6.2.2	Modified solver: rhoPEsonicFoam	100
6.2.3	Compressible microflows solver	105
6.3	Constitutive scaling models	106
6.3.1	Model A	106
6.3.2	Model B	107
6.4	Half-space problems	110
6.4.1	Kramers' problem	110
6.4.2	The temperature jump problem	112
6.4.3	Summary	114
6.5	Compressible micro-Couette flow	115
6.5.1	Discussion	121
6.5.2	Summary	126
7	A new approach to constitutive-scaling	128
7.1	Identifying a scaling function	129
7.2	Extracting effective viscosity	135
7.3	Incorporating Kn	138
7.4	Discussion	142
7.4.1	Scope for future work	144
7.4.2	Summary	146
8	Conclusions	148
8.1	Research contributions	153

8.2 Scope for future work	155
Appendices	157
A Analytical solutions: Poiseuille flow	157
A.1 Poiseuille flow	157
B Slip-flow in Fluent	162
B.1 Mean free path calculation	162
B.2 Boundary condition accuracy	163
B.3 Maxwell's slip condition	165
C Analytical solutions: Couette flow	168
D Microflows in Matlab	173
D.1 Couette flow	174
D.2 Poiseuille flow	176
References	177

List of Figures

2.1	Example of a Maxwellian distribution of molecular velocities in a 1D case. The most probable molecular velocity is the average value, with probability decreasing towards the maximum and minimum velocities.	13
2.2	Gas flow regimes classified by Knudsen number; A represents fully continuous flow, B slip/jump flow, C transitional behaviour and D free molecular flow.	14
3.1	Molecular interaction across a plane S , which gives rise to shear stress in the gas; and similar molecular interaction in the near-wall Knudsen layer region, where both incident and reflected “streams” of molecules interact.	26
3.2	Schematic of the velocity structure of the Knudsen layer near a wall in a pressure-driven flow, comparing different types of slip boundary condition.	41
4.1	Sketch of Kramers’ problem flow configuration showing applied constant shear stress, τ ; traditional, no-slip N-S solution (u_{wall} : dotted line), N-S solution with second order macroslip boundary condition (u_{slip}^{**} : dashed line) and true velocity profile (u_{slip} : solid line). The Knudsen layer extends approximately 2λ from the wall surface.	45
5.1	Schematic of Poiseuille flow configuration with velocity profile. . .	61

5.2	Analytical and numerical (microIcoFoam) Navier-Stokes solutions for no-slip Poiseuille flow at any Kn (standard no-slip Navier-Stokes solutions do not change with increasing Kn .)	65
5.3	OpenFOAM results including Maxwell slip compared to analytical results from Eq. (5.3) for Poiseuille flow at $Kn = 0.0035$. Inset: a close-up of the near-wall region highlighting the agreement between the two profiles for slip at the channel wall.	66
5.4	Verification of agreement between OpenFOAM simulations with Maxwell's slip boundary condition and Eq. (5.3) at various Kn values.	67
5.5	OpenFOAM results including constitutive scaling compared to analytical results from Eq. (5.4) for Poiseuille flow at $Kn = 0.035$. Inset: a close-up of the near-wall region highlighting the agreement between the two profiles at the channel wall.	69
5.6	Verification of agreement between OpenFOAM simulations with constitutive scaling and Eq. (5.4) at various Kn values.	70
5.7	Poiseuille flow results: comparison of OpenFOAM using Maxwell's slip boundary condition with OpenFOAM using constitutive scaling.	70
5.8	Schematic of Couette flow configuration with velocity profile.	71
5.9	Verification of agreement between OpenFOAM simulations with Maxwell's slip boundary condition and Eq. (5.9) at various Kn values.	75
5.10	Verification of agreement between OpenFOAM simulations with constitutive scaling and Eq. (5.11) at various Kn values.	76
5.11	Comparison of OpenFOAM results for Couette flow with Maxwell's slip boundary condition with OpenFOAM results for constitutive scaling. The top figure shows the velocity across the whole channel, and the bottom figure the velocity in the upper half of the channel only.	78

5.12	Constitutive scaling results from microIcoFoam compared to Navier-Stokes solutions with Maxwell’s slip condition and to DSMC results.	80
5.13	Microchannel orifice constriction geometry.	81
5.14	Microchannel venturi constriction geometry.	81
5.15	Centreline pressures in a channel with an orifice-plate constriction compared to experimental data.	83
5.16	Centreline pressures in a channel with a venturi constriction compared to experimental data.	84
5.17	Centreline pressures in the near-constriction region through venturi constrictions in rectangular channels as throat height h_t decreases, compared to experimental data.	84
5.18	Mass flowrates through constricted microchannels: OpenFOAM results for constitutive scaling and Navier-Stokes equations compared to experimental results.	85
5.19	Schematic of low-speed viscous flow through venturi-type and orifice constrictions.	87
5.20	Velocity profiles close to the throat wall for an orifice-plate constriction. Standard no-slip Navier-Stokes results are compared to results with Maxwell’s slip boundary condition applied and to constitutive scaling with microslip.	87
5.21	Centreline pressures in the near-constriction region through venturi constrictions in rectangular channels as throat height h_t decreases: constitutive scaling results only.	89
5.22	Maximum velocity magnitude for orifice-plate constrictions as throat height h_t varies.	90
5.23	Schematic of Couette flow between concentric cylinders.	93

5.24	Velocity profiles in cylindrical Couette flow non-dimensionalised by the tangential velocity of the inner cylinder. Comparison of no slip ($\cdot \cdot \cdot$), conventional slip ($- -$), Maxwell's original slip ($- \cdot -$), constitutive-scaling in CFD ($—$) and DSMC data (\circ).	94
6.1	Effective viscosities provided by the scaling models, compared to (constant) nominal viscosity.	109
6.2	Effective thermal conductivities provided by the scaling models, compared to (constant) nominal thermal conductivity.	110
6.3	Ratio of effective viscosity to effective thermal conductivity (ratio of momentum to energy diffusivity) provided by the scaling models.	111
6.4	Knudsen layer shape defect predicted for Kramers' problem: kinetic theory data (points connected by solid line) compared to model A (dashed line) and model B (dotted line).	113
6.5	Schematic of the temperature jump problem showing constant applied heat flux, q ; traditional, no-jump N-S-F solution (T_{wall} : dotted line), N-S-F solution with second order macro-jump boundary condition (T_{jump}^{**} : dashed line) and true temperature profile (T_{jump} : solid line).	114
6.6	Knudsen layer shape defect predicted for the temperature jump problem: kinetic theory data (points connected by solid line) compared to model A (dashed line) and Model B (dotted line).	115
6.7	Couette flow configuration and nomenclature for the compressible CFD analysis; $\mathbf{U}_{Ma=1}$ is the velocity applied to move the lower wall at the local speed of sound.	117
6.8	Micro-Couette velocity profiles predicted by model A, Model B and DSMC for $Kn = 0.1$	119
6.9	Micro-Couette temperature profiles predicted by model A, Model B and DSMC for $Kn = 0.1$	120

6.10	Compressible micro-Couette flow velocity profiles; comparison of model A results (lines) to DSMC data (points).	121
6.11	Compressible micro-Couette flow temperature profiles predicted by model A.	122
6.12	Temperature profiles predicted by model A, with high- Kn results.	124
6.13	Temperature profiles predicted by model A; results as Kn increases while $\sigma_U = \sigma_T = 0.8$	125
6.14	Predicted temperature (in K) at the centre of the channel in compressible micro-Couette flow (i.e. the maximum temperature), plotted against Knudsen number.	127
7.1	Schematic of an ellipse showing its centre (x_0, y_0) , major axis a and minor axis b	131
7.2	Velocity profiles from three newly proposed elliptical constitutive-scaling models for Poiseuille flow in a microchannel where $Kn = 0.1$. Position y across the channel is non-dimensionalised by the half-channel height.	134
7.3	Elliptical model 1 compared to a Navier-Stokes solution with slip boundary conditions and the constitutively scaled Navier-Stokes profile given by Eq. (5.4), for Poiseuille flow in a microchannel where $Kn = 0.1$. Position y across the channel is non-dimensionalised by the half-channel height.	135
7.4	Elliptical model 2 compared to a Navier-Stokes solution with slip boundary conditions and the constitutively scaled Navier-Stokes profile given by Eq. (5.4), for Poiseuille flow in a microchannel where $Kn = 0.1$. Position y across the channel is non-dimensionalised by the half-channel height.	136

7.5	Elliptical model 3 compared to a Navier-Stokes solution with slip boundary conditions and the constitutively scaled Navier-Stokes profile given by Eq. (5.4), for Poiseuille flow in a microchannel where $Kn = 0.1$. Position y across the channel is non-dimensionalised by the half-channel height.	137
7.6	Effective viscosity for the three elliptical scaling models compared to the effective viscosity of the original constitutive scaling model. Position y across the channel is non-dimensionalised by the half-channel height.	138
7.7	Errors between velocity profiles of elliptical scaling models and Eq. (5.4) for $Kn = 0.1$, shown at non-dimensional positions across half a microchannel whose wall is positioned at $y = 0$	140
7.8	Errors between velocity profiles of elliptical scaling models and Eq. (5.4) for $Kn = 0.075$, shown at non-dimensional positions across half a microchannel whose wall is positioned at $y = 0$	141
7.9	Average percentage error between velocity profiles from three elliptical scaling models and Eq. (5.4), shown versus Knudsen number, Kn	142
B.1	Schematic of typical near-wall cell in 2D CFD.	164
B.2	Top: sketch of a typical near-wall velocity profile returned by Fluent. In the nearest cell to the wall, the velocity gradient is always manipulated in order to return the velocity of the fluid at the wall, u_{gas} , to the wall velocity, u_{wall} . This is incorrect — the gas at the wall should be assigned the calculated slip velocity u_{slip} . Bottom: arrangement of near-wall cells corresponding to the sketched velocity profile, with cell-centre positions marked.	166

List of Tables

5.1	Variation of channel height, length and applied pressure gradient for Poiseuille flow verification cases. Channel dimensions are given in m , and the pressure gradient is specified in N/m^3	65
5.2	Variation of channel height, length and wall velocities for Couette flow verification cases. Channel dimensions are given in m and wall velocities are given in m/s	74
5.3	Variation of Knudsen number with throat height for a pressure drop of $99.63kPa$ across the channel.	89
6.1	Coefficients used in Eqs. (6.18) and (6.19) to define the scaling functions of model B.	108
6.2	Table of channel heights used to vary Kn in Couette flow simulations, with corresponding Reynolds numbers for each case.	117

Nomenclature

Latin symbols

A_1	First-order velocity slip coefficient
A_2	Second-order velocity slip coefficient
A_{jump}	Temperature jump coefficient
$A_{KP,TJ}$	Scaling coefficient
A_{slip}	Velocity slip coefficient
$[A]$	Matrix of coefficients
$C(f)$	Collision integral
$C_{1,2}$	Constants of integration
D	Diffusive coefficient
D_e	Heat adsorption
$D_{KP,TJ}$	Scaling coefficient
E	Energy
$E_{KP,TJ}$	Scaling coefficient
\mathbf{F}	Body force
H	Channel height
$I(n/\lambda)$	Velocity correction function
Kn	Knudsen number
Kn_o	Outlet Knudsen number
L	Characteristic length scale of a system
Ma	Mach number
P_i	Inlet pressure

P_o	Outlet pressure
Pr	Prandtl number
Q	Heat flux vector at the wall
R	Specific gas constant
Re	Reynolds number
S	Co-ordinate plane
S_f	Surface area of cell face
S_h	Energy sources
S_M	Momentum sources
$S(n/\lambda)$	Shape defect
T	Temperature
$T_{1,2}$	Wall temperatures
T_{jump}	Temperature jump
\hat{T}	Dimensionless temperature
T_{jump}^*	Temperature jump
T_{jump}^{**}	Temperature jump with fictitious jump coefficient
T_r	Reference temperature
T_w	Wall temperature
T_{wall}	Wall temperature
U	Velocity
U^T	Transpose of velocity
U_{Ma=1}	Velocity at local speed of sound
a	Constant — sec. 4.1.1
	Major axis of an ellipse — sec. 7.1
$a_{1,2,n}$	Chapman-Enskog coefficients
b	Constant — sec. 4.1.1
	Minor axis of an ellipse — sec. 7.1
[b]	Matrix of boundary values
c	Constant

c_1	Local speed of sound
c_p	Specific heat at constant pressure
c_v	Specific heat at constant volume
d_c	Constriction depth
e	Internal energy
f	Distribution function
f_M	Maxwellian distribution function
$f(u_{el})$	Functional proportion of an ellipse
$f(n/\lambda)$	Scaling function for viscosity
$f(n/\lambda_{\text{original}})$	Scaling function for mean free path
h	Half-height of rectangular channel — ch. 5 Full channel height of constricted channel — sec. 5.4 Separation between rotating cylinders — sec. 5.5
h_0	Total enthalpy
h_c	Constriction height
h_t	Throat height
\mathbf{i}_n	Unit vector normal to and away from a wall
k	Thermal conductivity
k_B	Boltzmann constant
l	Longitudinal channel length
m	Mass of gas molecule
\dot{m}	Mass flowrate
n	Normal distance from nearest surface
p	Pressure
\hat{p}	Dimensionless pressure
p_d	Dynamic pressure
$p_{\langle ij \rangle}$	Stress
\mathbf{q}	Heat flux
q_i	Heat flux

\mathbf{r}	Spatial position
r_i	Inner radius
r_o	Outer radius
t	Time
\mathbf{u}	Velocity
\mathbf{u}_{slip}	Gas velocity at wall surface
\mathbf{u}_{wall}	Velocity of wall surface
u	Velocity component in x -direction
$u_{1,2}$	Wall velocities — ch. 6
$u_{1,2,3}$	Velocity produced by model 1, 2, 3 — sec. 7.1
u_{el}	“Velocity” corresponding to major axis of an ellipse
u_c	Cell-centre gas velocity — app. B
u_g	Local reference gas velocity
	Gas velocity at first cell boundary — app. B
u_i	Velocity at i^{th} node — app. B
u_n	Gas velocity normal to the wall
$u_{\text{N-S}}$	Navier-Stokes velocity result, no-slip
u_{slip}	Slip velocity
u_{total}	Composite velocity profile
u_w	Gas velocity at wall surface
u_x	Component of slip velocity in x -direction
\hat{u}	Dimensionless velocity
u_{slip}^*	First-order velocity slip
u_{slip}^{**}	Second-order velocity slip
$[u]$	Matrix of velocities
\mathbf{v}	Velocity
v	Velocity component in y -direction
\bar{v}	Mean molecular speed
w	Velocity component in z -direction

x	Co-ordinate direction Channel length in x -direction — ch. 5
x_0	Origin co-ordinate in x
y	Co-ordinate direction
y_0	Origin co-ordinate in y
\hat{y}	Dimensionless position in y -direction
z	Co-ordinate direction Channel depth — sec. 5.4
$\mathbf{1}$	Identity tensor

Greek symbols

Γ_n	Number of molecules per unit time
Π	Stress tensor at wall surface
Φ	Dissipation function
$\Omega_{1,2,3}$	Scaling coefficient for model 1, 2, 3
α	Constant
β	Kinetic-theory function
γ	Specific heat ratio
δ	Half-cell width
ϵ	Energy
ζ_{jump}	Temperature jump coefficient
ζ_{slip}	Velocity slip coefficient
η	Number density of molecules
θ	Macroscopic variable in local Kn definition
κ	Thermal conductivity
κ_{eff}	Effective thermal conductivity
κ_{eff_A}	Effective thermal conductivity, Model A

$\kappa_{\text{eff}B}$	Effective thermal conductivity, Model B
λ	Equilibrium mean free path of a gas
λ_F	Lennard-Jones mean free path of a gas
λ_{eff}	Effective mean free path
$\lambda_{\text{original}}$	Original mean free path
μ	Dynamic viscosity
μ_1	Dynamic viscosity at wall surface
μ_{eff}	Effective viscosity
$\mu_{\text{eff}A}$	Effective viscosity, Model A
$\mu_{\text{eff}B}$	Effective viscosity, Model B
$\hat{\mu}$	Dimensionless dynamic viscosity
ν	Kinematic viscosity
	Exponent of inverse power law — sec. refsoa
ξ	Constant
ρ	Density
σ	Retained proportion of tangential momentum
	Lennard-Jones characteristic length scale — app. B
σ_T	Thermal accommodation coefficient
σ_U	Tangential momentum accommodation coefficient
$\boldsymbol{\tau}$	Tangential shear stress
$\boldsymbol{\tau}_{\text{mc}}$	Shear stress with multiple components of velocity
τ	Shear stress
τ_w	Wall shear stress
ϕ	Diameter of hard-sphere molecule
	Mass flux in OpenFOAM
$\phi_{1,2,3}$	Viscosity-scaling function for model 1, 2, 3
$\omega_0(\nu)$	Tabulated value from kinetic theory

Chapter 1

Introduction

Gas flows in microscale systems display behaviour that cannot be replicated with the governing equations of classical fluid dynamics, the Navier-Stokes-Fourier equations (N-S-F). This thesis details how the N-S-F equation set can be modified to model microscale gas flows successfully, and demonstrates, for the first time, that such an approach can be fully integrated into mainstream computational fluid dynamics (CFD). It also describes a new type of modification for the governing equations that is a generalised and extended alternative to previously available models.

1.1 Motivation

Gas microflows can now be found in a wide variety of applications, from small-sample testing equipment for biomedical research through to microscale sensors and actuators for the aerospace industry. Microscale shear flows occur in oscillatory systems such as comb drives, and even in optical applications where microscale mirrors are moved to redirect signals. In these applications, the drag forces experienced by systems can be very poorly predicted by classical fluid dynamics, leading to the malfunction and eventual failure of moving parts. Pressure-driven microflows are also common, with banks of micro-thrusters employed in low-mass satellite propulsion systems, and microscale flow-measurement devices being produced that would benefit from better design-phase calibration. The

inability of the N-S-F equations to accurately predict mass flowrate in these devices requires large margins of error to be employed in the engineering design of gas microsystems, limiting efficiency. There is also interest in replacing chemical batteries in portable electronic equipment with microscale power plants, a particularly interesting application that serves as an illustration of how macroscale physics cannot always be translated directly to smaller-scale systems [1].

Generally, microdevices are manufactured using mature technology originally developed for the electronics industry, and it is possible for intricate 3D geometries and complex multiphysics systems to be produced quickly and effectively. The design of small-scale systems is uniquely challenging, however, as many of the assumptions underpinning classical macroscale physics do not hold for microflows.

To illustrate, a truly general model for gas microflows would need to represent many unusual flow features, including local departures from the macroscopic second law of thermodynamics, dominant surface effects, and, under certain circumstances, velocity and temperature profiles completely inverse to those predicted by macroscopic methods. Although a large body of academic research has already been conducted dedicated to understanding the physics of microsystems, very few robust engineering models exist, and trial-and-error approaches are still used to design commercial products in many cases. Inefficient, and often ineffectual, devices are a common result. In order to improve industrial design in the short-to-medium term future, this thesis integrates new and innovative continuum models into the CFD package OpenFOAM, to produce an engineering analysis tool for gas microsystems with capabilities comparable to those available for macroscale design work.

1.2 Rarefied flows

The primary cause of the unusual, and at times counter-intuitive, behaviour observed in microscale flows is gas rarefaction. This occurs as the molecular mean free path of a gas in a system, the average distance a particle travels between

collisions with other particles, approaches the order of the physical dimensions of that system. As the flow becomes rarefied the gas ceases to act as a single continuous fluid, and begins to behave as a collection of discrete particles. There are two common causes of rarefaction: either it occurs in the case of decreasing density of the gas, or, as in microsystems, when the physical device dimensions are sufficiently small. In microscale devices, the density of the gas can remain unchanged, but only a relatively small number of molecules is found inside these low-volume systems. Also, the mean free path begins to approach the order of the physical dimensions of microsystems. For example, a microscale pipe system carrying air at atmospheric conditions would have a mean free path of approximately $0.06\mu\text{m}$. This represents a difference of only two orders of magnitude between the mean free path of the gas and the system's characterising dimension, the pipe diameter. The ratio of these two quantities is known as the Knudsen number. This is the parameter most commonly used to classify the degree of rarefaction in a gas:

$$Kn = \frac{\lambda}{L}, \quad (1.1)$$

where λ is the mean free molecular path of the gas and L is some characteristic dimension of the system. Traditionally, flows where the Knudsen number rises above $Kn = 0.001$ are considered to be rarefied [2].

1.2.1 Continuum-equilibrium

Local thermodynamic equilibrium is defined as the state of minimum thermodynamic potential, in which a fluid may be considered to be continuous. This is true if the fluid is infinitely divisible in both space and time. A fluid may be described as being in equilibrium if there exist no spatial or temporal gradients within it.

The loss of local thermodynamic equilibrium in a gas implies that the microscale behaviour of the gas leads to gradients of macroscopic quantities in the

flow. Macroscopic variables (velocity, temperature, pressure *etc.*) describe molecular behaviour averaged over an element of gas. This element must be sufficiently large as to accurately describe the microscopic behaviour of the fluid without large statistical fluctuations, but sufficiently small as to allow the macroscopic variables to be represented by differential calculus. This is the continuum assumption, which implies that there is scale separation between the microscopic and macroscopic behaviour of a gas flow [2].

Complete equilibrium is a clearly defined state where no gradients of macroscopic quantities exist in a flow. Generally, when discussing equilibrium in a practical system, what is meant is that the flow is quasi-equilibrium in nature. The “equilibrium” assumption, in this context, is that the departures from local thermodynamic equilibrium in the system are small. Quasi-equilibrium flows can be successfully modelled using the traditional governing equations.

As rarefaction increases in a dilute gas, first the assumption of a quasi-equilibrium state becomes invalid, followed by the continuum assumption (the opposite is true of a dense gas.) If the continuum assumption is invalidated, the differential equations traditionally used in the analysis of fluid flow and heat transfer also become invalid.

Larger departures from the equilibrium state lead to discontinuities of momentum and energy at gas-solid interfaces, phenomena known as velocity slip and temperature jump, respectively. In addition, the nonlinear behaviour of the Knudsen layer can have a significant impact on the flow. The Knudsen layer is a near-wall region of fluid where intermolecular collisions do not fully exchange energy and momentum between the gas and the bounding surface. It typically extends one to two mean free paths from solid surfaces in gas flows at any scale, and cannot be modelled using traditional continuum methods. In a rarefied gas the increased relative size of the mean free path can mean that large proportions of the flow are within the Knudsen layer, and exhibit nonlinear behaviour. As such, near-wall and Knudsen layer physics can greatly influence fluid flow and heat

transfer, particularly in microsystems, where the surface area-to-volume ratio is often large.

1.3 Scope of this research

In summary, this research comprises

- The implementation of N-S-F continuum models modified to include rarefaction effects in OpenFOAM CFD,
- Simulation of key engineering case studies for which analytical, statistical or experimental data are available, and
- The development of a new approach to modifying the N-S-F equations for the analysis of microscale flows that is more general and flexible than previously available alternatives.

The primary contribution of this research is the production of a design-oriented analytical tool for fluid flow and heat transfer in gas microflows. The work makes use of specialised boundary conditions alongside modifications to the N-S-F equations that can replicate Knudsen layer behaviour. It provides engineers with the capability to rationally design gas microsystems using the same type of numerical studies that are common in macroscale fluid dynamics. With microscale engineering often at the forefront of developing technology, this is a valuable new capability for the field. The OpenFOAM model created is the first modified N-S-F model that is fully integrated into a mainstream CFD package, and that can successfully simulate compressible, non-isothermal flows.

In order to produce the final OpenFOAM model, the scope of this research includes extensive review of available technology for the numerical simulation of gas microflows, a study of the physics of rarefied flows, and a definition of the state of the art in modified continuum fluid dynamics models. Detailed studies of

the OpenFOAM source code and available modifying functions lead to the implementation of simple models for incompressible, isothermal microflows. Validation and verification exercises are carried out using simple flow configurations. The modified continuum models are then extended for application to compressible flows. Several engineering case studies are analysed in detail, and the efficacy of the model as a design tool assessed.

This research has also produced an alternative means of using continuum methodology to analyse rarefied gas flows. The new approach is based on the modification of the governing equations according to the geometric and rarefaction parameters of the local system, rather than with a single, specific function, as is the case in other models studied. Although this new method is empirical in nature, it offers the possibility of extending the N-S-F equations in a more general way than was previously possible, based on a parametric classification of the likely impact of rarefaction on the system. Knudsen layer shape and depth, for example, can be estimated based on the system geometry, Knudsen number and local gradients of macroscopic quantities.

The development of this new model was inspired by some of the challenges encountered when extending existing continuum models to non-isothermal, compressible flows. Work on this subject includes detailed analysis of the relative merits of available modifications for the governing equations, and in-depth investigation of the interaction between those models and the most commonly used boundary conditions for rarefied flows. The new method is devised as a means of circumventing many of the difficulties associated with the use of previous scaling models for simulating “real-world” flows. Preliminary testing of this method has been conducted, and the results are assessed alongside those of the more established models. A discussion of the potential future for the technique is presented.

1.3.1 Availability of data

The larger part of this research comprises the implementation of mathematical models for gas rarefaction behaviour in a numerical framework. Although numerical simulations and CFD can offer excellent performance and flexibility in the analysis of complex flows, the accuracy of the results is limited primarily by two factors: the correct application of the technology to the problem, and the limitations of the numerical approach employed. As rarefied-gas dynamics is a relatively specialist subject, responsibility for the former remains with the end user of the OpenFOAM models created in this research. The latter, however, requires the validation and verification of the code to be conducted in a responsible manner during the development of the simulations.

Unfortunately, the implications of operating experimental gas-flow apparatus at micrometre scales mean that reliable experimental data for the type of microflows in which we are interested are often difficult to find. The specialist laboratory equipment required to manufacture and conduct experiments on gas microdevices is prohibitively expensive for most academic institutions. As such, only data published in academic literature by experimental facilities are available for validation, which may not be in the area of interest. Much of the available literature focuses on experimental analysis of two phase flows, on liquid flows, or on comparatively large physical scales, as these are more practical to investigate experimentally than dilute gas flows. As such, other sources of data must be employed along with traditional experimental work to have full confidence in the results of the numerical studies. To ensure that accuracy is not unreasonably sacrificed in the pursuit of performance, the numerical models presented here are evaluated using several different types of available data, as outlined very briefly below.

Analytical solutions For incompressible, isothermal cases in simple channel geometries, analytical solutions to the N-S-F equations may be found, both in-

cluding and excluding the impact of the modifying functions used to represent gas rarefaction. These are exact solutions and, as such, are the preferred method of verifying that the numerical implementation operates correctly. Analytical solutions were employed in early development stages of the models.

Other numerical results In some instances, numerical simulations have been produced by other research groups that provide interesting comparison to the modified continuum models implemented here. Unless otherwise stated, these models are compared to those presented in this thesis, but are not used to validate or verify the results of simulations, as there may be a large degree of uncertainty involved in the external works.

Kinetic theory of gases The kinetic theory of gases is a term used to describe equations that determine the macroscopic properties of gas flows from knowledge of their behaviour at a molecular level. The Boltzmann equation describes, for example, the statistical position, velocity and state of any given molecule in a gas at any given time. The complex nature and number of real molecular interactions, however, make it impossible to solve the Boltzmann equation for any practical cases [3]. This has led to the development of many simplified kinetic models, but even these are computationally intractable for all but the simplest of flows. In cases where kinetic theory solutions are possible, however, the results are often very accurate, and are good sources of data for comparison, see e.g. [3–9].

Discrete molecular methods Increases in available computing power have facilitated the use of large-scale statistical simulations as a source of reliable solutions for fluid flow and heat transfer in rarefied gases. These simulations model the gas flow discretely, and produce results for macroscopic quantities through a process of ensemble averaging. Typically the application of statistical methods is limited by prohibitively expensive computational cost and susceptibility to scatter in the data that increases solution times greatly when discrete approaches are

used for low-speed flows. However, statistical results can be very accurate, and are well-established as an alternative source of data in cases for which experimental results are not available.

Experimental work Experimental results are obviously the preferred means of validation for numerical simulations, especially for more complex flows and system geometry. The most accurate known data is produced by good quality experimental work, and, where reliable sources are available, they are used extensively.

1.4 Outline of thesis

Chapter 2 Characterising parameters for microscale flows are introduced. Critical evaluation of the most commonly applied techniques for modelling rarefied flows is provided for approaches ranging from discrete molecular simulations through to classical macroscale fluid dynamics.

Chapter 3 The physical effects of rarefaction in gas flows are described in detail, including the impact of loss of local thermodynamic equilibrium, boundary discontinuities and the Knudsen layer. Conventionally applied boundary conditions such as Maxwell’s velocity slip and Smoluchowski’s temperature jump are introduced [10, 11].

Chapter 4 A review of the performance of available continuum models for microscale gas flows is carried out. Constitutive-relation scaling, a phenomenological method whereby the linear constitutive relations of the Navier-Stokes-Fourier equations are replaced by modified functions is outlined. The technique was proposed only relatively recently by Lockerby et al. [12], and the current state of the art is presented. The finite-volume numerics package OpenFOAM is introduced, and the modifications made to the package in order to successfully incorporate constitutive scaling are detailed [13].

Chapter 5 The new OpenFOAM model is applied to several incompressible, isothermal flows. Results are reported for a range of cases, presented alongside a discussion of the efficacy of the approach in each case. Shear-driven Couette flow and pressure-driven Poiseuille flow results are compared to analytical solutions. Flows through microchannels with plate and venturi type constrictions are verified using available experimental data [14]. Cylindrical Couette flow in the special low accommodation coefficient case is studied, with results compared to available direct simulation Monte-Carlo (DSMC) results and other numerical solutions [15, 16].

Chapter 6 An OpenFOAM solver for compressible gas microflows is introduced. Two published constitutive relation models implemented within it are applied to non-isothermal and fully compressible case studies [12, 17]. Initially, half-space problems are used to contrast the different available constitutive scaling models, before a compressible Couette flow case is examined, with results compared to available kinetic theory and DSMC data [4, 6, 18]. A detailed critical evaluation of the method is carried out, focusing in particular on the relationship between momentum and energy transfer and on the selection of appropriate boundary conditions for complex, non-isothermal flows.

Chapter 7 A new methodology for defining constitutive scaling functions to model Knudsen layer behaviour is described, in which constitutive scaling is expressed in terms of local parameters of the system. The approach is demonstrated using a simple test case. First, the model determines the depth and shape of the Knudsen layer based on the geometry and rarefaction of the system, then reverse-engineers an appropriate effective viscosity function for use in the constitutive scaling process. The proposed methodology, and its potential for future development, are discussed in detail.

Chapter 8 Conclusions are drawn about the effectiveness of the different scaling models applied, including the newly proposed “local-parameters” model, and about the potential of the constitutive scaling method as an engineering design tool. Related work ongoing in the MultiScale Flows Research Group is briefly discussed, and suggestions are made for further research.

Chapter 2

Modelling rarefied gases

2.1 Characterising gas rarefaction

The Knudsen number has been introduced in Chapter 1 as the characterising parameter of gas rarefaction, and defined as the ratio of the molecular mean free path of the gas to a characteristic system dimension, $Kn = \lambda/L$. The mean free path of the gas is the average distance that a molecule will travel before a collision with another molecule. It is typically defined for a gas in equilibrium, and depends on the velocity distribution of the molecules in the gas. For the equilibrium state, molecular velocities conform to the Maxwellian statistical distribution function, commonly referred to as the equilibrium distribution [19]. An example of a typical Maxwellian distribution (in one spatial dimension) is shown in Fig. 2.1. The premise of the equilibrium distribution is that the most probable velocity of a molecule will be the average velocity, and that it is statistically unlikely that a large number of molecules will have either a much greater or much lower velocity than the average value. The shape of a gas' equilibrium distribution will be influenced by its molecular mass, its temperature, and its velocity in three-dimensional space. In turn, the expression that describes the mean free path of gas in a system will be determined by both its equilibrium distribution function and the choice of force-interaction model used to represent the gas molecules.

The simplest molecular interaction law is the hard-sphere model, which treats

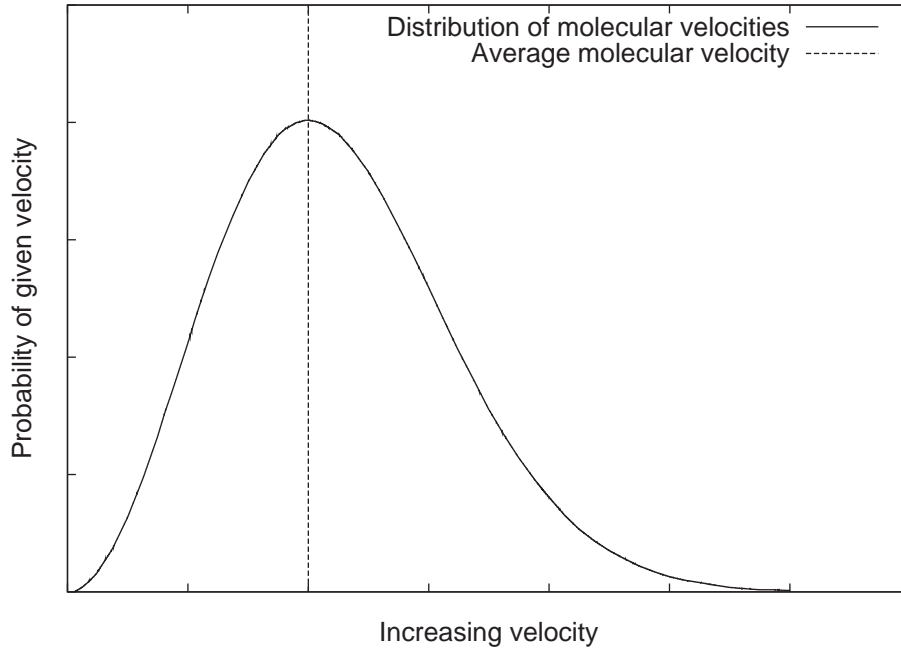


Figure 2.1: Example of a Maxwellian distribution of molecular velocities in a 1D case. The most probable molecular velocity is the average value, with probability decreasing towards the maximum and minimum velocities.

each molecule as an elastic sphere whose diameter is finite, but small in comparison to the mean molecular separation. Beyond the sphere diameter, there is no interaction potential between molecules, but when the spheres collide the repulsion is taken to be infinite [7]. The hard-sphere model is used throughout this thesis, as it can offer a reasonable approximation to the behaviour of monoatomic gases. For the hard-sphere model in a single-species gas, the mean free path is defined as

$$\lambda = \frac{1}{\sqrt{2}\pi\eta\phi^2}, \quad (2.1)$$

where η is the molecular density per unit volume (the number density), and ϕ is the diameter of the elastic spheres [8]. A more common expression of this form, given in terms of macroscopic quantities, is

$$\lambda = \nu \sqrt{\frac{\pi}{2RT}}, \quad (2.2)$$

where ν is the kinematic viscosity of the gas, R the specific gas constant and T the temperature [3]. Eq. (2.2) is the expression used to calculate mean free path throughout this thesis.

The Knudsen number is also dependent on L , a characteristic system dimension. This will depend on the system geometry, but in simple configurations it is most common to use the smallest dimension of the system, normally channel height or pipe diameter. In other cases the choice is less obvious, for example, in flow over an unconfined microsphere the sphere radius is used to define the Knudsen number [20]. In each case study examined in this thesis, the characteristic dimension used to define Knudsen number will be stated.

As outlined in Chapter 1, the Knudsen number characterises the degree of rarefaction of gas flows. The behaviour of rarefied gases is classified into four main categories, as shown in Fig. 2.2, which are described below [21].

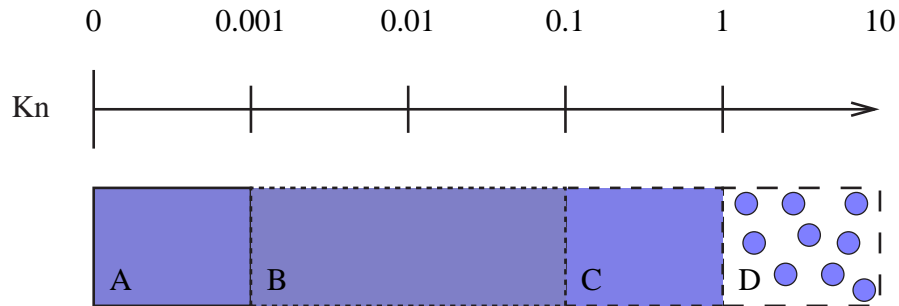


Figure 2.2: Gas flow regimes classified by Knudsen number; A represents fully continuous flow, B slip/jump flow, C transitional behaviour and D free molecular flow.

In the limit of $Kn \rightarrow 0$, regime A, the gas behaves as an entirely continuous fluid at, or very near to, the equilibrium state. In this flow regime, which extends to $Kn \approx 0.001$, the N-S-F equations remain valid [2]. The Knudsen layer, a region of non-equilibrium flow found within one to two mean free paths of a surface, has no appreciable impact on the flow. The gas is equilibrated with its bounding

surfaces, and the no-slip and no-jump boundary conditions of macroscale fluid dynamics hold.

As Kn increases into regime B, in the range $0.001 < Kn < 0.1$, the flow moves further from local thermodynamic equilibrium. In this flow regime the Knudsen layer is traditionally considered to have a negligible impact on the flow, although research conducted in the production of this thesis has demonstrated that this is unlikely to be true in some microsystem cases, particularly in the upper range of the regime [22]. The main evidence of rarefaction in the gas presents at the system boundaries, where discontinuities of energy and momentum occur. These discontinuities must be modelled using slip or jump boundary conditions, hence, this regime is often referred to in the literature as the slip flow regime.

In the range of $0.1 < Kn < 1$ gas flows are said to be transitional, whereby increasingly fewer intermolecular collisions take place in a given time period as Kn becomes larger. In regime C, the nonlinear structure of the Knudsen layer can represent a large proportion of the flow. In microflows, which are most commonly internal flows, the extent of the Knudsen layer increases until at approximately $Kn = 1$, the Knudsen layers extending from bounding surfaces would represent the entire flow field. Accordingly, it is imperative that any numerical model intended for use in the transition regime has the ability to model the Knudsen layer structure reliably. The magnitude of boundary discontinuities also increases as flows become transitional, and it can be shown that in the upper transition regime, particular care must be taken when applying the conventional mathematical expressions for these discontinuities [22].

As Knudsen number increases beyond $Kn = 1$ into regime D, the gas flow is almost free molecular in nature, and becomes completely so beyond $Kn \approx 10$ [2]. In free molecular flows, the gas molecules act individually and collisions between them are negligible. In this regime simple solutions to many flow configurations exist, as only collisions between gas molecules and bounding surfaces need be considered.

In this thesis the flows analysed are typically in regions B and C, where gas rarefaction has a significant impact on the behaviour of the flow, but where it still behaves recognisably as a fluid. In these regimes, the increased importance of individual molecular interactions at system boundaries and the structure of the non-equilibrium Knudsen layer are the dominant effects of rarefaction. They are the most important flow features to capture in numerical analyses [21].

2.2 Approaches to modelling rarefied flows

The loss of local thermodynamic equilibrium and the breach of the continuum assumption in rarefied gas flows lead to the breakdown of the classical governing equations of fluid dynamics. As Kn increases beyond 0.001 the N-S-F equations are no longer able to accurately predict the behaviour of gas flows. In order to simulate the macroscopic behaviour of rarefied gases properly it is necessary to consider the influence of their molecular nature. A large number of approaches to the numerical simulation of rarefied gases exist, ranging from discrete models of molecular motion, averaged for macroscopic quantities, through to extensions of the traditional hydrodynamic equations. The following brief review considers the most commonly applied techniques, assessing their suitability for integration into mainstream engineering design tools.

2.2.1 Kinetic theory of gases

The Boltzmann equation is the governing equation of the kinetic theory of gases, and uses classical mechanics to describe the velocity, position, and state of a gas molecule in a flow at any given time. It is based on several simplifications of the molecular behaviour of gases; it is assumed that the molecular diameters remain small in comparison to the molecular separation, that the molecules are in constant random motion, and that they undergo frequent collisions. It is also assumed that molecular chaos prevails, and that bulk motion may be superimposed on the random molecular motion. Further simplifications, assuming that

the gas flow is dilute and composed of a single, monoatomic species, lead to the Boltzmann equation:

$$\frac{\partial f}{\partial t} + \mathbf{v} \cdot \frac{\partial f}{\partial \mathbf{r}} + \mathbf{F} \cdot \frac{\partial f}{\partial \mathbf{v}} = C(f), \quad (2.3)$$

where $f(\mathbf{r}, \mathbf{v}, t)$ describes the number of gas molecules in a volume of gas that possess velocity \mathbf{v} at the time t . The spatial position of a molecule is given by \mathbf{r} , and the flow is acted upon by a body force, \mathbf{F} . The first term on the left hand side of the equation describes the transient changes of the molecular distribution, f , while the second term on the left hand side is the convective change in the distribution. The Boltzmann equation describes how the bulk motion of the gas, on the left hand side, relates to the molecular collisions taking place in the gas, given by the collision integral $C(f)$ on the right hand side. The collision integral is highly complex, involving velocity-space coordinates as independent variables, with the result that it is computationally intractable to solve the equation for most flows [23].

In order to apply the Boltzmann equation practically, the collision integral can be replaced by a simplified kinetic model of the collision processes in the flow. The kinetic models linearize the Boltzmann equation, replacing the complex function $C(f)$ with expressions that can be solved to determine the distribution function f of macroscopic quantities. One of the most widely used kinetic models is the Bhatnagar-Gross-Krook (BGK) model [24]. In this model, the collision integral is replaced with the product of the collision frequency between molecules and the difference between a Maxwellian distribution function and the actual distribution function sought [25]. For analysis of near-wall regions, the collision integral may be replaced with specialised synthetic scattering kernels, such as the Cercignani-Lampis model, which include the effects of interactions between the gas and the wall [5].

Linearizing the Boltzmann equation using kinetic models, it is possible to produce very accurate solutions for some fundamental cases. Unfortunately, sim-

plified kinetic models are rarely appropriate for complex geometry, and the assumptions implicit in the linearisation process greatly limit applicability of the results for practical rarefied flows [26].

2.2.2 Discrete molecular models — DSMC

The direct simulation Monte-Carlo (DSMC) method was originally proposed by Bird, and is a particle-based approach to simulating the Boltzmann equation, rather than solving it directly [27]. DSMC does not operate on individual molecules, but on a large number of computational particles, each of which is assumed to be representative of a much larger number of individual molecules. At each time step the particles are moved around the system, and can undergo binary collisions that will alter their velocity and internal energy, but not their physical position. In consequent time steps, particles have their physical positions adjusted around the system in a deterministic manner, i.e. according to their previous collision and the laws of classical mechanics. The simulation continues until ensemble averages of the individual observed states give a statistical simulation of the physical behaviour of the gas flow to sufficient accuracy. Macroscopic properties of the gas are inferred from the averages of the particle behaviour.

Although it can be shown that DSMC provides results that are directly equivalent to solving the Boltzmann equation, its computational intensity restricts its applicability for use as an engineering design tool [23, 28]. There are two key factors that make DSMC a particularly computationally expensive process. Firstly, DSMC particles are tracked within a computational mesh, which is used to identify upcoming collisions at each time step and to produce the information used in the statistical averaging processes. In order to ensure that only physical results (i.e. system states) are produced, both the time step and the mesh-cell size must remain smaller than the mean collision time and mean free path, respectively [27]. Thus, the memory requirements of DSMC processes can be extremely demanding, given the large number of time steps required for accurate ensemble-averaging of

non-equilibrium systems.

The second factor that limits the use of DSMC as a design tool, particularly for gas-based microsystems, is susceptibility to statistical noise. In the low-speed cases commonly found in microscale flows, a much larger number of sample system states is required to produce accurate averages of the macroscopic quantities. The computational time necessary to obtain low-scatter results for low speed rarefied gas flows then becomes prohibitive even on massively parallel computing facilities [23]. In recent work, Baker and Hadjiconstantinou have proposed a means of significantly reducing the computational effort involved in DSMC for microsystems by considering the relatively small departures from equilibrium observed in some low-speed flows [29]. Although this modified method may yet become the *de facto* standard for low-speed DSMC, it does not currently offer sufficient improvements in computational requirements for complex cases to provide the particle-based approach with an advantage over continuum models for microsystem design applications. It is also limited, in studying small departures from equilibrium, to relatively low- Kn applications.

Currently, DSMC is predominantly used in academic research for the study of aerodynamics and hypersonics, but it is now also accepted as an analytical tool for other non-equilibrium flows. The method produces reliable data in many cases where equivalent experimental results are not available, and can also be applied to complex flows in realistic configurations, given sufficient time and computing resources are available [30, 31]. These features of DSMC are particularly attractive for analysis of gas microflows, where complex geometry is common, and where practical constraints often preclude detailed experimental work. In practice, however, the computational effort involved in most DSMC makes it prohibitively expensive, in terms of both time and required computational facilities, for consideration as an industrially applicable design tool.

2.2.3 The Chapman-Enskog expansion

As an alternative to directly solving the Boltzmann equation, it is possible to determine some non-equilibrium distribution functions, represented by f , as a perturbation of the local Maxwellian distribution, f_M , using a series expansion. The traditional Chapman-Enskog (C-E) series is written in terms of Kn :

$$f = f_M (1 + a_1(Kn) + a_2(Kn)^2 + \dots), \quad (2.4)$$

where the coefficients a_n are functions of density, velocity and temperature. The C-E expansion produces a series of continuum equations that are assumed to converge to the Boltzmann equation with increasing order [9]. Practically, this assumption of convergence implies a limit to the degree of departure from the equilibrium state that may be successfully predicted using the C-E expansion.

To zeroth-order in Kn , the C-E series produces the Euler equations, which are inviscid constitutive relations, and valid for gas flows far from bounding surfaces when Kn is below approximately 10^{-2} . To first-order in Kn , the series results in the viscous N-S-F equations. The higher the order of the terms in the series, in theory, the greater the departure from the equilibrium distribution that may be modelled. At the second-order in Kn , the Burnett equations are produced, which are similar to the N-S-F equations, but which include more complex constitutive expressions for stress and heat flux [32].

Since Burnett's original work, many others have derived alternate second-order equations, using either different physical interpretations of the C-E series, or working with the assumption that it should converge to kinetic approximations to the Boltzmann equation, see e.g. [33–35]. Although all of the published models agree on the form of the first-order N-S-F equations, there is no general agreement as to the correct form of the second-order equations and, as yet, no single model is demonstrably superior [36, 37].

The most attractive feature of the higher-order equation sets that arise from the C-E expansion is that they can, in theory, predict the behaviour of gas flows

further from equilibrium than the N-S-F equations, but reduce to the lower-order equations in regions of flow where Kn is low. In many flows this would greatly reduce the computational cost of non-equilibrium numerical simulations, which would otherwise require stochastic treatments such as DSMC. Also, as the Burnett equations are continuum-based, it would theoretically be possible to integrate them into CFD simply by altering the constitutive relationships that link the energy and momentum equations. Unfortunately, the higher-order equation sets also have drawbacks that limit their applicability for use in engineering design.

Whilst it is true that the Burnett-order equations can capture more of the non-equilibrium physics of microsystems than the N-S-F equations, such as wall-normal shear stress and heat flux, they are not generally well-posed. For example, many of the second-order equations are numerically unstable, and can require complex solution methods to be employed in order to ensure that they produce unique solutions. Also, the higher order terms require higher-order boundary conditions, which are not necessarily known *a priori*. This is particularly problematic at solid boundaries, where the physical interactions between gas molecules and wall molecules are not well understood. In addition, not all forms of the Burnett-order equations are able to model the non-equilibrium Knudsen layer observed in very near-wall regions, which is an important physical feature of many microflows [37].

2.2.4 Moment models

As an alternative to the C-E expansion, Grad proposed that the non-equilibrium distribution function could be approximated using a series of first-order partial differential moment equations, obtained using the Hilbert expansion [9]. Hermite tensor polynomials are used to close the equations, taken around the Maxwellian state, with coefficients related to the moments [38]. Grad's expansion using five moments (density ρ , three components of velocity u_i and temperature T) is equivalent to the Euler equations from the C-E expansion. Thirteen moments (density

ρ , momentum density ρu_i , energy density $\rho\epsilon$, stress $p_{(ij)}$ and heat flux q_i) equate to the Burnett-order, then twenty-six moments for Super-Burnett order, and so on [39]. Grad's moment equations retain many of the drawbacks of the higher-order C-E terms, in that they are numerically unstable, and require complex, and unknown, boundary conditions. Although some recent work such as [40] has attempted to resolve the problem of boundary conditions for Grad's equations, they also require a large number of variables to describe certain flows, and can be shown to produce non-physical results in some cases.

Recently, Struchtrup combined Grad's 13-moment expressions with the C-E expansion to produce the regularized 13-moment equations, the *R13*, with the aim of avoiding some of the problems of the traditional methods [41]. Further work is ongoing to determine appropriate boundary conditions in order to apply the *R13* equations to gas microflows [42–44].

2.2.5 Extending the Navier-Stokes-Fourier equations

The N-S-F equation set in 3D comprises five conservation equations; one equation for mass, three for momentum and one for energy. The equations are linked by linear constitutive relationships for shear stress and heat flux. Using a Cartesian coordinate system where spatial coordinates x, y, z have velocity components u, v, w , respectively, and \mathbf{u} is a velocity vector, the N-S-F equations are given in unsteady 3D form as follows:

$$\frac{\partial \rho}{\partial t} + \nabla \cdot (\rho \mathbf{u}) = 0, \quad (2.5)$$

$$\frac{\partial (\rho \mathbf{u})}{\partial t} + \nabla \cdot \mathbf{u} (\rho \mathbf{u}) = -\nabla p + \nabla \cdot \tau + S_M, \quad (2.6)$$

where τ is the stress tensor and S_M represents momentum sources. The energy equation is

$$\frac{\partial (\rho h_0)}{\partial t} + \nabla \cdot (\rho h_0 \mathbf{u}) = \nabla \cdot (\kappa \nabla T) + \frac{\partial p}{\partial t} + \Phi + S_h, \quad (2.7)$$

where h_0 is enthalpy, S_h represents source/sink terms, κ is the thermal conductivity and Φ is the dissipation function given by

$$\begin{aligned} \Phi = 2\mu & \left[\left(\frac{du}{dx} \right)^2 + \left(\frac{dv}{dy} \right)^2 + \left(\frac{dw}{dz} \right)^2 \right] + \mu \left(\frac{du}{dy} + \frac{dv}{dx} \right)^2 \\ & + \mu \left(\frac{du}{dz} + \frac{dw}{dx} \right)^2 + \mu \left(\frac{dv}{dz} + \frac{dw}{dy} \right)^2 - \frac{2}{3}\mu (\nabla \mathbf{u})^2. \end{aligned} \quad (2.8)$$

These equations are widely used at the macroscale for computation of a range of fluid flow and heat transfer problems. At the microscale, where Kn increases and the molecular nature of gas flows becomes important, the N-S-F equations alone do not predict the effects of gas rarefaction [2].

In the slip- and transitional- Kn regimes, the most apparent effects of gas rarefaction are velocity slip/temperature jump and the Knudsen layer. Using slip and jump boundary conditions, it is possible to extend the applicability of the N-S-F equations into the slip flow regime: $0.001 < Kn < 0.1$ [10, 11]. This is the most commonly applied numerical technique for weakly rarefied flows.

Recently, new approaches designed to extend the applicability of the N-S-F into the transition regime have also been developed, see e.g. [12, 17, 45]. By modifying the constitutive relationships used to derive the N-S-F equations, for example, they can be made to incorporate the effects of the Knudsen layer [12]. This process, known as constitutive-relation scaling, uses available data describing the shape of the Knudsen layer to modify the linear shear stress/strain rate and heat flux/temperature gradient relationships that define the N-S-F equations. The primary advantage of the constitutive scaling approach is that it is an efficient method of simulating rarefaction effects within a continuum framework, which is much less computationally expensive than direct simulation techniques.

Generally, these modifications do not provide the N-S-F equations with the means to actually model the physics of rarefied flows, however, they can allow them to simulate the observed behaviour at higher Kn more accurately. This

type of approach is common in other areas of fluid dynamics, where empirical models are often used. For example, many different empirical models have been developed to simulate turbulence in high Reynolds number flows [46].

Given the difficulties inherent in physically modelling non-equilibrium gas flows, the primary advantage of an extended N-S-F model would be that it would remain relatively computationally un-intensive compared to alternatives such as kinetic theory and DSMC. Also, modifying the N-S-F equations, which are already in widespread use, is likely to make for a more practical analysis tool than emerging alternatives such as the *R13* equations [41]. If we consider solving the Boltzmann equation directly as a bottom-up approach to the problem, in that it directly incorporates all aspects of the physical behaviour of the gas, then using extended N-S-F equations constitutes a top-down approach. In such a strategy, the key features of rarefied flows observed in experimental work or kinetic solutions to the Boltzmann equation are selectively “retro-fit” to a much simpler continuum model [12]. Although this necessarily implies some loss of generality, from an engineering perspective it has the potential to generate a very effective design tool for some non-equilibrium flows. This thesis exploits the potential of extending the N-S-F equations, by integrating available models into a mainstream CFD framework, producing an efficient and flexible means of analysing non-equilibrium flows.

2.2.6 Summary

In summary, it is clear that modelling non-equilibrium flows is both particularly challenging and traditionally computationally intensive. In order to effectively design microsystems in the short-to-medium term, one promising approach is to identify the key features of gas rarefaction, and incorporate them into simpler numerical models. In order to do so, it is necessary to understand the physics that characterise the effects of rarefaction in the transition regime, primarily interface discontinuities and the Knudsen layer, and to discuss how such flow features are

traditionally accommodated in analytical and numerical models.

Chapter 3

Physics of rarefied flows

3.1 Interfacial phenomena

Consider a gas flowing uniformly in a direction y with bulk velocity u , parallel to an imaginary plane S which has a finite area. There exists a velocity gradient across the plane, du/dx , as shown in Fig. 3.1. The gas flowing on the left hand side

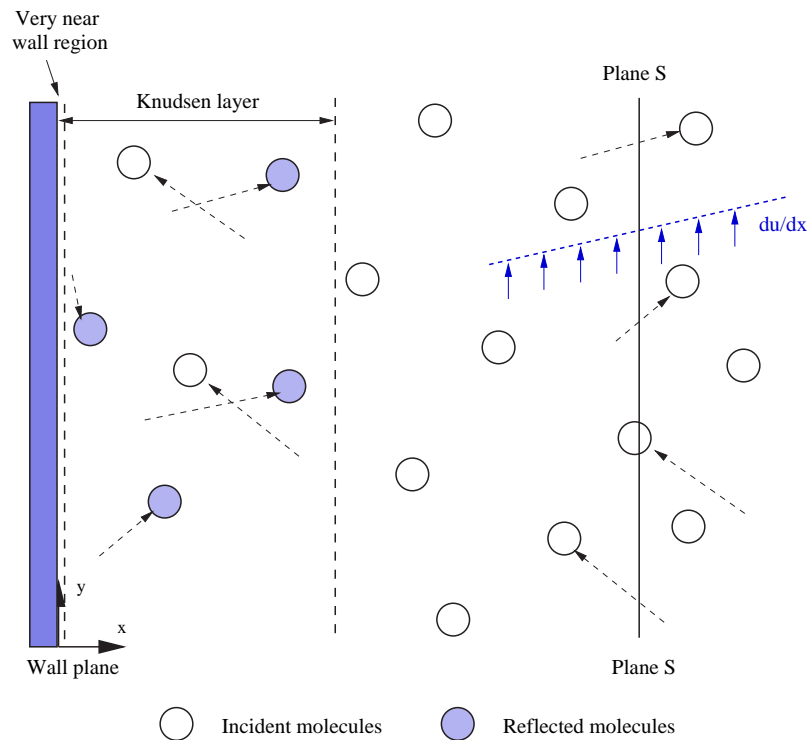


Figure 3.1: Molecular interaction across a plane S , which gives rise to shear stress in the gas; and similar molecular interaction in the near-wall Knudsen layer region, where both incident and reflected “streams” of molecules interact.

of the plane S (within a suitably small distance) is moving at a given velocity, and the gas on the right hand side of the plane is moving at another given velocity which is higher. As a molecule crosses from the right to the left hand side of the plane (negative x -direction), it will lose tangential momentum in collisions until it adopts the same velocity as the gas on the left hand side of the plane. The inverse will be true of a molecule crossing from left to right — it will gain tangential momentum from collisions until it assumes the velocity of the stream on the right hand side. Thus, there exists a force on the surface area of the plane which acts in both positive and negative y -directions, brought on by the tangential components of momentum that any crossing molecules have or have lost. This force acting over the surface area is the shear stress, τ , in the fluid. For suitably small tangential components of momentum the coefficient of viscosity, μ , linearly relates shear stress to the velocity gradient, du/dx :

$$\tau = \mu \frac{du}{dx}. \quad (3.1)$$

If we now consider the stationary wall in Fig. 3.1, rather than the plane S , there will be a stream of gas molecules incident to the wall, and a post-collision stream receding from it. The viscous force on the wall surface is due to the difference in tangential momentum between the incident and receding streams, rather than between molecules crossing an imaginary plane. From a macroscale perspective (a quasi-equilibrium system) the action of this viscous force is what reduces the tangential velocity of the gas to zero at the surface — leading to the no-slip boundary condition.

From a microscale perspective, momentum and energy are being exchanged between gas molecules and wall molecules in collisions both at and very close to the gas-surface interface. A non-rarefied gas, by definition, has a molecular mean free path that is negligible compared to the system dimensions. Molecules very near the surface will undergo a large number of collisions both with the wall and with other gas molecules in a very short timescale, reaching an almost

instantaneous equilibrium state. In non-rarefied gases, it is not possible to observe any discontinuity between the velocity of the gas at the wall and the velocity of the wall, but thin non-equilibrium regions where these average velocities are not the same do physically exist. In fact, the macroscopic approach produces the “correct” approximation of the flow losing tangential momentum at the wall only because the length scale of the near-wall non-equilibrium region (the Knudsen layer) is negligibly small.

When gas flows become rarefied, the length-scale of the Knudsen layer becomes large in comparison to the system dimensions, and the discontinuity of momentum at the surface interface becomes significant¹. That is to say, the velocity of gas flow *at* the wall can no longer safely be assumed to be the velocity *of* the wall. This was originally observed in experimental work carried out in the 19th century, investigating the effects of gas-damping on a vibrating disc [47]. The viscous damping was found to be reduced at low pressures as the gas “slipped” over the solid surface of the disc. This slip is in fact the non-equilibrium discontinuity between the gas velocity and the surface velocity that becomes larger as the gas becomes rarefied. Specifically, when the mean free path becomes suitably long, the gas flow at the wall cannot be considered to lose all of its (relative) tangential momentum to the wall.

3.1.1 Maxwell’s phenomenological model

In order to represent velocity slip at system boundaries, in 1879 Maxwell produced a phenomenological model, based on his earlier work on the theory of viscosity in gases [10, 19]. Phenomenological models are mathematical descriptions derived from the observed behaviour of physical systems, rather than from theoretical knowledge, and which may be used successfully to predict the behaviour of other, similar systems. Maxwell’s phenomenological slip model has a lengthy derivation,

¹A similar discontinuity of energy also exists at surface interfaces, which is referred to as temperature jump, but for now let us consider the velocity discontinuity as representative of the boundary phenomena in rarefied flows.

but can be described more simply as an analogue to the macroscopic model [8, 10]. It is designed to work as a boundary condition with the continuum equations of fluid dynamics. Consider once more a gas flowing parallel to the planar wall shown in Fig. 3.1. In the macroscopic approach, shear stress arises at the surface due to the exchange of tangential momentum between gas molecules approaching the wall and gas molecules receding from it. The approaching gas and the receding gas are assumed to have equal influence on the total shear stress at the surface:

$$\left[\frac{1}{2} \mu \frac{du}{dx} \right]_{\text{Approaching}} + \left[\frac{1}{2} \mu \frac{du}{dx} \right]_{\text{Receding}} = \left[\mu \frac{du}{dx} \right]_{\text{Total}} \quad (3.2)$$

In Maxwell’s model, each macroscopic term in Eq. (3.2) can be replaced by a microscopic “equivalent”. The equivalent terms are approximations of molecular behaviour that Maxwell produced based on his observations of rarefied gas flows. The fluid approaching the wall from the bulk flow is assumed to be composed of molecules with an equilibrium velocity distribution. The contribution of this flow to the shear stress at the wall remains the same as in the macroscopic description: $\frac{1}{2} \mu \frac{du}{dx}$. The stream of molecules receding from the wall is assumed at the microscopic level to be equivalent to a simple effusive flow. A typical effusive velocity distribution would be that of a flow of individual molecules through a small hole (with diameter of the order of the mean free path) in a planar surface. The total number of molecules that would issue effusively from such a system per second, Γ_n , may be described simply in terms of the mean molecular speed, \bar{v} , and the number density of molecules in the flow, η : $\Gamma_n = \frac{1}{4} \eta \bar{v}$ [8]. This number of molecules leaving the surface is then multiplied by the velocity of the gas at the wall, the unknown slip velocity, u_{slip} , to produce the receding stream’s contribution to the shear stress at the wall. However, the observation of a slip velocity in itself implies that some tangential momentum is retained by the gas at the wall. To determine the slip velocity whilst conserving momentum, Maxwell represented the fraction of tangential momentum that the molecules on average lose to the wall as the proportion σ of their original tangential momentum. This is effectively

a “relaxation” of the macroscopic assumptions, and represents the mathematical difference between the macroscopic description and the microscopic description, where, for non-equilibrium flows

$$\left[\frac{1}{2} \mu \frac{du}{dx} \right]_{\text{Receding}} \neq \frac{1}{4} \eta \bar{v} u_{\text{slip}}.$$

Effectively, Maxwell’s argument is that if the macroscale shear-stress analogy were to imagined to hold true, then it would be possible to account for deficiencies in that assumption numerically by specifying the fraction of tangential momentum lost to the wall. Introducing this relaxation factor, or tangential momentum accommodation coefficient, as it is more commonly known, a microscopic description of the shear stress at the wall is obtained,

$$\sigma \left(\frac{1}{2} \mu \frac{du}{dx} + \frac{1}{4} \eta \bar{v} u_{\text{slip}} \right) = \mu \frac{du}{dx}. \quad (3.3)$$

Incorporating $\rho = \eta m$, which relates number density and the mass of the gas molecules, m , to the macroscopic density, ρ , Eq. (3.3) can be rearranged to give the velocity slip:

$$u_{\text{slip}} = 2 \left(\frac{2 - \sigma}{\sigma} \right) \frac{\mu}{\rho \bar{v}} \frac{du}{dx}. \quad (3.4)$$

Substituting in the expression for mean molecular velocity in a Maxwellian distribution, $\bar{v} = 2\sqrt{(2RT/\pi)}$, the definition of mean free path given in Eq. (2.2), and the linear constitutive relationship between shear stress and strain-rate given in Eq. (3.1), we can obtain the most common form of Maxwell’s equation for velocity slip in rarefied flows over planar surfaces [8]:

$$u_{\text{slip}} = \left(\frac{2 - \sigma}{\sigma} \right) \lambda \frac{\tau}{\mu}. \quad (3.5)$$

Thus, we can determine the slip velocity of a rarefied hard-sphere gas at an interface using the mean free path of the gas, λ , the shear stress at the wall, τ , the dynamic viscosity, μ , which is a temperature dependent property of the

gas, and the degree of tangential momentum accommodation, σ , which may be thought of as a property of a particular gas-surface interaction. The tangential momentum accommodation coefficient determines the proportion of molecules reflected from the wall specularly (equal to $\sigma - 1$) or diffusely (simply σ), where $0 < \sigma \leq 1$. Specular reflection implies that the molecular tangential momentum of the impinging molecules is perfectly reflected, and that the gas therefore exerts no tangential stress on the wall. It is also assumed that no energy exchange takes place between the wall and the gas molecule. In the case of diffuse reflection, molecules are ascribed random velocities with the average loss of all of their tangential momentum, and recede at the temperature of the wall.

Eq. (3.5) is the most widely used form of Maxwell's equation, see e.g. [20]. In following the macroscale approach to derive the equation, however, many of the subtleties of the original work are easily lost [10]. Eq. (3.5) assumes, for example, that there is no stream-wise variation in wall-normal velocity (i.e. that the bounding surfaces of the flow are non-rotating and planar). Also, this formulation neglects the influence of thermal creep, a process whereby a temperature gradient tangential to the surface generates additional slip flow along the surface in the direction of increasing temperature [48].

The microscopic explanation of thermal creep is relatively simple. If tangential momentum is not fully accommodated between the gas and the wall due to rarefaction, then some proportion of the molecules will be reflected from the wall diffusely (with Maxwell's proposed effusive velocity distribution). In regions of higher temperature, the gas molecules have a higher average velocity. If the molecules were specularly reflected, then their original tangential momentum would simply be reversed, and the flow would move from hot to cold as expected. In the hot flow, the higher average velocity implies that the diffusely reflected gas molecules will rebound more strongly from the wall in randomly ascribed directions than in the cold flow. Thus, the gas will gain tangential momentum towards the regions of increased temperature, producing a net flow from cold to

hot [8].

Maxwell's original expression for velocity slip over planar surfaces included a second term, incorporating the thermal creep effect. Considering a planar surface where n is the co-ordinate normal to the wall and x is the co-ordinate tangential to it, the conventional expression of the full Maxwell slip equation is

$$u_{\text{slip}} = \left(\frac{2 - \sigma}{\sigma} \right) \lambda \frac{du_x}{dn} + \frac{3}{4} \frac{\mu}{\rho T} \frac{dT}{dx}, \quad (3.6)$$

where u_x is the x -component of the slip velocity, T is the gas temperature, and dT/dx is the temperature gradient tangential to the surface interface [10]. Whilst this form of Maxwell's equation is commonly implemented in analytical and numerical simulations of the N-S-F equations, it is important to note that it is not applicable to surfaces with curvature. For example, for a two dimensional surface curvature, Lockerby *et al.* showed the correct form of Eq. (3.6) to be

$$u_{\text{slip}} = \left(\frac{2 - \sigma}{\sigma} \right) \lambda \left(\frac{du_x}{dn} + \frac{du_n}{dx} \right) + \frac{3}{4} \frac{\mu}{\rho T} \frac{dT}{dx}, \quad (3.7)$$

where u_n is the gas velocity normal to the wall [16]. The additional term featuring in Eq. (3.6) but not in Eq. (3.5) can have a significant influence on the velocity slip in flows over surfaces with curvature. For example, it can be demonstrated that accurate predictions of velocity profile inversions in cylindrical micro-Couette flow are only achieved when Eq. (3.6) is used [16, 36]. In order to fully generalise Maxwell's equation for use in three-dimensional geometries, it should be written in vector form as follows;

$$\mathbf{u}_{\text{slip}} - \mathbf{u}_{\text{wall}} = A_1 \left(\frac{2 - \sigma_U}{\sigma_U} \right) \frac{\lambda}{\mu} \boldsymbol{\tau} + \frac{3}{4} \frac{\text{Pr}(\gamma - 1)}{\gamma p} \mathbf{q}, \quad (3.8)$$

where the tangential shear stress is $\boldsymbol{\tau} = (\mathbf{i}_n \cdot \boldsymbol{\Pi}) \cdot (\mathbf{1} - \mathbf{i}_n \mathbf{i}_n)$ and heat flux is $\mathbf{q} = \mathbf{Q} \cdot (\mathbf{1} - \mathbf{i}_n \mathbf{i}_n)$, with bold type-face denoting a vector quantity. The Prandtl number Pr relates energy and momentum diffusivity, γ is the specific heat ratio, and p is the gas pressure at the wall. A unit vector normal to, and away from, the wall is \mathbf{i}_n , with $\boldsymbol{\Pi}$ the stress tensor at the wall, $\mathbf{1}$ the identity tensor, and \mathbf{Q} the heat

flux vector at the wall. The slip coefficient A_1 , is equal to 1 in Maxwell's original derivation. The accommodation coefficient symbol σ has also been replaced with σ_U , in order to distinguish between the tangential momentum accommodation coefficient, which affects velocity, and the equivalent thermal value that will be discussed in section 3.1.3.

Although it is phenomenological in nature, Maxwell's slip model can be seen to be very effective across a wide range of cases, and is the most commonly-applied velocity boundary condition for rarefied gas flows [20]. Unfortunately, Maxwell's model does not capture the underlying physics of the microsystem flows that it is used to represent. Consequently, as Knudsen number approaches the transition regime, the accuracy of Maxwell's model can be seen to be greatly reduced — even when used in conjunction with appropriate models for Knudsen layer effects [22].

3.1.2 Phenomenological model vs. physical behaviour

Maxwell's model assumes that in a rarefied gas flow parallel to a wall, molecules approaching the wall will do so with an equilibrium velocity distribution, such as would be found elsewhere in the bulk flow. On colliding with the wall, gas molecules are said to be reflected either specularly or diffusely, with the proportion of each determined by the tangential momentum accommodation coefficient. Both specularly and diffusively reflected molecules are initially incident to the wall with the same equilibrium velocity distribution. However, following collisions at the interface, the diffusely reflected molecules will have exerted a tangential stress on the wall, and the specularly reflected molecules will not. Thus, the post wall-collision velocity distributions of the specularly and diffusely reflected molecules cannot be the same, implying that the composite stream of all the receding molecules has a non-equilibrium velocity distribution.

When the gas flow is rarefied, the number of intermolecular collisions near the wall surface is insufficient for an equilibrium state to be quickly established be-

tween the approaching and receding streams of molecules. So, it is most unlikely that Maxwell’s assumption of molecules incident to the wall approaching it with an equilibrium velocity distribution holds true. As a phenomenological model, Maxwell’s description of slip velocity can be seen to work well, however, it is not a physical description of molecular behaviour at interfaces in rarefied gas flows. This was openly acknowledged by Maxwell in his original paper [10].

Physically, slip is a difference between the average molecular velocity of a gas and the average molecular velocity of a surface that the gas flows past, which we know as relative tangential momentum. In a non-rarefied gas, we do not observe this difference in the average molecular velocities, it is “instantly” dispersed by intermolecular collisions. This is not true of a rarefied gas flow, where the difference in average molecular velocities is seen to persist as a discontinuity of macroscopic velocity at the boundary.

Fundamentally, rarefied and non-rarefied gases behave similarly, in that energy and momentum are transported through the fluid by intermolecular collisions. For example, if we consider a rarefied but quiescent gas in a solid, stationary container, we know that the fluid will reach a state of equilibrium with its surroundings given sufficient relaxation time². This relaxation time will be significantly longer than the equivalent for a non-rarefied gas. The increase in timescale is due to the larger mean free path of the rarefied gas; the frequency of collisions is lower, slowing the rate of diffusive transport. In the quiescent system, the average molecular velocity of the gas will be zero, as would be true of the oscillating molecules of the stationary container, so there will be no discontinuity of velocity at the gas-surface interface. Thus, slip should be considered as a phenomenon that is highlighted by rarefaction, but is ultimately driven by differences in average molecular velocity that arise when the rarefied gas is in motion relative to a surface.

If we have an established flow of a transitional rarefied gas in a channel, say,

²It should be noted that energy and momentum diffuse at different rates, and technically have different relaxation times [3]. Momentum is exchanged faster than energy, but here relaxation time is taken to mean the total relaxation time for the system, which is the longer, energy transport value.

then the gas flow far from the system boundaries will relax to an equilibrium velocity distribution. The number of molecules is reduced, but the bulk flow will behave, essentially, in the same manner as a non-rarefied equivalent. Away from the channel walls, the gas will have a convection transport timescale that is unaffected by the degree of rarefaction (within the transition regime). The timescale of diffusive transport of momentum and energy in the regions of gas near to the channel walls, however, will be altered by rarefaction. The decreased collision frequency and longer mean free path substantially increase the diffusive relaxation time, as we observed in discussion of the quiescent flow. Thus, the diffusive exchange of momentum between the gas and the system boundaries will take place on a much longer timescale than the convection processes of the bulk flow. Molecules could, then, on average, be transported through the system by the bulk flow before they are able to equilibrate fully with the system boundaries, i.e. before the difference in the average molecular velocity between the gas and the wall is reduced to zero. This would result in a persistent velocity slip at the boundary, and a steady-state but non-equilibrium system.

In practice, the most important difference between rarefied and non-rarefied gas flows is that it is not possible for some rarefied flows to reach an equilibrium state, even if given infinite time to relax. In rarefied gases that are not at rest, there will always exist some degree of velocity slip at surface interfaces, brought on by the loss of local thermodynamic equilibrium. Maxwell's phenomenological model gives a reasonable approximation of the degree of velocity slip in transitional flows, but, as it is not a physical model, there are some serious limitations to its applicability [21].

3.1.3 Boundary effects on temperature

Just as Maxwell's model describes discontinuities of momentum between a moving rarefied gas and its bounding surfaces, so Smoluchowski's phenomenological model describes the equivalent discontinuity of energy between an unequally

heated rarefied gas and surrounding surfaces [11]. Temperature jump is driven by heat flux normal to the wall, rather than a velocity gradient, but can be derived along similar lines to Maxwell’s model [8]. Rather than determining the contribution to shear stress of the approaching molecules’ transferred momentum, Smoluchowski’s model examines the differential energy that the molecules have. That is to say, their energy above or below the average energy of a molecule in an equivalent equilibrium distribution. The thermal accommodation coefficient σ_T is then used to ascribe the temperatures of the receding molecules. Specularly reflected molecules recede from the wall with their original incident energy, and diffusely reflected molecules have their temperatures adjusted to those that would arise in a mass of gas in equilibrium at the temperature of the wall.

For temperature jump at solid boundaries:

$$T_{\text{jump}} - T_{\text{wall}} = A_{\text{jump}} \left(\frac{2 - \sigma_T}{\sigma_T} \right) \left(\frac{2\gamma}{\gamma + 1} \right) \frac{\lambda}{\text{Pr}} \frac{\partial T}{\partial n}. \quad (3.9)$$

The jump coefficient, A_{jump} , has a value of 1 in the original derivation. The specific heat ratio of the gas is represented by γ , and the Prandtl number Pr is used to represent the ratio of momentum diffusivity to energy diffusivity. The gas temperature is T , and n is the direction normal to the wall’s surface.

It is worth noting that in the derivation of Eq. (3.9), it is assumed that internal molecular energy and translatory energy are assumed to be described by the same accommodation coefficient, i.e. that they are transferred at the same rate in intermolecular collisions. This is not in accordance with the theory of equipartition of energy, and is likely to be a source of error in the equation, but given the phenomenological nature of the model, its impact is largely negligible [8].

Of greater concern is the relationship between momentum and energy transfer that is implied when describing the specular and diffuse reflections of Maxwell and Smoluchowski’s models [49]. In practice, the velocity slip coefficient may be shown to be dependent on the level of energy accommodation at the surface, and vice versa, but not in the manner implied by Maxwell and Smoluchowski’s

equations [50]. In Maxwell's Eq. (3.8), for example, diffuse reflection means that molecules leave the wall with an equilibrium distribution of velocity, and are assigned the temperature of the wall. In Smoluchowski's expression, Eq. (3.9), diffuse reflection implies an equilibrium distribution of temperatures is assigned, as if the gas were in equilibrium, with the average temperature being that of the wall [8].

So, the average temperature of the molecules receding from the wall that the models predict is equivalent, but the assumed temperature distribution is not. As outlined in section 3.1.2 above, for the exchange of momentum at bounding surfaces, when the diffusely reflected stream is combined with the specularly reflected stream of molecules, it is unlikely to have an equilibrium distribution of molecular velocities. The same also holds true for temperature distributions.

Consider diffusely reflected molecules that are all assigned the wall temperature value, as in Maxwell's model. The new temperature distribution of the full receding stream will be composed of part of the incident equilibrium temperature distribution, from the specularly reflected molecules, and all of the diffusely reflected molecules will have the same temperature, the wall value. If the diffusely reflected molecules are assigned an equilibrium distribution with the wall temperature as the average value, as in Smoluchowski's model, then, when combined with the specularly reflected molecules, the temperature distribution produced will be different to that obtained using the Maxwellian treatment. The difference in these temperature distributions will have an effect on the degree of departure from equilibrium of the receding stream of molecules and, consequently, an impact on the interaction between approaching and receding streams of molecules that underpins the physical processes of velocity slip and temperature jump. In practical rarefied flows, then, where both energy and momentum are being exchanged in near wall collisions, the validity of using Maxwell and Smoluchowski's expressions in conjunction may be questioned [49].

3.1.4 Alternative slip and jump models

In order to counteract some of the shortcomings of the widely used models for velocity slip and temperature jump, several alternatives have been proposed; although none is widely accepted as a complete replacement for Maxwell and Smoluchowski's conveniently simple expressions.

As an alternative to Maxwell's model, it has been suggested that Langmuir's theory of the adsorption of gases could be used [51]. Adsorption is a process where gas molecules become temporarily attached to a solid bounding surface upon collision with it, and are released again into the bulk flow after some finite time lag. The Langmuir model is based on surface chemistry, but may be shown to make equivalent predictions of slip to Maxwell's model in some key cases [52]. The Langmuir model for velocity slip is given by

$$u_{slip} = \left(\frac{\beta p}{1 + \beta p} \right) u_w + \left(\frac{1}{1 + \beta p} \right) u_g, \quad (3.10)$$

where p is the gas pressure, u_w is the velocity of the gas interacting with the surface, u_g is a local reference velocity elsewhere in the gas and β is the function

$$\beta = \left(4 Kn Pr \omega_0(\nu) \left(\frac{T_w}{T_r} \right)^{1 + \frac{2}{\nu-1}} \exp \left(\frac{-D_e}{k_B T_w} \right) \right)^{-1}. \quad (3.11)$$

Here, $\omega_0(\nu)$ is a tabulated value taken from the kinetic theory of gases, T_w is the wall temperature, T_r a reference temperature, ν is the exponent of the inverse power law for viscosity, D_e is the value of the heat of adsorption, k_B is the Boltzmann constant and Pr the Prandtl number, which describes the relationship between momentum and energy diffusivities.

Although the Langmuir model is obviously more complex than Maxwell's model, its key advantage is that it is possible to determine the slip velocity from knowledge of the chemical interactions between particular gases and surfaces. The properties of surface interactions are both more physical and less open to interpretation than the accommodation coefficient used in Maxwell's model.

Another alternative to Maxwell's slip model is Sharipov's model, in which the Cercignani-Lampis scattering kernel is used to describe molecular interactions at the wall, rather than Maxwell's specular/diffuse scattering model [5, 50]. The Cercignani-Lampis model for the behaviour of molecules receding from the wall is chosen as it contains not one but two accommodation coefficients in the slip velocity: a tangential momentum accommodation coefficient, and a thermal accommodation coefficient. There is also a separate energy accommodation coefficient used in the expression for temperature jump. This type of model gives a more accurate representation of both the physical interactions near the wall, and the interdependence between velocity slip and thermal transpiration effects (creep). Sharipov uses a more realistic description of the collision physics in the near wall region to inform general slip/jump equations and then, using kinetic theory to determine unknown constants, develops accurate expressions for velocity slip and temperature jump. This type of model is an improvement on Maxwell's phenomenological model in that it provides very accurate solutions for particular gas-surface interactions in planar half-spaces. The gas-wall collisions are also handled using more sophisticated and realistic models than Maxwell proposed. Unfortunately, from a practical point of view, this new type of model does not address the real, restrictive limitations of Maxwell and Smoluchowski's models, namely, that they are inaccurate for transitional Knudsen numbers, and that they are not applicable to complex 3D geometries without the risk of substantial error.

Ultimately, while both Langmuir and Sharipov's models (and several other alternatives, see [3, 53, 54]) are more accurate than Maxwell and Smoluchowski's expressions, in application they must be considered less robust. Generally, alternative models are relatively complex and require available kinetic theory data, which, for practical flows and most engineering design applications renders them largely unsuitable. Also, it is difficult to justify the complexity of implementing models that are dependent on individual gas-surface interaction properties, but

derived only for simple flow configurations (typically planar surfaces, and often isothermal cases). Large accuracy losses can occur when converting kinetic-theory dependent models to 3D, non-isothermal, compressible and transitional- Kn flows, which can negate the benefits of using kinetic-theory based slip models altogether in practical flows. As yet, no alternative to Maxwell or Smoluchowski's models has been widely accepted as suitable, particularly for application to complex flows.

3.2 The Knudsen layer

The Knudsen layer is a near-wall region approximately one to two mean free paths in thickness where local thermodynamic equilibrium is not maintained. Microscopic interactions in the Knudsen layer do not generate equilibrium distributions of the macroscopic variables. In rarefied flows, velocity slip and temperature jump arise within the Knudsen layer as the difference in the average molecular properties of the wall and those of the gas at the wall. The Knudsen layer thickness is the average distance over which these discontinuities would be equilibrated in a quiescent gas.

Macroscopically, the Knudsen layer is observed as a region of flow exhibiting strong departures from the linear constitutive behaviour of the N-S-F equations: the relationships between stress/strain-rate and heat flux/temperature-gradient are nonlinear. As gas flows reach transitional- Kn values, moving from regime B to C as outlined in section 2.1, the structure of the Knudsen layer becomes important. For example, in cases of pressure-driven gas flow in a microchannel with the relatively modest rarefaction of $Kn = 0.05$, velocity slip may be shown to increase the observed mass flowrate by 15%. The nonlinear structure of the Knudsen layer accounts for 30% of this difference between the “true” microscopic velocity profile and that predicted by the N-S-F equations [37].

To illustrate, a schematic of the Knudsen layer structure is given in Fig. 3.2. The figure shows Knudsen layer velocity profiles for an isothermal, pressure-driven

gas flow, moving parallel to a planar wall. The velocity of the wall is denoted by u_{wall} , and the actual speed of the gas at the wall by u_{slip} . The solid line indicates the true velocity of the gas, which is commonly referred to as the microslip, as would be found in experimental results or predicted in accurate molecular dynamics simulations [3, 6, 8].

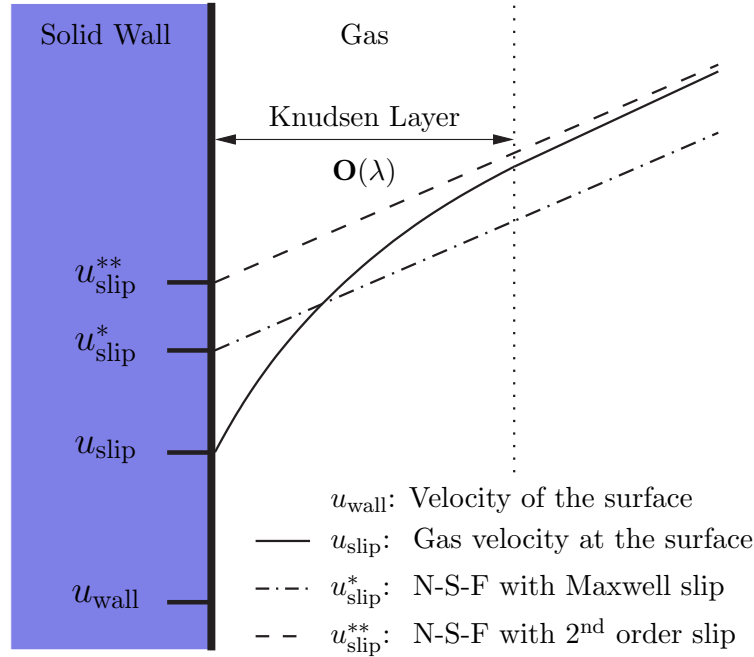


Figure 3.2: Schematic of the velocity structure of the Knudsen layer near a wall in a pressure-driven flow, comparing different types of slip boundary condition.

The dash-dot line represents the velocity profile obtained using the N-S-F equations with Maxwell’s velocity slip condition, Eq. (3.8), giving the slip value u_{slip}^* at the wall. Although this model over-predicts slip at the boundary, outside of the Knudsen layer it under-predicts the velocity slightly, and gives a reasonable approximation of the velocity gradient. Far from the wall in transitional- Kn flows, where the assumed equilibrium velocity/temperature distributions hold, the N-S-F equations are appropriate. Therefore, beyond the Knudsen layer, they may be used in conjunction with Maxwell’s equation for boundary slip to predict the mass flowrate in moderately high- Kn systems with acceptable accuracy. As Kn increases, however, Maxwell’s model increasingly under-predicts the gas

velocity outside of the Knudsen layer, until eventually the level of error in the results becomes unacceptable [21, 49].

In order to improve the mass flowrate prediction of the N-S-F equations with slip, particularly at high- Kn , it is common to use higher-order slip/jump boundary conditions, which are often referred to as macroslip conditions [3, 6, 21]. These macroscopic boundary conditions deliberately over-predict the velocity slip at the surface interface, in order to more accurately capture the velocity profile outwith the Knudsen layer, as shown in Fig. 3.2 by the dashed line, u_{slip}^{**} .

Higher-order slip models are typically derived using series expansions of the simplest form of Maxwell's equation: that for isothermal flows in planar geometries, Eq. (3.5). For example, Cercignani proposed a second order model for slip at the wall of the form

$$u_{\text{slip}}^{**} = A_1 \lambda \frac{du}{dy} - A_2 \lambda^2 \frac{d^2u}{dy^2}, \quad (3.12)$$

where A_1 and A_2 are the first and second order slip coefficients, du/dy the velocity gradient and λ the mean free path [55]. Like Maxwell's model, this expression for slip is dependent on the mean free path definition and, hence, molecular force-interaction law applied. For the hard-sphere molecular model, the slip coefficients would be $A_1 = 1.1466$ and $A_2 = 0.647$ [56].

Other higher-order models, however, use different slip coefficients. For example, Deissler [57] suggests values of 1.0 and 1.125 for A_1 and A_2 , respectively, while Karniadakis and Beskok [21] propose 1.0 and -0.5 . Whilst some authors agree with Cercignani's coefficients, these models and several others do not match even the first-order slip coefficient, and there is no universal agreement as to the most accurate general model [3, 21, 57, 58]. So, despite the useful potential to extend the applicability of the N-S-F models by introducing macroscopic slip effects to match observed mass flowrates, the lack of agreement on correct slip coefficients greatly detracts from the generality of higher-order slip models.

Several other factors also limit the appeal of second-order slip for engineering

applications. Typically, macroslip models are derived from the simplified form of Maxwell's equation, Eq. (3.5), which is not suitable for curved surfaces, and neglects thermal creep. Thus, in non-isothermal and compressible flows, it is likely that the error introduced by neglecting surface geometry and thermal creep would negate the benefits of having a second-order-accurate model.

Returning to Fig. 3.2, we see that there are two main differences between the N-S-F models with slip boundary conditions and the true velocity of the gas. Firstly, the velocity gradient is much steeper in the Knudsen layer region of the real gas — the Maxwellian equilibrium-velocity profile coming from the bulk of the flow does not really extend all the way to the wall. Secondly, this increase in the velocity gradient means that the true slip of the gas at the wall is lower than the value Maxwell's model predicts. There is some debate about the exact magnitude of the microslip coefficient (for first order slip), but it can be shown from kinetic theory solutions for the near-wall region to be ≈ 0.8 for both velocity slip and temperature jump [16, 17]. So, we know that Maxwell's model and other macroslip models can be used in some circumstances to improve predictions of bulk quantities, such as mass flowrate or drag force on a surface, but, also that ultimately, they do not capture the true physics of the Knudsen layer.

Chapter 4

Constitutive scaling

4.1 Introduction

At transitional- Kn and in the upper slip flow regime, the effects of the non-equilibrium Knudsen layer must be incorporated into numerical simulations to obtain accurate results for the macroscopic properties of the flow. Constitutive scaling, where the relationship between viscous stress and strain-rate (and/or heat flux and temperature gradient) in the near wall region is modified to represent Knudsen layer behaviour, is one numerically economical approach to incorporating the Knudsen layer in continuum analyses. This technique uses linearised kinetic theory results to determine a phenomenological function $f(n/\lambda)$ with which to scale the N-S-F constitutive relations. The method was originally proposed by Lockerby *et al.* [12] for application to isothermal cases. In Lockerby *et al.*'s paper, Knudsen layer behaviour is incorporated into N-S-F simulations by scaling the relationship between shear stress and strain-rate in planar flows, i.e. the relationship given in Eq. (3.1):

$$\tau = \mu \frac{du}{dn} \implies \tau = \frac{1}{f(n/\lambda)} \mu \frac{du}{dn}. \quad (4.1)$$

The scaling is a function of the normal distance to the nearest surface n , and the local mean free path λ , and therefore directly relates to changes in Kn . The scaling function is chosen such that $f(n/\lambda) \rightarrow 1$ with decreasing Kn , restoring the linear relationship between stress and strain-rate assumed in the N-S-F equations.

Hence, the constitutive scaling approach also remains valid as $Kn \rightarrow 0$.

To determine an appropriate scaling function, Lockerby *et al.* [12] used linearised kinetic theory results for Kramers' problem, a half-space shear flow over a planar surface [3]. A schematic of Kramer's problem is shown in Fig. 4.1.

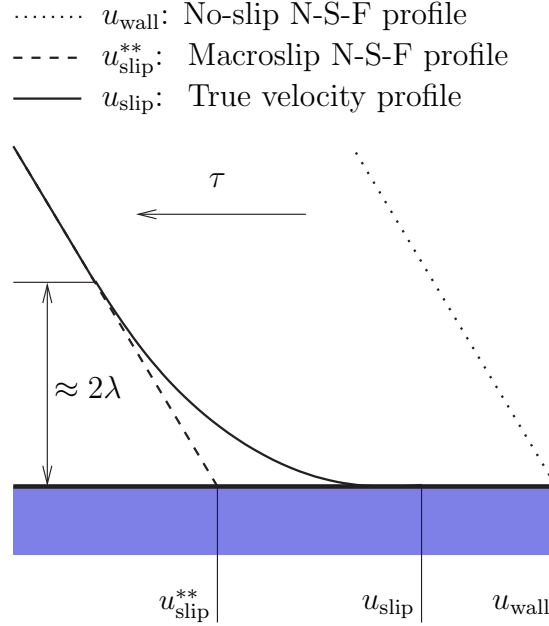


Figure 4.1: Sketch of Kramers' problem flow configuration showing applied constant shear stress, τ ; traditional, no-slip N-S solution (u_{wall} : dotted line), N-S solution with second order macroslip boundary condition (u_{slip}^{**} : dashed line) and true velocity profile (u_{slip} : solid line). The Knudsen layer extends approximately 2λ from the wall surface.

Kinetic theory indicates that the Knudsen layer velocity profile in a monoatomic gas that is subject to a uniform shear stress and flows over a planar surface is given by

$$u = -\frac{\tau}{\mu} (n + \xi - \lambda I(n/\lambda)), \quad (4.2)$$

where τ is the uniform shear stress, μ is the gas viscosity, and ξ is a constant [3]. The velocity correction function $I(n/\lambda)$ introduces the deviation from a linear strain-rate profile, i.e. the change in shape from the dotted u_{wall} or dashed u_{slip}^{**} profiles to the solid u_{slip} profile as shown in Fig. 4.1. The function can be curve-fit

from kinetic theory data given in [3] to be:

$$I(n/\lambda) \approx \frac{7}{20} \left(1 + \frac{n}{\lambda}\right)^{-2}. \quad (4.3)$$

Although kinetic theory is used to define the scaling function used in [12], it is worth noting that it would be equally possible to use direct-simulation Monte Carlo (DSMC), molecular dynamics (MD) or experimental data to determine case-specific scaling functions for $I(n/\lambda)$. In practice, this could allow the constitutive scaling method to be extended to flows of polyatomic gases.

Differentiating Eq. (4.2) produces an expression for strain-rate, which is appropriate throughout the near-wall Knudsen layer region of the flow:

$$\frac{du}{dn} = -\frac{\tau}{\mu} f(n/\lambda). \quad (4.4)$$

This expression is then recast into the form of the expressions in Eq. (4.1), and used in place of the linear N-S-F relation, Eq. (3.1). Mathematically the result is equivalent to using an “effective” viscosity model,

$$\tau = \mu_{\text{eff}} \frac{du}{dn}, \quad (4.5)$$

where the effective viscosity is given by $\mu_{\text{eff}} = \mu/f(n/\lambda)$. Although Eq. (3.1) describes the relationship between shear stress and velocity gradient in one spatial dimension only, the variation of the effective viscosity in Eq. (4.5) is with normal distance to the nearest surface, n , rather than a single plane. This allows the scaling effect to be realised in 3D when the full Navier-Stokes stress tensor is used to determine τ . The final shape of the viscosity scaling function $f(n/\lambda)$ is given in [12] as

$$f(n/\lambda) = 1 - \lambda \frac{d}{dn} [I(n/\lambda)] \approx 1 + \frac{7}{10} \left(1 + \frac{n}{\lambda}\right)^{-3}. \quad (4.6)$$

Using this function $f(n/\lambda) \rightarrow 1.7$ as $n \rightarrow 0$. When Kn is in the continuum regime the extent of the Knudsen layer ($\approx 2\lambda$) is small in comparison to the system

dimensions, so constitutive scaling effects imposed by this function automatically become negligible when it is applied to continuum flows (i.e. as $Kn \rightarrow 0$).

Derived from a kinetic solution for a relatively low speed, planar flow of monoatomic gas subject to uniform shear stress, this scaling model should be limited strictly in applicability to cases of that type. The basic assumptions underpinning the kinetic theory solution include a restriction to low Mach number flow, relatively low Kn values, and planar surfaces with diffuse molecular reflection. It has been shown, however, that this particular scaling model can improve, both qualitatively and quantitatively, numerical results for flows that are beyond these limitations. For example, the model has been successfully applied to flows over non-planar surfaces [12, 14, 36].

4.1.1 State of the art

Constitutive scaling as a technique was proposed by Lockerby *et al.* only relatively recently, in 2005 [12]. The primary advantage of the method is that Knudsen layer structures can quickly and easily be incorporated into standard N-S-F simulations. This extends the applicability of these relatively fast continuum analyses for microsystem design applications, where flexibility and low computational cost are essential. The original model, given in Eq. (4.6), was intended as a simple means of capturing the Knudsen layer in isothermal flows, and was intended for primarily planar cases. Using previous work on Maxwell's boundary conditions carried out in [16], Lockerby *et al.* then extended the method to include curved surface geometries, analysing viscous drag over an unconfined microsphere. The method has also been applied to a quiescent thermal flow in planar half-space geometry, giving a successful prediction of the temperature profile normal to the wall [36]. Limitations of the constitutive scaling method as originally proposed were that it had not been applied to complex geometries, compressible non-isothermal flows, or to cases where both energy and momentum exchanges are considered, e.g. non-quiescent thermally-driven flows, or shear/pressure-driven

flows with heat transfer effects.

In an attempt to improve the accuracy and generality of the constitutive scaling method, Reese *et al.* [17] and Zheng *et al.* [45] proposed new scaling functions for Knudsen layers of both momentum and energy. Kinetic theory data from a wide literature survey were used to determine separate scaling functions for effective dynamic viscosity, μ , and effective thermal conductivity, κ . Thermal conductivity is the material property that is used in the N-S-F equations to linearly relate heat flux and temperature gradient;

$$\mathbf{Q} = \kappa \frac{\partial T}{\partial n}. \quad (4.7)$$

In the same way that dynamic viscosity is replaced with an effective quantity in Eq. (4.5), the thermal conductivity may be scaled by a phenomenological function to produce a Knudsen layer structure. Constitutive scaling for thermal Knudsen layers replaces the constant thermal conductivity found in Eq. (4.7) with an effective quantity;

$$\mathbf{Q} = \kappa_{\text{eff}} \frac{\partial T}{\partial n}. \quad (4.8)$$

Crucially, the use of different scaling for viscosity and thermal conductivity in these models implies a non-constant effective Prandtl number (which relates energy and momentum diffusivities) when they are used together [49]. It is possible that this therefore highlights some physical inconsistency in the models, which needs further investigation if they are to be considered as a means of extending the applicability of constitutive scaling to more complex flows.

More recently, Lockerby and Reese [59] have proposed a scaling function derived from the Bhatnagar-Gross-Krook (BGK) kinetic model. It is designed for use in constitutive scaling in conjunction with a second order velocity slip condition. Although it is seen to improve the performance of the model as a whole, the use of a second order slip boundary condition remains inherently unphysical as it does not represent a Knudsen layer. Whilst constitutive scaling is not in itself a

means of producing a physical model, the intent is to replicate observed Knudsen layer behaviour. Second order slip conditions do not model the true physics of gas-surface interactions, but are used solely to improve the performance of simulations beyond the extent of the Knudsen layer. However, this most recent paper very accurately replicates BGK results for shear-driven and pressure-driven microchannel flows and, notably, demonstrates that using a BGK based function, it is theoretically possible to predict the “Knudsen minimum¹” using constitutive scaling. This most recent work has not yet been extended by Lockerby *et al.* to include thermal effects, nor has the BGK-based model been applied to non-planar geometries.

Several other research groups have also now taken an interest in approaches similar to the constitutive-scaling process, and some even propose alternate scaling functions for various gas microflow configurations. Fichman and Hetsroni [62], for example, consider a reduction of dynamic viscosity in near-wall regions of rarefied flows. Their analysis uses arguments similar to those of Maxwell [10] insofar as their scaling of the dynamic viscosity as a function of mean free path and distance from the surface interface is dependent on the proportion of molecules reflected specularly/diffusely. They find the actual gas viscosity at the surface interface to reduce to one half of its original free-stream value. This is comparable to the original work of Lockerby *et al.* [12], which scales dynamic viscosity with normal distance to the nearest wall, reducing to a value of 0.59 times the free-stream viscosity at the surface [49].

Lilley and Sader [63] have also proposed modelling rarefied flows as non-Newtonian fluids, which is mathematically equivalent to scaling the constitutive relations of the N-S-F equations. They put forward a scaling function that is curve-fit to linearised solutions to the Boltzmann equation for Kramers’ problem, as published by various authors [64–67]. The premise of their paper is that

¹In experimental work confirmed by Gaede [60], Knudsen [61] showed experimentally that the volume flowrate of rarefied gas through a channel reaches a minimum value at $Kn \approx 1$, and increases with increasing Kn beyond that condition. This is commonly referred to as the Knudsen minimum [8].

both the linearised Boltzmann equation and DSMC give very similar results for Kramers' problem, and the velocity profiles from those solutions may be represented using a power-law function, which can be translated to a variation of effective viscosity. Notably, Lilley and Sader's use of a power law curve fit for the velocity profile, implies that the velocity gradient need not be finite at the surface. For example, using

$$u(y) = a + by^c \quad (4.9)$$

as a curve fit for the velocity, where y is the distance from a planar wall and a , b and c are constants, the velocity gradient at the surface would be

$$\frac{du}{dy} = \frac{cby^c}{y}. \quad (4.10)$$

So, as $y \rightarrow 0$ approaching the surface, the velocity gradient would indeed become infinite. The authors use this fact to suggest that since the velocity gradient at the wall is infinite, and the effective viscosity a function of the velocity gradient, then the effective viscosity at the wall would become zero. This is specifically a consequence of the power-law curve fit, however, and not necessarily a physical property of the flow. Had the velocity profile been approximated using another type of curve fit, then no such singularity would appear. Also, the authors state that they consider fully diffuse molecular reflection at the surface interface. As described in section 3.1.2 of the previous chapter, diffuse reflection implies that the tangential momentum of gas molecules is altered in collisions with the wall from the incident velocity distribution to a new, effusive velocity distribution. If the effects of this exchange of momentum extend into the flow as the non-linear Knudsen layer, then physically some finite viscosity is implied. This is not consistent with the authors' findings of zero effective viscosity at the surface.

Cercignani *et al.* [68] have also recently proposed viscosity scaling as a tool for analysing microsystems in engineering applications. In their 2007 paper [68], fluid moving in and around a comb drive is modelled, where the flow is taken

to be a combination of Couette and Poiseuille flows (i.e. a combination of shear-driven and pressure driven flow). The authors of the paper propose two different effective viscosities, one for the Couette flow in the device and another for the Poiseuille type flow. These two effective viscosities are then combined into a model for the total force on the device structure that is exerted by the fluid, with coefficients balancing the influence of the effective viscosity for the Couette and Poiseuille proportions of the flow. The coefficients are determined numerically, and optimised to produce results that are accurate in comparison to experimental data available for the particular device analysed [68]. In this paper, the authors are able to use experimental data to carefully fine-tune their continuum solutions for fluid flow. This is a very useful validation of the scaling approach, which highlights the need for constitutive-relation scaling to be informed by reliable data sources. Where experimental data are available for comparison, it is possible to produce very useful models, which can be tailored effectively for device design.

In summary, the constitutive-relation scaling approach is a simple but effective method for incorporating Knudsen layer simulation into N-S-F models. The approach was proposed originally by Lockerby *et al.* [12], who have worked with their group and collaborators to further it [17, 36, 45, 59]. Other research groups have also attempted to move the approach forward and have proposed similar strategies [62, 63, 68]. To date, however, none of these models are implemented in mainstream CFD codes and most are for incompressible and/or isothermal flows in planar geometry. This thesis exploits the potential of the constitutive scaling method by developing it for application to compressible flows within a flexible CFD framework, to produce a design-focused tool for analysing fluid flow and heat transfer in gas microsystems. Momentum Knudsen layers, which are fundamental to almost all physical cases, are the primary focus of this research, although thermal Knudsen layers are included in later models where gas compressibility is considered.

4.2 OpenFOAM: a CFD framework

To meet the eventual aim of creating a flexible tool for fully compressible gas microsystem design, the open-source CFD package OpenFOAM has been selected as a suitable numerical framework for constitutive scaling [13]. OpenFOAM (Open-source Field Operation and Manipulation) is a finite-volume numerics package designed to solve systems of differential equations in arbitrary 3D geometries, using a series of discrete C++ modules. These modules are modifiable by the end user which, in this instance, allows the incorporation of slip/jump boundary conditions and the integration of the constitutive scaling method with reliable pre-existing N-S-F solvers.

The modules supplied in the OpenFOAM release include a range of solvers, utilities and libraries that are used both to pre- and post-process and to simulate cases. The structure of OpenFOAM is hierarchical, allowing the user to fully extend the capabilities of, say, a solver application, whilst retaining the benefits of a general notation and stable numerical framework. The case structure of OpenFOAM is also open, in that each case comprises accessible and human-readable files detailing the mesh, boundary conditions and system conditions under which it is to run. Flexibility and modularity are the key features that make OpenFOAM attractive as the numerical framework in which to extend the N-S-F equations for CFD simulations of rarefied gas flows.

4.3 Incompressible solver: icoFoam

The OpenFOAM application icoFoam solves the Navier-Stokes equations for incompressible, isothermal flows of Newtonian fluids. The equations are implemented in tensor form, as shown below.

<pre>fvVectorMatrix UEqn (fvm::ddt(U) + fvm::div(phi, U) - fvm::laplacian(nu, U)); solve(UEqn == -fvc::grad(p));</pre>	<p>icoFoam Eqns.</p> $\frac{\partial \mathbf{U}}{\partial t} + \nabla \cdot (\phi \mathbf{U}) - \nabla \cdot \nu \nabla \mathbf{U} = -\nabla p_d$
--	---

The equations use the kinematic viscosity ν , and the pressure p_d is equal to the static pressure p divided by the density ρ , that is to say, density is assumed to be constant and uniform. The mass flux ϕ is given by $\phi = \rho \mathbf{U}$ from continuity. The equations are posed in general transport form, comprising (from top to bottom) a transient term, convective term, diffusive term and a source term, which in this case is the pressure gradient. If this value is unspecified in the OpenFOAM case, the equation is solved for $\nabla p_d = 0$.

Each of the terms in the governing equations is discretised using one of a range of numerical schemes that are individually specified in each solver. A typical incompressible case would use an implicit Eulerian discretisation for the transient term, a Gaussian discretisation with linear interpolation between cell-centre values and face-centre values for the convective terms and source terms, and a slightly different Gaussian scheme for the diffusive term. The diffusive discretisation scheme would typically use a linear interpolation for the diffusion coefficient, ν in the example above, and a corrected (explicit, non-orthogonal) numerical discretisation for the surface-normal gradient, $\nabla \mathbf{U}$, which is generally a conservative scheme for incompressible cases. Full details of the discretisation procedure and the numerical schemes are given in the OpenFOAM Programmer's Guide and User Guide [69, 70].

4.3.1 Boundary conditions

OpenFOAM is supplied with a range of physical boundary conditions, such as solid surfaces and symmetry planes, in addition to boundary conditions for the simulated fluid. The fluid boundary conditions are derived from a small range of primitive types. The most common types are fixed boundary value (Dirichlet) or fixed boundary gradient (Neumann). Composite derivatives of these boundary conditions are also implemented, including a “mixed” condition, which is a weighted blend of the Dirichlet and Neumann types. This mixed fixed-value/fixed-gradient boundary condition is the basis for incorporating Maxwell’s velocity slip model, Eq. (3.8), in OpenFOAM.

Maxwell’s slip model is not included as part of the OpenFOAM general release, but has been implemented in the package as outlined in [71] as part of ongoing research at the University of Strathclyde. The slip boundary condition was originally implemented without the slip coefficient A_1 , therefore only representing Maxwell’s original equation with a slip coefficient $A_1 = 1$. So the slip coefficient has been added to the code as part of this thesis to allow the true microslip coefficient to be used when Knudsen layer models are employed, and to allow a wider range of first and second order slip models to be tested in OpenFOAM. Thermal creep effects are also not included in incompressible, isothermal applications in OpenFOAM.

4.4 OpenFOAM for non-equilibrium flows

The Knudsen layer is incorporated into OpenFOAM using the constitutive scaling technique. The scaling of constitutive relationships is achieved in OpenFOAM with the introduction of effective viscosity models, known in the code as “transport models”. These may be introduced in a similar fashion to any other non-Newtonian transport model such as, for example, Sutherland’s viscosity law.

In order to incorporate non-Newtonian fluid dynamics, the icoFoam solver ap-

plication must be modified. Firstly, if the viscosity is no longer constant, then the momentum equations must be altered to include viscosity as a variable quantity to be updated at each time step. This is carried out in accordance with the procedures followed in a variant OpenFOAM solver, nonNewtonianIcoFoam. In the icoFOAM momentum equations, given above, references to kinematic viscosity `nu` are replaced with `fluid.nu()`, and the function `fluid.correct()` is called to update the viscosity appropriately in the solver's main iterative loop.

Secondly, the constitutive scaling method as implemented by Lockerby *et al.* [12], the first constitutive model to be tested in this thesis, employs effective viscosity as a function of distance to the nearest solid surface. Written fully, the Navier-Stokes stress tensor is

$$\boldsymbol{\tau} = \mu \nabla \mathbf{U} + \mu \nabla \mathbf{U}^T - \frac{2}{3} \mu \text{tr}(\nabla \mathbf{U}) \mathbf{I}, \quad (4.11)$$

where the superscript T denotes the transpose ($\mathbf{U} = U_{ij}$, $\mathbf{U}^T = U_{ji}$), and \mathbf{I} the identity tensor. The trace of the strain-rate tensor is $\text{tr}(\nabla \mathbf{U})$, which is the sum of its diagonal components, in this case referring to the deviatoric stresses.

In the Navier-Stokes momentum equations, shown in Eq. (2.6), the divergence of the stress tensor, $\nabla \cdot \boldsymbol{\tau}$, is the diffusive transport term. Combining this term from Eq. (2.6) and Eq. (4.11) above, we find

$$\nabla \cdot \boldsymbol{\tau} = \nabla \cdot (\mu \nabla \mathbf{U}) + \nabla \mu \left(\nabla \mathbf{U}^T - \frac{2}{3} \text{tr}(\mathbf{U}^T) \mathbf{I} \right). \quad (4.12)$$

When viscosity is constant and uniform, as it should be in an incompressible, isothermal Navier-Stokes solution, the second term in Eq. (4.12) is premultiplied by $\nabla \mu = 0$, and is hence omitted from the standard icoFoam code for efficiency. Thus, for constant viscosity,

$$\nabla \cdot \boldsymbol{\tau} = \nabla \cdot (\mu \nabla \mathbf{U}) = \mu \nabla^2 \mathbf{U} \quad (4.13)$$

represents the diffusive transport term in the icoFoam momentum equations.

When introducing a spatially-varying viscosity as part of the constitutive scaling procedure, however, it is necessary to include the complete Navier-Stokes stress tensor. It is no longer valid to neglect the second term on the right hand side of Eq. (4.12), which couples the new effective viscosity and the velocity gradient. The inclusion of this term, in kinematic-viscosity form, is the final modification to the momentum equations necessary to implement the constitutive-scaling technique in icoFoam. These changes form the basis of a new OpenFOAM solver, which is known as microIcoFoam.

fvVectorMatrix UEqn (microIcoFoam Eqns.
fvm::ddt(U)	$\partial \mathbf{U} / \partial t$
+ fvm::div(phi, U)	$+\nabla \cdot (\phi \mathbf{U})$
- fvm::laplacian(nu, U)	$-\nabla \cdot \nu \nabla \mathbf{U}$
- fvc::grad(fluid.nu() & dev2(fvc::grad(U)().T()))	$-\nabla \nu \cdot (\nabla \mathbf{U}^T - \frac{2}{3} \text{tr}(\mathbf{U}^T) \mathbf{I})$
);	=
solve(UEqn == -fvc::grad(p));	∇p_d

4.4.1 Implementing effective viscosity

In practice, the most convenient method of implementing constitutive scaling in OpenFOAM is to make use of existing structures for non-Newtonian fluid dynamics, and create a specific “effective viscosity fluid”. Before implementation, the constitutive expression for effective viscosity μ_{eff} is re-cast into an expression for effective mean free path λ_{eff} based on normal distance to the nearest wall n :

$$\lambda_{\text{eff}} = \frac{\lambda_{\text{original}}}{f(n/\lambda_{\text{original}})}, \quad (4.14)$$

where $\lambda_{\text{original}}$ is the equilibrium mean free path based on the un-scaled constitutive coefficients (e.g. dynamic viscosity), given by Eq. (2.2) for the hard-sphere

gas model. For the original scaling function Eq. (4.6) proposed by Lockerby *et al.* [12], Eq. (4.14) then becomes

$$\lambda_{\text{eff}} = \frac{\lambda_{\text{original}}}{1 + \frac{7}{10} \left(1 + \frac{n}{\lambda}\right)^{-3}}. \quad (4.15)$$

The definition of molecular mean free path given in Eq. (2.2) is then used to define an effective dynamic viscosity as a function of the effective mean free path:

$$\mu_{\text{eff}} = \frac{\rho \lambda_{\text{eff}}}{\sqrt{\frac{\pi}{2RT}}}. \quad (4.16)$$

One motivation to do this is that in real systems it is postulated that some shortening of the mean free path of the gas would occur in the Knudsen layer region. Detailed molecular dynamics simulations of gas/wall interaction are needed to confirm this hypothesis, however it makes some physical sense. Shortening of the mean free path could occur near surfaces due both to gas-solid collisions, and to the interaction between gas molecules incident to the surface and those reflected from it. Molecules reflected from a solid surface have their velocity distribution ascribed by the slip equation, Eq. (3.8). They are assumed to be reflected diffusely when their incident tangential momentum and energy is completely equilibrated with the solid surface. There is no restriction, however, on the number of collisions an individual molecule may have within the confines of a rough surface for this condition to be met (i.e. adsorption can take place). If intermolecular collisions between gas molecules and wall molecules are included in the definition of local mean free path of the gas, then it also stands to reason that the mean free path could be shorter in the near-wall region.

4.4.2 Maxwell's slip and constitutive scaling

The primary motivation for the use of an effective mean free path in constitutive scaling models is that the strain-rate in Maxwell's slip model, Eq. (3.8), which is equal to τ/μ , increases when the original viscosity is replaced with an effective viscosity. This occurs as the effective viscosity is lower than the original viscosity

in the near-wall region, allowing any given shear stress to generate a higher strain-rate representing the Knudsen layer.

By including the effective viscosity as a function of mean free path, which is, in turn, a function of wall-normal distance, it is possible to use the true strain-rate at the wall to determine the slip velocity. In constant shear-stress problems, such as Couette flow, the correct shear-stress profile is therefore maintained despite the variation in strain-rate observed through the Knudsen layer. This cannot be said of other constitutive-scaling implementations, which rely on separate calculation of the viscous stress arising from an equivalent equilibrium strain-rate profile [72].

4.5 Progress summary

In summary, at this point, the key physical effects of gas rarefaction at transitional- Kn that impact microsystem design have been identified. For incompressible and isothermal flows these are velocity slip, and the presence of a Knudsen layer in the velocity field, which is caused by the incomplete exchange of momentum between gas molecules and wall molecules. For non-isothermal flows, temperature jump at system boundaries and temperature-profile Knudsen layers, caused by incomplete exchange of thermal energy, are also relevant. Suitable mathematical models for key non-equilibrium effects have been reviewed and the most practical chosen for implementation into a CFD-based design tool. For velocity slip and temperature jump, Maxwell [10] and Smoluchowski's [11] phenomenological models will be used, and for the Knudsen layer, a constitutive scaling approach will be taken, see e.g. [12].

OpenFOAM has been identified as the most suitable mainstream CFD package for the development of a design tool for gas microsystems, as it is both flexible and highly extensible [13]. Modifications to the OpenFOAM source code have been made to produce a new incompressible, isothermal solver that incorporates the effects of velocity slip and the momentum Knudsen layer. The most notable feature of the new solver is that it brings together gas rarefaction effects and

practical applicability, in that it is implemented in full 3D form. This is the first time that the constitutive scaling method has been applied in a full finite-volume CFD framework, and represents substantial development of the method in itself.

These modifications are, of course, only the first stage in the evolution of a microsystem CFD tool that is applicable to fully compressible and non-isothermal flows. The next stage in the development process is the verification of the implemented models, which will be described in the next chapter. Only following successful verification of the incompressible solver will the model be extended to compressible flows.

Chapter 5

Incompressible flows

5.1 Introduction

In this chapter the OpenFOAM implementations of Maxwell slip and constitutive scaling are both verified and validated. Verification is defined in [73] as

The process of determining that a model implementation accurately represents the developer’s conceptual description of the model and the solution to the model.

In the context of this thesis, verification implies ensuring that the implemented descriptions in the OpenFOAM numerical framework accurately correspond to the original mathematical models for slip [10] and isothermal constitutive scaling [12]. Analytical solutions to the Navier-Stokes equations for flow in planar channels are used for verification. Two key case types are examined: pressure-driven Poiseuille flow, and shear-driven Couette flow. In section 5.2, Poiseuille flow velocity profiles from OpenFOAM are compared to analytical solutions to examine both Maxwell’s slip boundary condition and the constitutive-relation scaling model. Worked analytical solutions are given in appendix A, and details of other relevant numerical analysis are given in appendix B.

In section 5.3 Couette flow results from OpenFOAM are compared to analytical solutions and alternative numerical methods for verification, and to DSMC results for validation, where validation is defined as [73]

The process of determining the degree to which a model is an accurate representation of the real world from the perspective of the intended uses of the model.

Details of the analytical solutions to Couette flow are given in appendix C, and alternative numerical solutions are described in appendix D.

Following successful verification and validation, in sections 5.4 and 5.5 the microIcoFoam solver is used to analyse rarefied gas flows in more complex cases, including channels with orifice plate and venturi constrictions, and flow between rotating concentric cylinders.

5.2 Poiseuille flow

Poiseuille flow is the name traditionally given to flow of viscous fluid in a channel or pipe driven by a constant pressure gradient (or acceleration), where pressure decreases in the direction of the flow. Figure 5.1 shows a schematic of planar Poiseuille flow in a 2D channel with parallel walls.

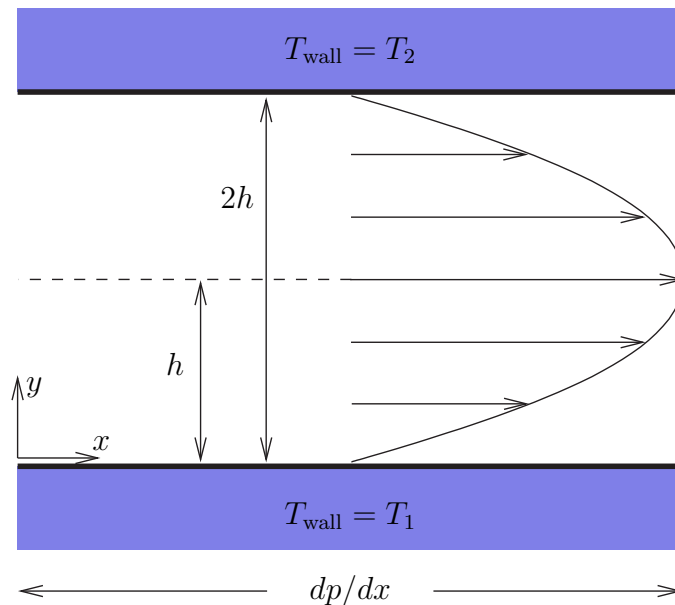


Figure 5.1: Schematic of Poiseuille flow configuration with velocity profile.

The channel height is $2h$, and the longitudinal pressure gradient driving the flow is $-dp/dx$. A sketch of the velocity profile for fully developed Poiseuille flow is shown in the figure. The flow is assumed to be fully developed and in a steady state. In this chapter the case is treated as isothermal, with the upper and lower wall temperatures T_2 and T_1 taken to be equal for the purposes of determining the properties of the gas in the channel.

When non-rarefied Poiseuille flow is fully developed its cross-channel velocity profile is parabolic. Rarefaction alters the shape of this velocity profile, but at any Kn the profile remains constant along the length of the channel. As such, this type of flow may be considered as a special 1D case. For a Newtonian fluid, the governing equation for the Poiseuille flow case shown in Fig. 5.1 is obtained by reducing Eqs. (2.5) and (2.6) to obtain a general solution:

$$\frac{dp}{dx} = \frac{d}{dy} \left(\mu \frac{du}{dy} \right). \quad (5.1)$$

An exact analytical expression for the velocity profile across the channel, $u(y)$, can then be obtained from the general expression given in Eq. (5.1) when two independent boundary conditions are known. At the channel centre $y = h$, the derivative of the velocity profile is zero as the profile is parabolic: $du/dy = 0$. In low- Kn flows, the no-slip boundary condition applies at channel walls: $u(y) = 0$ at $y = 0$. When these boundary conditions are applied to Eq. (5.1), an expression for Poiseuille flow in the continuum flow regime is established¹:

$$u(y) = \frac{1}{\mu} \frac{dp}{dx} \left(\frac{y^2}{2} - hy \right). \quad (5.2)$$

As Kn increases beyond ≈ 0.001 flows enter the slip regime, where boundary conditions such as Maxwell's slip boundary condition, Eq. (3.8), are used. The isothermal analytical solution for the cross-channel velocity profile obtained when using Maxwell's expression is

¹Full details of the solution procedures for analytical solutions are given in appendix A.

$$u(y) = \frac{1}{\mu} \frac{dp}{dx} \left(\frac{y^2}{2} - hy \right) - A_1 \left(\frac{2 - \sigma_U}{\sigma_U} \right) \frac{\lambda}{\mu} \tau_w. \quad (5.3)$$

where τ_w represents the shear stress evaluated at the channel wall.

In the upper slip flow and early transition regimes of Kn , Knudsen layer effects begin to alter the velocity profile of Poiseuille flow [12, 74]. To represent rarefaction effects, constitutive scaling has been implemented in OpenFOAM. It is also possible to determine analytical expressions for the Navier-Stokes solution including the effect of constitutive scaling, although these solutions are considerably more complex than standard results such as Eqs. (5.2) and (5.3)². Constitutive scaling is only applied in conjunction with appropriate microslip boundary conditions. In the case of Maxwell's slip model, the slip coefficient A_1 is reduced to ≈ 0.8 to give the true slip at the wall [12].

When Eq. (4.6), as proposed in [12], describes the shape of the constitutive scaling function, the analytical expression for the velocity profile becomes

$$u(y) = \frac{1}{\mu} \frac{dp}{dx} \left[\frac{y^2}{2} - hy - \frac{7\lambda^2}{20} \left[\left(\frac{1 + \frac{2y}{h} - \frac{h}{\lambda}}{\left(1 + \frac{y}{\lambda}\right)^2} \right) - 1 + \frac{h}{\lambda} \right] \right] - A_1 \left(\frac{2 - \sigma_U}{\sigma_U} \right) \frac{\lambda}{\mu} \tau_w. \quad (5.4)$$

The mass flowrate, \dot{m} , for incompressible Poiseuille flow at any Kn -value is given by the expression

$$\dot{m} = 2\rho \int_0^h u(y) dy, \quad (5.5)$$

where ρ is the gas density and is assumed to be constant and uniform. This expression remains valid for incompressible Poiseuille flows at any Kn as rarefaction effects are included directly in the velocity profile. In numerical simulations

²Strictly, when constitutive relations are scaled, the term ‘‘Navier-Stokes solution’’ becomes invalid, as the N-S-F equations refer only to the continuity, momentum and energy equations linked by linear constitutive relationships. As the intention of constitutive scaling is not to alter a fluid's properties, but merely to represent its behaviour when rarefied, the term Navier-Stokes will continue to be used in this thesis for clarity's sake when discussing constitutive scaling implemented in an N-S-F type framework.

where mass is conserved, any error in mass flowrate will be proportional to the error between the analytical and numerical velocity profiles.

5.2.1 Verifying numerical results

To test the implementations of Maxwell’s slip condition and constitutive scaling in OpenFOAM, results from numerical simulations are compared to the analytical expressions derived above. Poiseuille flow of the type shown in Fig. 5.1 is considered. Argon is taken to be the working fluid, at a constant temperature of $300K$, and gas properties are determined using [75]. The mean free path of the gas, λ , is calculated using Eq. (2.2), and the Knudsen number is determined using the channel height as the characteristic length scale:

$$Kn = \frac{\lambda}{2h}. \quad (5.6)$$

The channel height, length and the applied pressure gradient dp/dx along the channel are varied to alter the Kn of the system. Cases at four Kn values are considered. The system configurations for each of these variations are shown in Table 5.1. These cases are used to analyse the performance of the modifications to OpenFOAM as Kn moves from the continuum ($Kn < 0.001$), to the slip flow ($0.001 < Kn < 0.1$), to the transition regime ($0.1 < Kn < 1$). Pressure gradients for these verification cases have been chosen arbitrarily to minimise numerical solution time, as density is assumed to be constant throughout in both analytical and numerical simulations. It is worth noting, however, that for atmospheric outlet conditions these pressure gradients would induce large density changes, and that for purposes other than verification of the numerical solvers, a compressible simulation should be used.

First, it is important to verify that the performance of the original OpenFOAM Navier-Stokes solver has not been compromised by any of the modifications described in Chapter 4. To achieve this, a continuum- Kn Poiseuille flow at $Kn = 0.00035$ is assessed, whose details are given in the first column of Table 5.1.

Kn	0.00035	0.0035	0.035	0.35
$-dp/dx$	1×10^5	1×10^7	1×10^9	1×10^{11}
h	1×10^{-4}	1×10^{-5}	1×10^{-6}	1×10^{-7}
x	1×10^{-2}	1×10^{-3}	1×10^{-4}	1×10^{-5}

Table 5.1: Variation of channel height, length and applied pressure gradient for Poiseuille flow verification cases. Channel dimensions are given in m , and the pressure gradient is specified in N/m^3 .

Constitutive scaling is not applied, and the no-slip boundary condition is used. Figure 5.2 shows half-channel results from the OpenFOAM solver `microIcoFoam` compared to the analytical expression for the velocity profile given by Eq. (5.2).

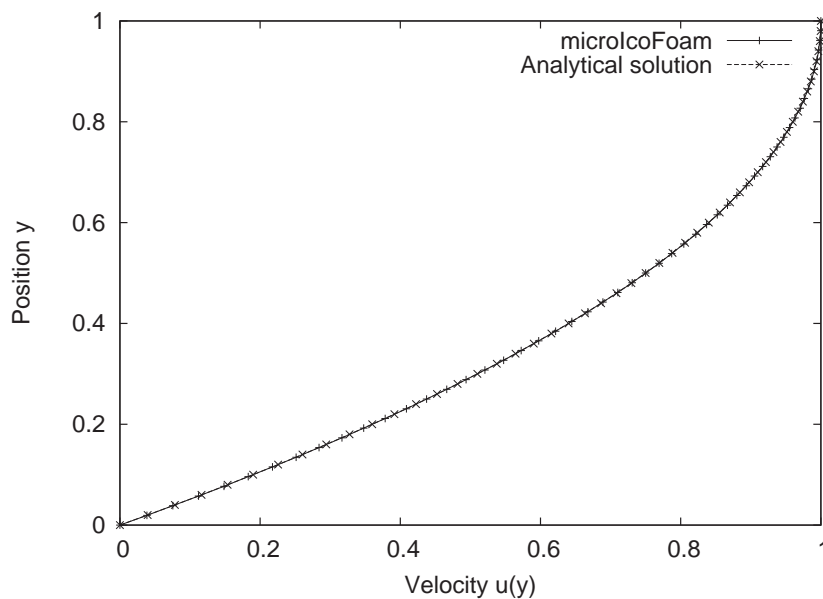


Figure 5.2: Analytical and numerical (`microIcoFoam`) Navier-Stokes solutions for no-slip Poiseuille flow at any Kn (standard no-slip Navier-Stokes solutions do not change with increasing Kn .)

The velocity profiles are non-dimensionalised by the channel-centre velocity, and the y -position across the channel is non-dimensionalised by the half-channel height, h . In all cases 2D structured-hexahedral meshes are used (100×40 cells), which have been refined until grid-independence is ensured, and simulations have

minimum convergence criteria of 1×10^{-6} . The maximum recorded error between the analytical solution and the microIcoFoam results for this case is 0.031%. The peak velocity corresponds to a Mach number of $Ma = 0.067$ in the channel, which is well within the incompressible limit of $Ma \leq 0.3$. The agreement of the analytical and numerical results in Fig. 5.2 verifies that the standard Navier-Stokes components of microIcoFoam operate as per their original implementation in OpenFOAM.

Figure 5.3 compares results from microIcoFoam with slip boundaries to those obtained from Eq. (5.3) for a Poiseuille flow where $Kn = 0.0035$, which represents the lower slip-flow regime. Here, the ability of the OpenFOAM implementation of Maxwell's slip condition to determine the gas velocity at the channel walls is tested.

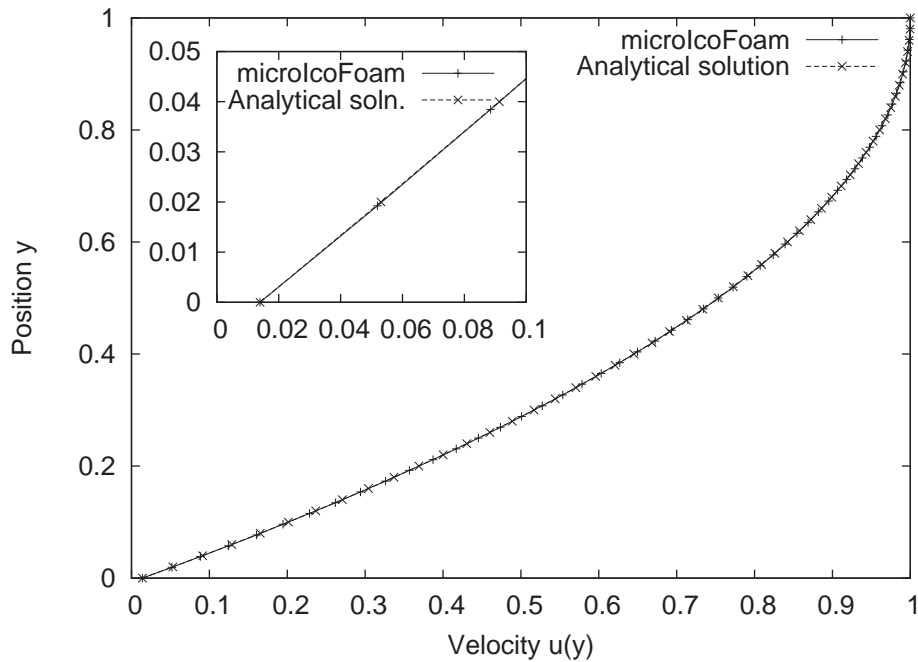


Figure 5.3: OpenFOAM results including Maxwell slip compared to analytical results from Eq. (5.3) for Poiseuille flow at $Kn = 0.0035$. Inset: a close-up of the near-wall region highlighting the agreement between the two profiles for slip at the channel wall.

As the inset to Fig. 5.3 shows, the microIcoFoam and analytical results agree

very closely. Interestingly, whilst the OpenFOAM implementation of Maxwell’s slip condition replicates the analytical solution almost exactly, such accuracy is not possible with the implementation of Maxwell’s slip equation found in Fluent 6.3, the latest release of the most widely used commercial CFD software [76]. A full explanation of the issues with Fluent, which were submitted to the company as a bug report, is given in appendix B.

Figure 5.4 expands on Fig. 5.3, verifying that the agreement between analytical and numerical results for Poiseuille flow is maintained across a range of different Knudsen numbers in the slip and transition regimes. The errors between Eq. (5.3) and the OpenFOAM simulation are again approximately 0.031% across the channel. This value is acceptably small and remains almost perfectly constant for both no-slip and Maxwell slip cases as Kn increases. The most likely source of this small error is truncation in the calculation of the analytical results.

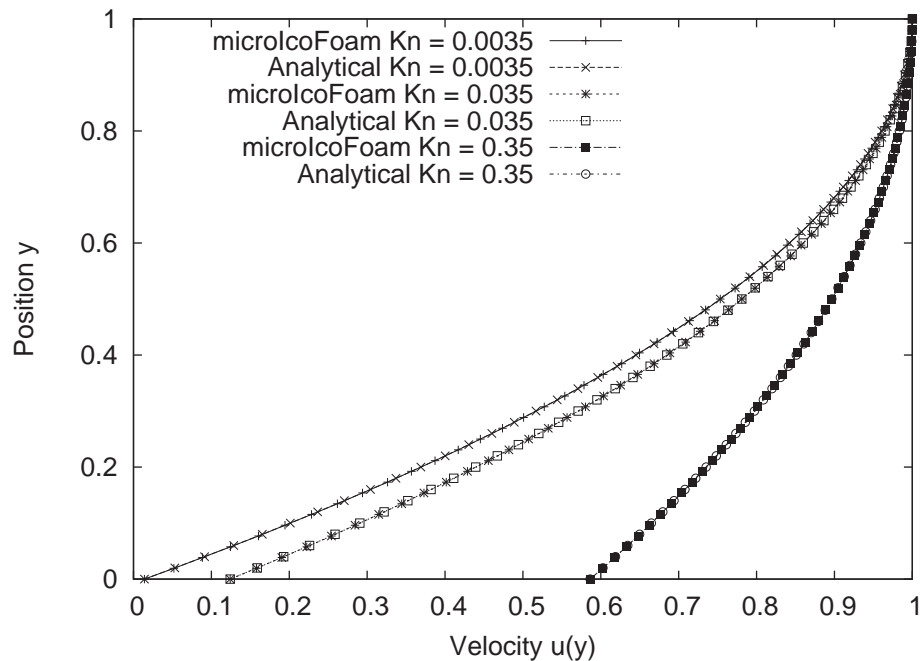


Figure 5.4: Verification of agreement between OpenFOAM simulations with Maxwell’s slip boundary condition and Eq. (5.3) at various Kn values.

As Kn increases beyond the midpoint of the slip flow regime it becomes

necessary to represent the impact of rarefaction on the velocity profile of gas flows [49, 77]. Figure 5.5 compares results from `microIcoFoam` to those obtained from the analytical solution for constitutive scaling, Eq. (5.4), for a Poiseuille flow case where $Kn = 0.035$. As the figure shows, numerically implemented constitutive scaling does not agree quite as closely with its analytical solution as the Maxwell slip or no-slip results. As Fig. 5.6 shows, when Kn increases the error diminishes, and it is within 0.1% by the onset of the transition regime, but this is larger than in the unscaled models. The numerical discrepancy is greater here as the scaling function used is both relatively steep and dependent on the normal distance to the nearest wall [12]. The velocity gradient in each cell is scaled as a function of this wall-distance, and hence the smaller the cells in the near wall region, the more accurate the scaling will be compared to the “ideal” analytical profile for the function. To ensure acceptable limits of error without increasing simulation time, the computational mesh can be graded towards the channel walls rather than refined as a whole. Even with this type of constraint on the simulation, however, `OpenFOAM` simulations with slip and constitutive scaling tend to converge faster than no-slip Navier-Stokes equivalents (and at approximately the same speed as slip solutions), as the maximum and minimum velocities in the simulation are generally closer together.

To illustrate the impact of constitutive scaling compared to Navier-Stokes solutions with Maxwell’s slip boundary condition, Fig. 5.7 shows `microIcoFoam` results from both models side by side. The difference in predicted slip at the channel wall is clearly apparent in the profiles shown for $Kn = 0.035$, and the changes to the shape of the velocity profile are pronounced in the transition- Kn results at $Kn = 0.35$. This transitional- Kn value reaches, or possibly even exceeds, the original proposed limits of applicability of the constitutive scaling method, but illustrates neatly how scaled Navier-Stokes solutions differ from standard slip-boundary solutions.

In this section, `microIcoFoam` has been successfully verified in that its imple-

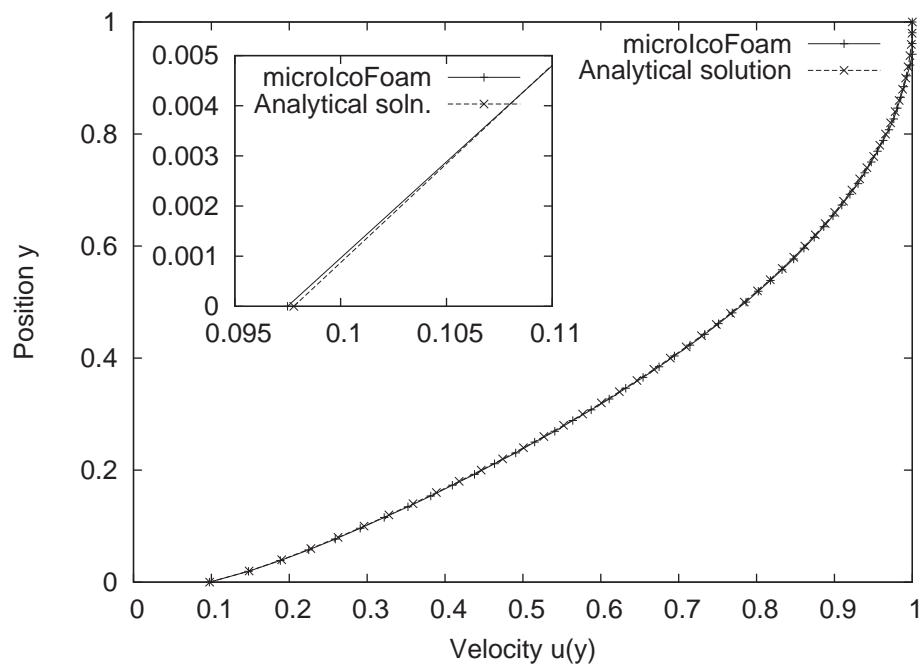


Figure 5.5: OpenFOAM results including constitutive scaling compared to analytical results from Eq. (5.4) for Poiseuille flow at $Kn = 0.035$. Inset: a close-up of the near-wall region highlighting the agreement between the two profiles at the channel wall.

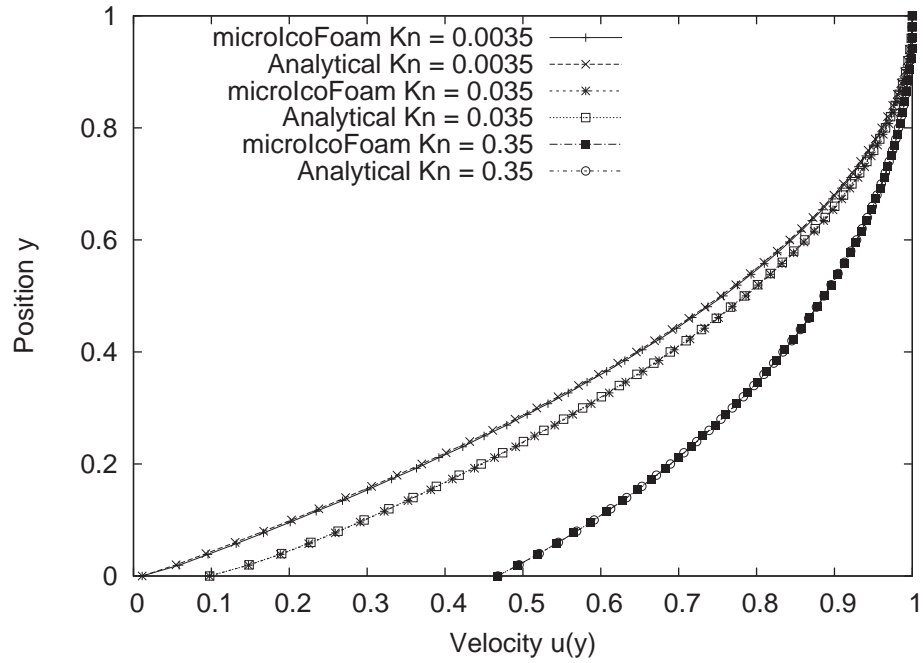


Figure 5.6: Verification of agreement between OpenFOAM simulations with constitutive scaling and Eq. (5.4) at various Kn values.

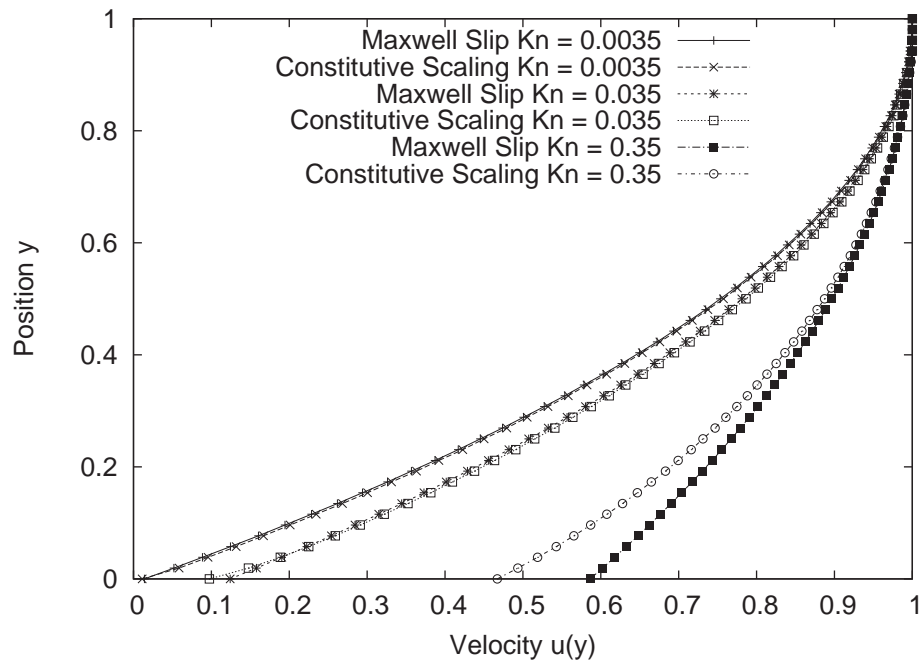


Figure 5.7: Poiseuille flow results: comparison of OpenFOAM using Maxwell's slip boundary condition with OpenFOAM using constitutive scaling.

mentations of the original mathematical models for slip and constitutive scaling have been shown to be suitably accurate for Poiseuille-type flows. The next stages in the development process are the verification of the solver for other flow types and the validation of the solver — testing the accuracy of the results against reliable external data that represent the true behaviour of microflows.

5.3 Couette flow

Couette flow is driven by shear-forces arising in viscous fluids, for example, the relative motion of two parallel plates produces a velocity profile in a fluid between them. Shear-driven flows in other configurations, such as between concentric rotating cylinders, are also commonly referred to as Couette flows. Planar Couette flow, like Poiseuille flow, can be considered in simple 1D form, making the case ideal for verification analyses. A schematic of a planar Couette flow is given in Fig.5.8.

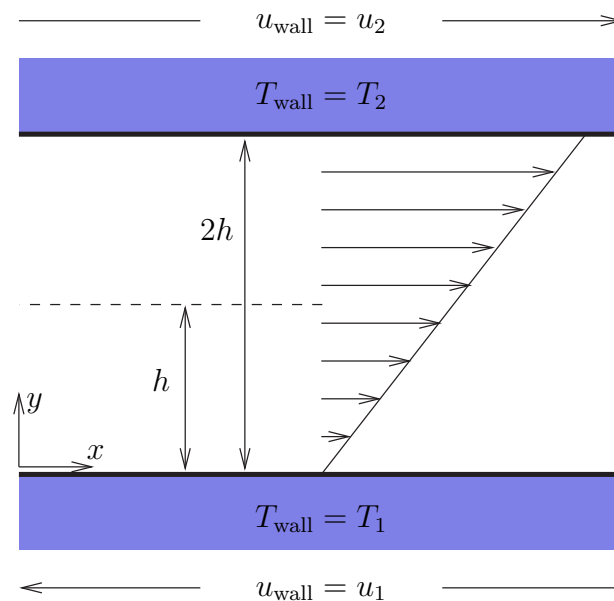


Figure 5.8: Schematic of Couette flow configuration with velocity profile.

The channel height is equal to $2h$, and this value can be varied to change the Knudsen number of the flow. Energy-transfer considerations are not included at

this stage, but the plate wall-temperatures T_1 and T_2 are considered to be equal and constant to allow the properties of the gas flow to be determined. Two forms of planar Couette flow are common. In the first type, one bounding plate remains stationary and the other moves. In the second type, the upper and lower plates move in opposite directions, most commonly with equal velocities, although any relative motion could be considered. In Fig. 5.8 and in the cases used here for verification, the second Couette-flow type is considered, where the plate walls move in opposite directions aligned with the x -axis at equal velocities.

In non-rarefied flows, the velocity profile produced by a constant applied shear stress is constant in the direction of motion of the plates, and varies linearly across the channel in the y -direction, as shown in Fig 5.8, allowing Couette flow to be considered alongside Poiseuille flow as a special 1D case. The Navier-Stokes expression for Couette flow is obtained by reducing Eqs. (2.5) and (2.6) to

$$\mu \frac{d^2 u}{dy^2} = 0. \quad (5.7)$$

When the no-slip condition is imposed at the lower wall, the gas velocity at the wall $u(y) = u_1$ at $y = 0$. In planar Couette flows where the condition $u_1 = -u_2$ is imposed, i.e. the wall velocities are equal and opposite, the gas velocity must be zero in the centre of the channel, giving the second boundary condition: $u(y) = 0$ at $y = h$. These boundary conditions can be applied to Eq. (5.7) to find a velocity profile for non-rarefied planar Couette flow³:

$$u(y) = u_1 \left(\frac{y}{h} - 1 \right). \quad (5.8)$$

As Kn increases and slip boundary conditions are applied, the magnitude of the slip at the channel walls will influence the velocity gradient. Maxwell's expression for velocity slip (Eq. (3.8)), however, is dependent on the velocity gradient at the wall. This circular reference is not hugely problematic, as the slip velocity magnitude can be obtained either using iterative methods, such as those

³Full details of all analytical solutions for Couette flow are given in appendix C

described in appendix D, or using the value of the shear stress at the wall, if it is known directly. For convenience, analytical solutions for Couette flow with slip will be presented in this thesis in terms of the slip velocity at the channel walls, u_{slip} , on the assumption that its value may be determined by independent means.

When slip is included at the channel walls, the boundary condition $u(y) = u_1 + u_{\text{slip}} = -u_2 + u_{\text{slip}}$ is applied at $y = 0$. The velocity still changes sign at the channel centre, so the condition $u(y) = 0$ at $y = h$ remains valid. The slip solution for planar Couette flow is given by

$$u(y) = u_2 \left(\frac{y}{h} - 1 \right) - u_{\text{slip}} \left(\frac{y}{h} - 1 \right). \quad (5.9)$$

When constitutive scaling is applied, Couette flow can no-longer be analysed using the conventional Navier-Stokes expression for a Newtonian fluid, but must be assessed using the more general expression

$$\frac{d}{dy} \left(\mu(y) \frac{du}{dy} \right) = 0, \quad (5.10)$$

where the viscosity $\mu(y)$ is treated as a function of normal distance away from the nearest wall, y . Note that care must be taken to ensure that y is measured from the nearest wall, i.e. that in the upper half of the channel the reference wall-distance is switched appropriately. For the constitutive scaling model proposed in [12], given by Eq. (4.6), the velocity profile for Couette flow with scaled constitutive relations is given by

$$u(y) = \frac{(u_2 - u_{\text{slip}}) \left(\frac{-20y}{7\lambda} + (1 + y/\lambda)^{-2} - 1 \right)}{\frac{-20h}{7\lambda} + (1 + h/\lambda)^{-2} - 1} - u_2 + u_{\text{slip}} \quad (5.11)$$

This expression is obviously cumbersome in comparison with the standard Navier-Stokes result, however, constitutive scaling is primarily intended as an aid to numerical analysis of rarefied gas flows, rather than for use in deriving analytical solutions. As described in Chapter 4, the introduction of constitutive scaling in OpenFOAM's numerical framework does not significantly complicate simulations, and in some cases is even observed to decrease average solution time.

5.3.1 Verifying numerical results

To verify the performance of the OpenFOAM implementations of Maxwell slip and constitutive scaling for Couette-type flows, results from CFD simulations are compared to Eqs. (5.9) and (5.11). Four 2D channel configurations, described in table 5.2, are used. The Knudsen number is defined using the full channel height: $Kn = \lambda(2h)^{-1}$.

Kn	0.00035	0.0035	0.035	0.35
u_1	-2.5	-2.5	-2.5	-2.5
u_2	2.5	2.5	2.5	2.5
h	1×10^{-4}	1×10^{-5}	1×10^{-6}	1×10^{-7}
x	1×10^{-2}	1×10^{-3}	1×10^{-4}	1×10^{-5}

Table 5.2: Variation of channel height, length and wall velocities for Couette flow verification cases. Channel dimensions are given in m and wall velocities are given in m/s .

The working fluid is argon at $300K$, with properties determined from data available in [75]. The flows are driven by a difference in velocity between the channel walls of $5m/s$, which corresponds to an incompressible Mach number of $Ma = 0.008$. The cases are analysed using grids of 100×40 cells. When constitutive scaling is applied the cell density is increased towards the walls at a ratio of 4:1, which ensures that the near-wall velocity gradients imposed by constitutive scaling are captured accurately. Grid independence is achieved in all test cases, and the minimum convergence limit for the simulations is specified as 1×10^{-6} . In all of the figures shown, the y -position across the channel is non-dimensionalised by the channel height $2h$, and the velocity $u(y)$ by the wall velocities, which are $\pm 2.5m/s$.

Figure 5.9 shows velocity profiles obtained using the microIcoFoam solver in OpenFOAM compared to results from Eq. (5.9). The results shown are for the upper half of the 2D channel, and are Navier-Stokes solutions with Maxwell's slip

condition applied. As the figure shows, perfect agreement in the cross-channel velocity profiles is obtained between the analytical and numerical solutions.

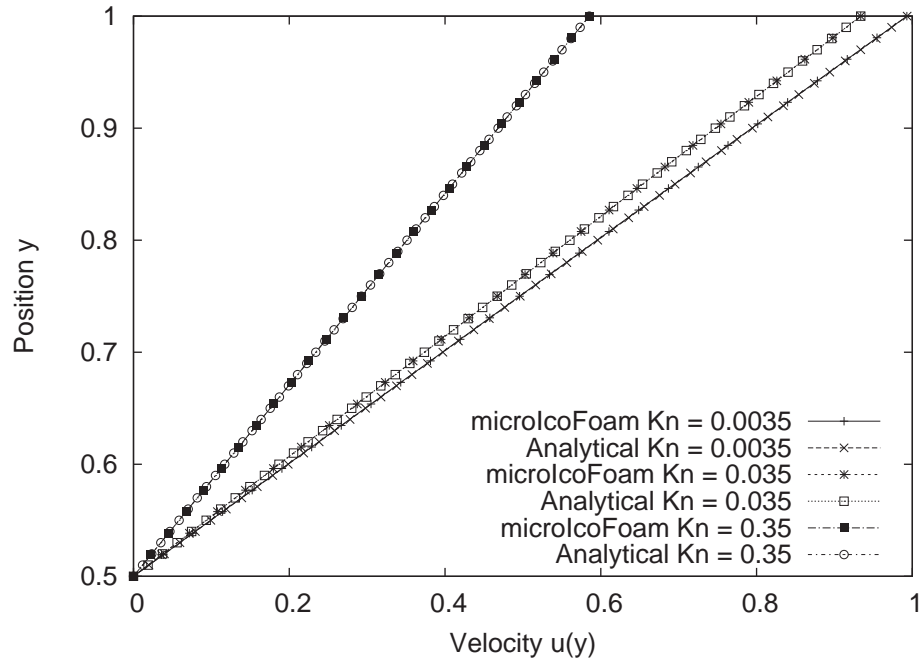


Figure 5.9: Verification of agreement between OpenFOAM simulations with Maxwell’s slip boundary condition and Eq. (5.9) at various Kn values.

The magnitude of the velocity slip at the wall in the analytical solutions was determined in two ways. At first, for simplicity, the velocity reported by the slip condition in OpenFOAM was used to represent u_{slip} in the analytical solutions, and perfect agreement between the two groups of solutions was obtained for each Kn -value. Then, to check the accuracy of the solutions in a fully independent fashion, the gas-slip values were obtained using iterative numerical solutions as described in appendix D. Again, absolute agreement (error $\sim 1 \times 10^{-16}$) between the combined analytical/numerical and fully numerical results from OpenFOAM was found.

Figure 5.10 shows the verification of the OpenFOAM implementation of constitutive scaling with the analytical expression Eq. (5.11) at varying Kn values. The agreement between the two groups of profiles is generally excellent, although

at the lowest Knudsen numbers the CFD results show very slightly exaggerated constitutive scaling. This error is extremely small, however, and is only apparent in the lowest Kn case, which falls into the lower slip-flow regime where the Navier-Stokes equations with slip boundary conditions remain valid.

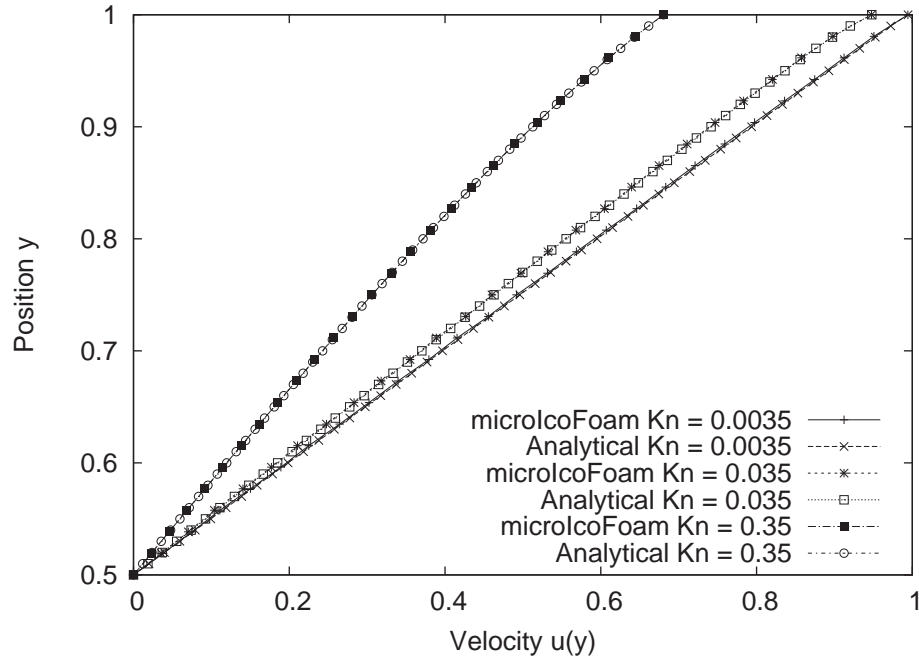


Figure 5.10: Verification of agreement between OpenFOAM simulations with constitutive scaling and Eq. (5.11) at various Kn values.

In Fig. 5.11, OpenFOAM results for both the Navier-Stokes equations with Maxwell’s slip boundary condition, and the scaled Navier-Stokes equations are shown. The upper figure shows results across the full height of the channel, with the top of the graph corresponding to $y = 2h$ and the bottom of the graph corresponding to the lower wall at $y = 0$. The lower figure shows a close-up of the velocity profile in the upper half of the channel only ($h < y < 2h$) to highlight the impact of constitutive scaling in the near-wall region. As the figures show, the microslip associated with constitutive scaling is lower than that predicted by Maxwell’s original slip condition, and the velocity gradient of the scaled results approaching the channel wall is steeper than that predicted by the Navier-Stokes

equations.

The results presented so far in this chapter verify that the slip and constitutive scaling models implemented in OpenFOAM are functioning as intended, however, they do not speak for the efficacy of the constitutive scaling model as a representation of rarefaction effects in gas microflows. To test the extent of the improved functionality that microIcoFoam offers over standard Navier-Stokes solvers for rarefied flows, validation exercises must also be carried out.

5.3.2 Validating numerical results

As an initial validation exercise, constitutive scaling results from OpenFOAM are compared to published DSMC data for low-speed Couette flows [77]. Planar Couette flows in channels are analysed in the paper, with the DSMC results being obtained using a modified form of a 1D code originally published in [27]. The maximum scatter in the available DSMC data for velocity profiles is reported as 1% [77].

The flow configuration analysed is slightly different from that used in the verification cases above, in that the Couette flows in [77] have one stationary wall and one moving wall. It is the upper wall of the channel that is in motion, moving at $20m/s$ in the positive x -direction. The working fluid is argon, and fully diffuse accommodation is assumed at the channel walls, i.e. $\sigma_U = 1$ in Maxwell's slip model. The channel walls are held at $273K$, which corresponds to a maximum Mach number of 0.065 for the gas flow, and which is within the incompressible limit.

Couette flows are analysed at a range of Kn values, from 0.01 to 10 in the original paper. In this thesis, a maximum Kn value of 1 will be considered, as beyond this point it is invalid to apply continuum analysis of any kind. In [77], Kn values are altered by varying the density of the working fluid. In OpenFOAM, Kn can be varied most conveniently and consistently in the incompressible solver by altering the height of the channel whilst maintaining a constant density. Flow

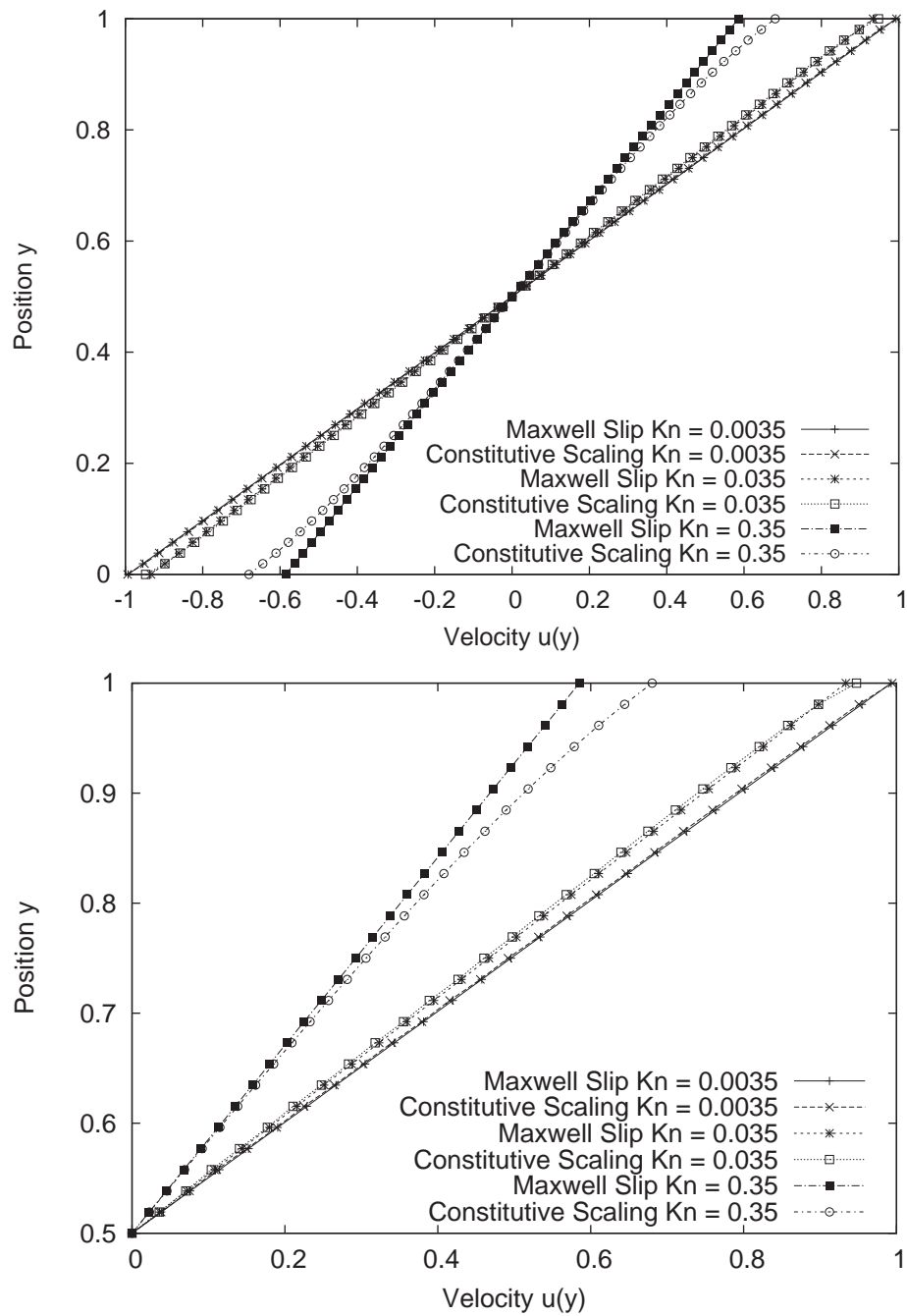


Figure 5.11: Comparison of OpenFOAM results for Couette flow with Maxwell's slip boundary condition with OpenFOAM results for constitutive scaling. The top figure shows the velocity across the whole channel, and the bottom figure the velocity in the upper half of the channel only.

properties for the CFD analysis are determined using [75].

In Fig. 5.12, results from the `microIcoFoam` solver are compared to the DSMC data presented in [77] for $Kn = 0.01, 0.1$ and 1 . Constitutive scaling results are seen to compare very favourably with the DSMC data. As Kn increases, both the magnitude of the velocity slip at the channel walls and the curvature of the velocity profile increase considerably. Results from the Navier-Stokes equations with constitutive scaling capture both of these trends well and, as Kn increases, offer significantly better performance than the Navier-Stokes equations with Maxwell's slip model alone. The largest errors between constitutive scaling and the DSMC results occur for $Kn = 1$, at a y -position of approximately 0.15 . This discrepancy seems to be due to a single anomalous data point in the DSMC, rather than any failing of the `OpenFOAM` model. This conclusion is supported by the fact that this data point does not appear to continue the DSMC profile smoothly, when compared to its neighbours, and also that in the upper half of the channel, agreement between constitutive scaling and the DSMC data is excellent. Overall, these DSMC results provide very good validation of the constitutive scaling approach in its current form, as integrated into CFD.

5.4 Constricted channels

The next stage in the validation process for constitutive scaling in `OpenFOAM` is to test the solver using rarefied flows in more complex, 3D geometries. Here, two different types of constrictions in silicon micro-channels are investigated. The first case is an orifice constriction plate placed in a rectangular channel. Orifice plates are small constrictions used in channels or pipes to create a pressure drop, allowing the mass flowrate of the fluid across the device to be measured. The second case is a venturi constriction of the same minimum area as the orifice plate, again in a channel of rectangular cross-section. Venturi constrictions are convergent-divergent sections that are also commonly used to measure mass flowrate. These flow configurations are chosen to allow results from `OpenFOAM` to be compared

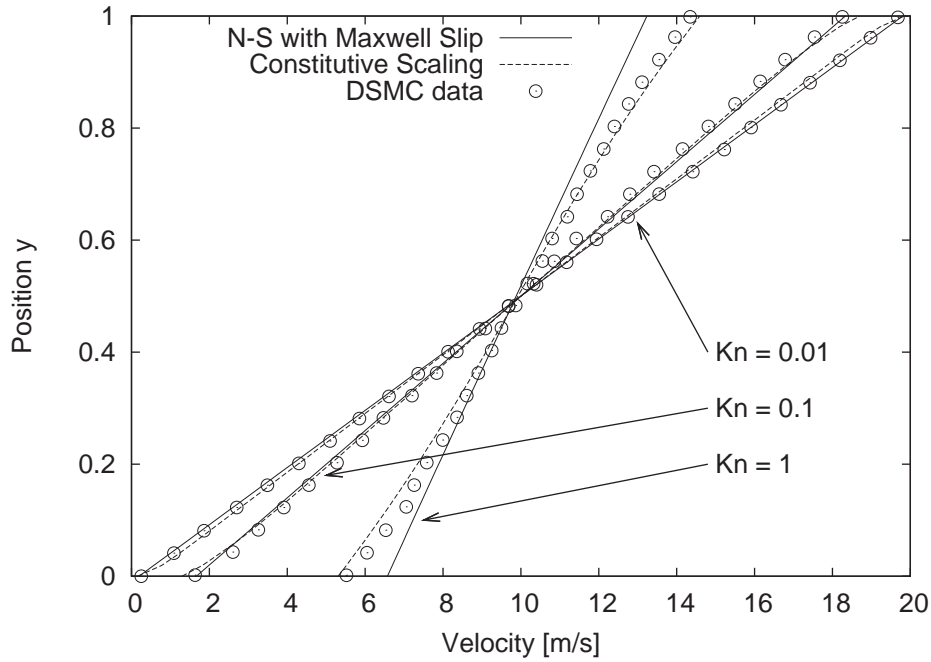


Figure 5.12: Constitutive scaling results from microIcoFoam compared to Navier-Stokes solutions with Maxwell’s slip condition and to DSMC results.

to available experimental data published by Li *et al.* [78].

The basic channel geometry and flow conditions are common to both cases. Schematic representations of the cases are given in Figs. 5.13 and 5.14. Experimental results are presented in [78] for a micro-channel with a height-to-width ratio of 40 : 1 (directions $y : z$). The channel has an end-to-end length, l , of $4000\mu m$ and a height, h , of $40\mu m$. It has a width of $1\mu m$ in the z -direction. Both constrictions are $10\mu m$ in height (h_c) on each side of the channel, leaving a $20\mu m$ throat height (h_t) through which fluid flows. The constriction depth d_c is also $10\mu m$, and the working fluid in this case is nitrogen at $314K$. The analysis is exclusively for incompressible flows, and the maximum pressure difference applied along the channel’s length is $140.3kPa$. All flows are taken to be isothermal.

Pressure changes along the channels of $99.63kPa$ and $140.3kPa$ ($14.45psi$ and $20.35psi$) are applied. Rarefaction in the system is characterised by the Kn value based on the smallest dimension of the system, its $1\mu m$ depth in the z -

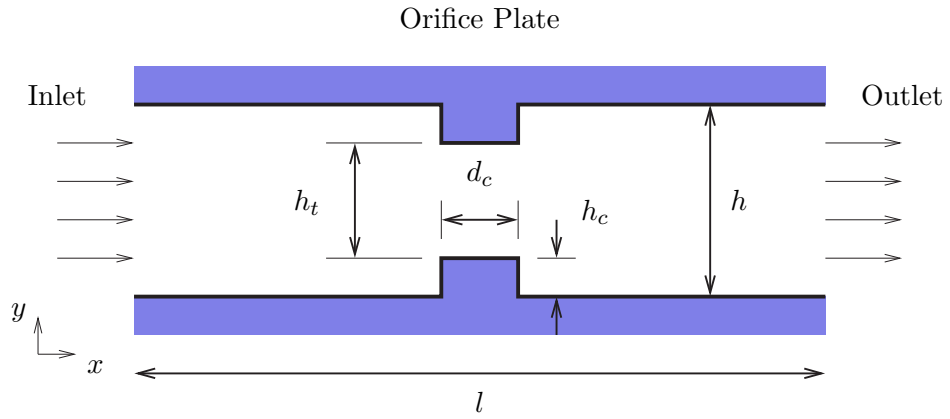


Figure 5.13: Microchannel orifice constriction geometry.

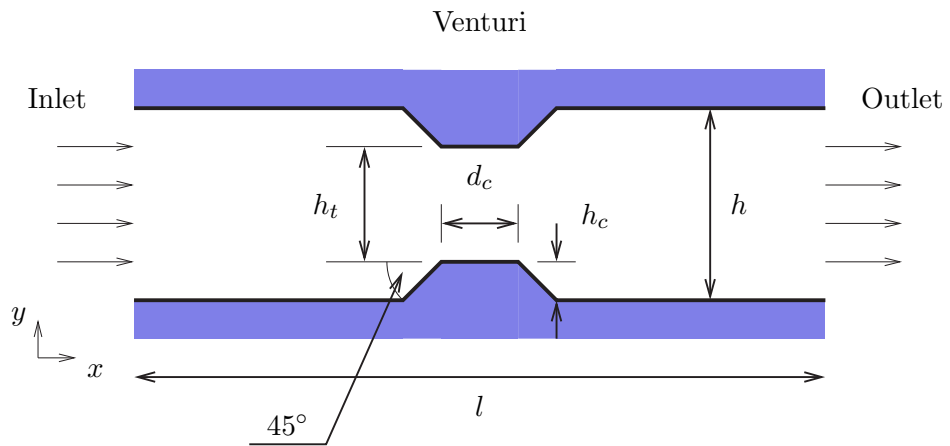


Figure 5.14: Microchannel venturi constriction geometry.

axis: $Kn = 0.06$. The tangential momentum accommodation coefficient in the velocity slip equation is taken to be $\sigma_U = 0.8$ throughout, which has been shown experimentally to be representative of gas-surface interactions between nitrogen and silicon [79].

For each applied pressure drop, three types of OpenFOAM simulation are carried out:

- No-slip analysis,
- Maxwell slip analysis,
- Constitutive-scaling analysis.

In the first instance, the no-slip boundary conditions applied in macroscale CFD are applied to the system walls. In the Maxwell slip case, Eq. (3.8) is applied as a velocity boundary condition with the first order slip coefficient $A_1 = 1$. The thermal creep is neglected as the cases are taken to be isothermal. When constitutive scaling is applied, the effective viscosity model proposed in [12], and given in Eq. (4.6), is used in conjunction with Maxwell's slip boundary condition, with microslip coefficient $A_1 = 0.8$.

5.4.1 Validating numerical results

Initially, OpenFOAM results for centreline pressure in the constricted channels are validated against the experimental data presented in [78]. Figure 5.15 shows results from microIcoFoam with constitutive scaling compared to experimental data for the orifice-plate constriction. The figure illustrates longitudinal pressure profiles for both applied pressure changes ($99.63kPa$ and $140.3kPa$). The experimental data, which are restricted to areas of the channel away from the constriction, have been extracted as lines from plots in [78]. Individual points are shown on the experimental data in this figure (and in other subsequent figures) to represent the ends of the available experimental data series, rather discrete

point values. In Figure 5.15, numerical results from OpenFOAM agree very well with the available data.

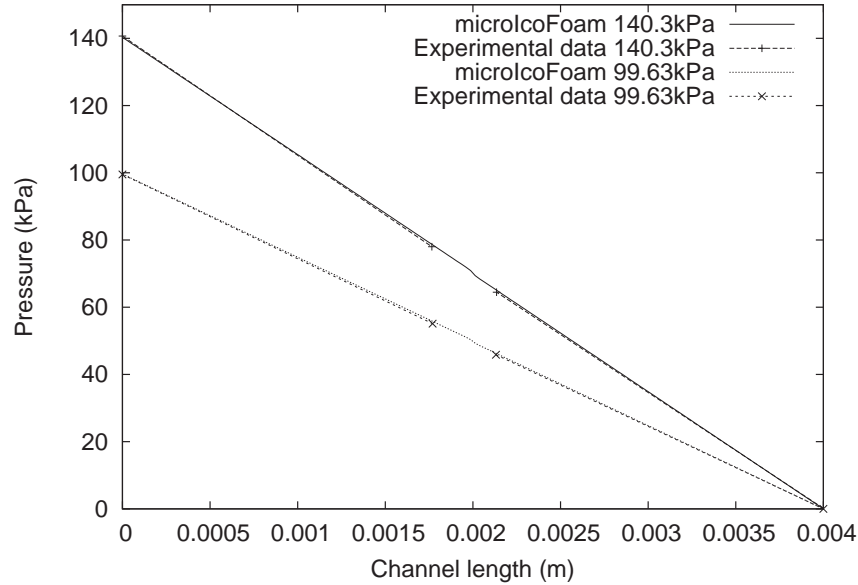


Figure 5.15: Centreline pressures in a channel with an orifice-plate constriction compared to experimental data.

For the venturi constriction case, Fig. 5.16 shows the centreline pressure profiles. In this case, the agreement between the numerical and experimental data is poor. The original paper, however, reveals that the experiments found venturi-type constrictions to produce a higher pressure drop in the flow than orifice plates of the same minimum area. The paper’s authors acknowledge that this data is likely to be erroneous, and comment on the role of one particular pressure transducer in producing these results [78]. Figure 5.17 shows centreline pressures in the region close to the venturi constriction for the 99.63kPa case. The experimental results given by Li *et al.* for the venturi constriction would seem to be consistent with a much smaller constriction throat height, and are almost certainly incorrect for the $20\mu\text{m}$ throat case.

In Fig. 5.18, numerical results for mass flowrate in both orifice- and venturi-constricted channels are compared to those given by Li *et al.* The experimental data, which are for test cases where maximum applied pressure changes peak

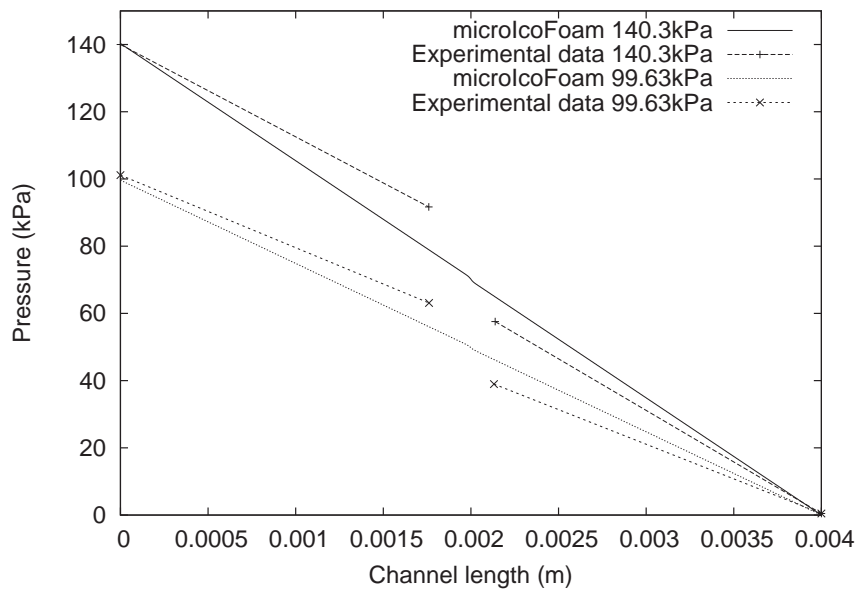


Figure 5.16: Centreline pressures in a channel with a venturi constriction compared to experimental data.

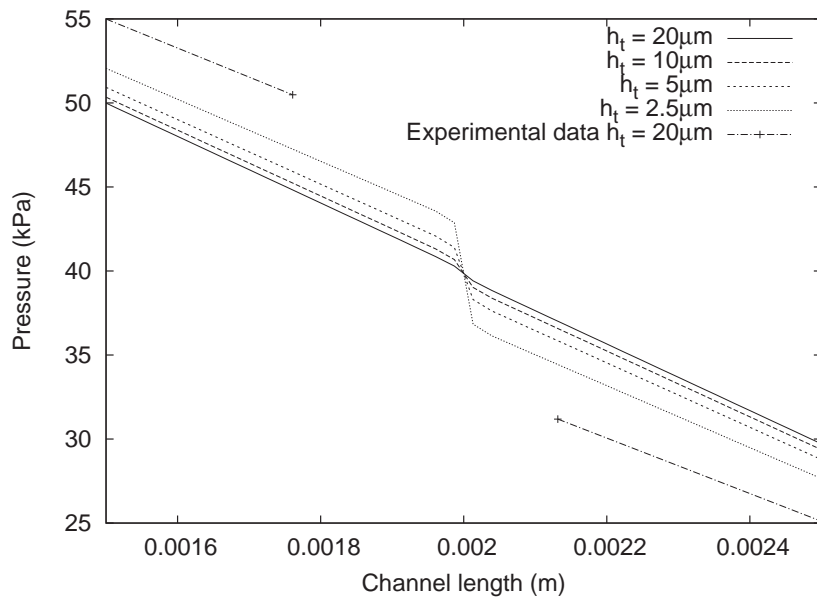


Figure 5.17: Centreline pressures in the near-constriction region through venturi constrictions in rectangular channels as throat height h_t decreases, compared to experimental data.

at 140.3kPa , are also compared to theoretical predictions of mass flowrate for an equivalent straight-channel. The theoretical value was calculated using the following expression [78, 80]:

$$Q_m = \frac{z^3 h P_o^2}{24 R T l \mu} \left(\left(\left(\frac{P_i}{P_o} \right)^2 - 1 \right) + 12 K n_o \left(\frac{P_i}{P_o} - 1 \right) \right), \quad (5.12)$$

as outlined in the original authors' paper, using a "best-fit" channel depth of $1.1\mu\text{m}$, and $K n_o = 0.06$ [78].

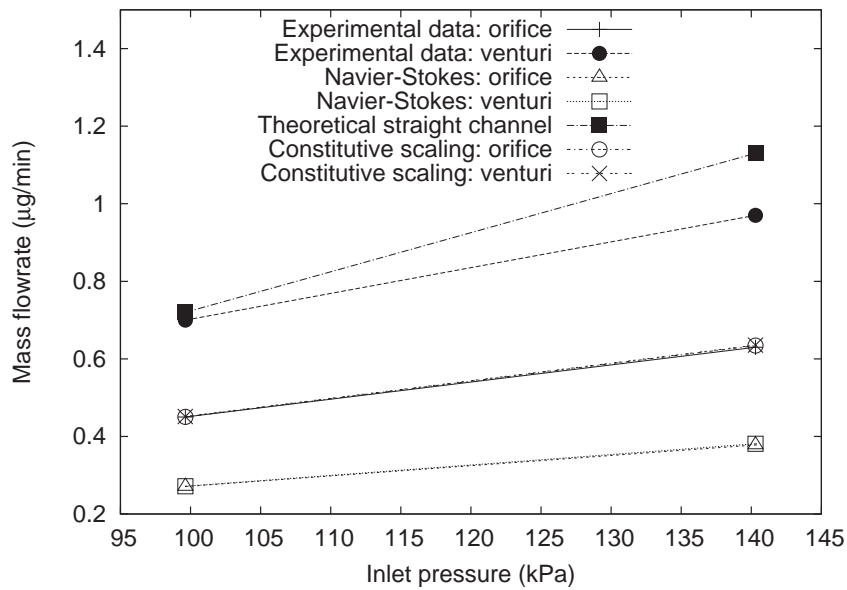


Figure 5.18: Mass flowrates through constricted microchannels: OpenFOAM results for constitutive scaling and Navier-Stokes equations compared to experimental results.

Numerical results from microIcoFoam for a $20\mu\text{m}$ orifice constriction are shown to agree almost exactly with the experimental data for orifice-plate mass-flow at both applied pressures. This agreement is possibly better than should be expected, as the applied pressure gradients along the experimental channels would typically produce large density changes. Density variations are not modelled using this incompressible solver, which is a potential source of inconsistency that has not yet been resolved.

The OpenFOAM results for mass flowrate through the venturi constrictions

do not agree with the experimental results from [78]. While the experimental results return higher flowrates through the venturi constriction, the numerical simulations return very similar mass flowrates for both the orifice and the venturi; between the two case types the agreement is to within 0.2%. Although the standard Navier-Stokes simulations under-predict the magnitude of the mass flowrate, they too predict very similar values between the orifice and venturi case types. These OpenFOAM results are reasonable, however, as the cases studied have very low Reynolds numbers: $Re \approx 0.7$ for the $99.63kPa$ pressure difference and $Re \approx 1$ for $140.3kPa$ pressure difference. In these fully developed laminar flows, no flow separation occurs at the trailing edge of the orifice plate. In fact, viscous work causes the orifice constriction to develop a velocity profile similar to that observed in the venturi constrictions. As Fig. 5.19 illustrates, regions of very low-speed or stationary flow can develop on the upstream and downstream edges of the orifice, effectively channelling the flow through a venturi shape. For a given throat geometry in slow gas-flows such as these, it is reasonable to assume that the mass flowrate through the two devices would be comparable, and that there is some error in the venturi constriction results presented in [78].

Figure 5.20 shows numerical results for x -direction throat-exit velocity at the throat wall for an orifice-plate constriction, contrasting results from the three types of numerical model tested for verification purposes. Whilst the no-slip case adopts the velocity of the stationary wall, the Maxwell slip and constitutive scaling cases capture a finite degree of slip at the boundary. The constitutive-scaling model with microslip profile predicts a slip velocity 20% lower than the Maxwell slip prediction, and displays a velocity gradient at the wall 1.7 times steeper than that of the Maxwellian profile, representing the impact of the Knudsen layer. The increase in the gradient matches the applied scaling function, implying reasonable grid independence has been achieved, and is consistent with the increase in strain-rate observed in other analyses of Knudsen layers [3, 8].

Each numerical case is simulated in 3D on a standard desktop PC, with no

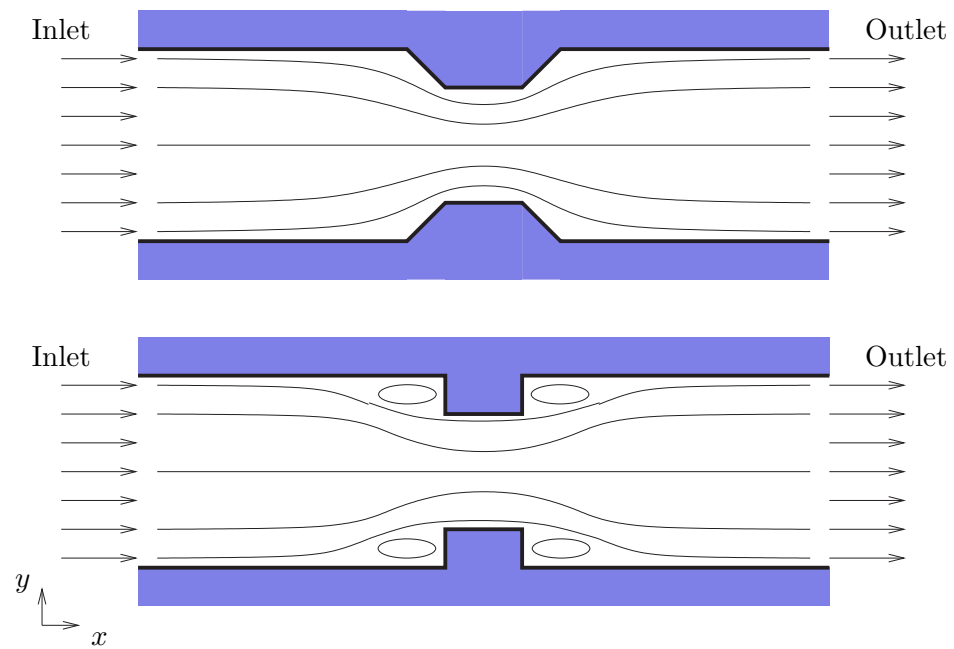


Figure 5.19: Schematic of low-speed viscous flow through venturi-type and orifice constrictions.

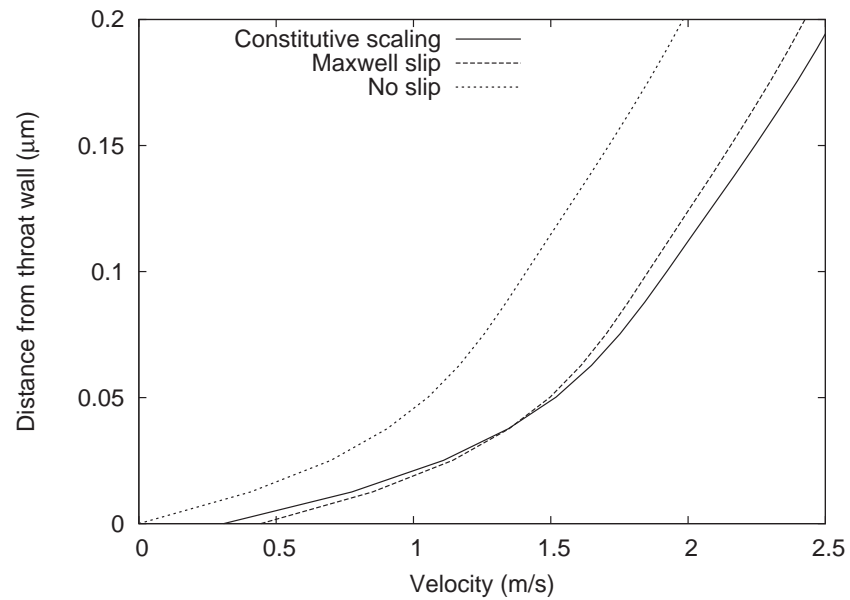


Figure 5.20: Velocity profiles close to the throat wall for an orifice-plate constriction. Standard no-slip Navier-Stokes results are compared to results with Maxwell's slip boundary condition applied and to constitutive scaling with microslip.

appreciable time difference introduced by the inclusion of constitutive scaling in the analysis. Structured, hexahedral meshes are used in all cases which were refined toward the channel walls in ratios of 4 : 1 (minimum of $160 \times 100 \times 50$ cells). Typical solution times for each case are of the order of 30–40 minutes. The efficiency of the OpenFOAM solver for these cases highlights the practicality of the constitutive scaling method in CFD. At such low Mach numbers ($\approx 1.4 \times 10^{-3}$) it would be incredibly computationally expensive to apply DSMC and satisfactorily reduce scatter in the results. Also, the difficulties encountered by Li *et al.* in ensuring the accuracy of experiments conducted at these physical scales reinforce the need for more reliable means of simulating gas microflows.

5.4.2 Extending the analysis

As the OpenFOAM simulation has been shown to replicate some features of Li *et al.*'s experimental results, a series of new test geometries are investigated to examine the behaviour of fluid flow through constrictions with reduced throat heights. As Knudsen number is directly related to the system geometry, a Kn value based on throat height would vary directly with changes to the constriction. By varying the width-based reference value of $Kn = 0.06$, which is otherwise independent of changes to geometry in the y -direction, by the factor of change in geometry, it is possible to include the effects of varying constriction height on rarefaction. Table 5.3 shows the variation of Kn with throat height, h_t .

Throat heights in the channel for both orifice and venturi constrictions are decreased for the lowest pressure drop, $99.63kPa$, to a minimum throat height of $2.5\mu m$. In the orifice plates, the $10\mu m$ constriction depth, shown as d_c in Fig. 5.13, is maintained while the throat height, h_t , is decreased. In the venturi constrictions both constriction depth, d_c , and the 45° angle are maintained as the throat height, h_t , is decreased.

Figure 5.21 illustrates the centreline pressure through a channel with a venturi constriction which has a $5\mu m$ throat height. As the constriction height increases

Kn	0.06	0.12	0.24	0.48
h_t	$20\mu m$	$10\mu m$	$5\mu m$	$2.5\mu m$

Table 5.3: Variation of Knudsen number with throat height for a pressure drop of $99.63kPa$ across the channel.

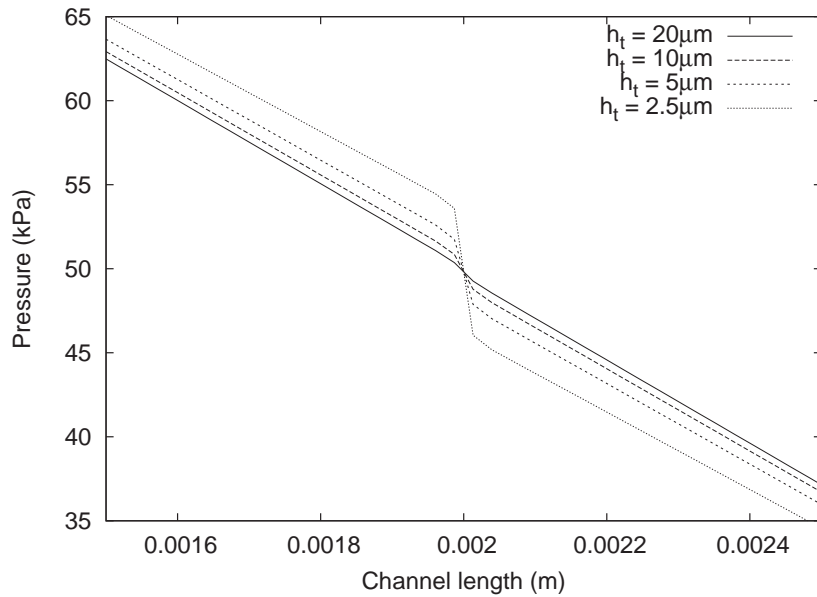


Figure 5.21: Centreline pressures in the near-constriction region through venturi constrictions in rectangular channels as throat height h_t decreases: constitutive scaling results only.

(and throat height decreases) the pressure drop across the venturi becomes increasingly sharp, when compared to Fig. 5.16 for example, as would be expected.

The effects of increasing gas rarefaction are also highlighted when throat heights in the channels are reduced. Fig. 5.22 shows the maximum velocity magnitude for a range of orifice-plate constrictions. Each constriction is analysed using both the no slip boundary condition and the constitutive scaling model with microslip boundaries. The figure shows the variation in maximum velocity predicted by each model as the throat height h_t is varied from $20\mu m$ to $10\mu m$, $5\mu m$ and $2.5\mu m$. The impact of the Knudsen layer is larger for smaller throat heights, as shown by the greater separation between the standard Navier-Stokes profile and the constitutive scaling profile.

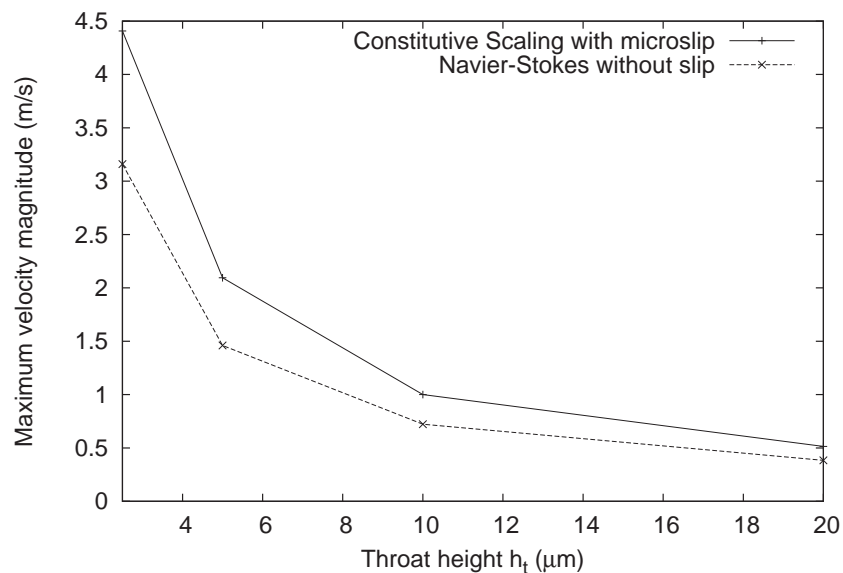


Figure 5.22: Maximum velocity magnitude for orifice-plate constrictions as throat height h_t varies.

With smaller throat heights, the Knudsen number is higher, and hence the Knudsen layer and velocity slip have a greater effect on the simulation. To illustrate, when the constriction height h_t is $20\mu m$ and $Kn = 0.06$, the no-slip model predicts zero-velocity at the wall, and a maximum velocity magnitude of $0.389m/s$. The constitutive scaling simulations return a slip velocity of

0.00761m/s at the channel walls, and a maximum velocity magnitude of 0.539m/s at the constriction centre. The difference between the predicted maximum velocities is 39%. When h_t is reduced to 2.5 μ m, and Kn increases to 0.48, the no-slip model gives a maximum velocity of 3.12m/s, compared to the constitutive scaling model's slip at the channel walls of 0.67m/s, and constriction-centre velocity of 4.5m/s. The difference between the maximum centreline velocities for the higher- Kn case is 44%, which represents a change in the discrepancy between no-slip and scaled simulations of 5% with a single order of magnitude change in Kn .

Using the experimental data published in [78], microIcoFoam has been shown to produce reasonable predictions of the behaviour of low-speed gas flow through constricted microchannels. As the available experimental data are somewhat limited, validation using alternate data sources would be desirable to ensure that the numerical solver provides an accurate representation of the fluid flow through microscale constrictions. In OpenFOAM, several higher- Kn cases beyond the scope of the original experimental data have also been studied. The application of constitutive scaling to these cases has shown that as gas rarefaction increases, the macroscopic behaviour of gas flow through constricted microchannels is likely to be significantly altered. This highlights that successful design of microscale mass flowrate measurement devices will be heavily dependent on the ability of engineering tools to capture the behaviour of rarefied gases.

5.5 Cylindrical Couette flow

Couette flow between rotating concentric cylinders, as shown in Fig. 5.23, is a shear-driven problem that behaves in a similar manner to planar Couette flow. This is an excellent case with which to test the microIcoFoam solver, as it assesses both the solver's ability to adequately capture slip and Knudsen layer effects in curved geometries, and its ability to capture some of the counter-intuitive features found in rarefied flows. This flow configuration is of particular engineer-

ing relevance as it corresponds directly to gas behaviour in microscale air bearings, which appear in many applications such as microscale power generation and micro-turbines, see e.g. [1].

Typically, in cylindrical Couette flow, the inner cylinder rotates at a constant velocity, whilst the outer cylinder remains stationary. The shear-force arising in a viscous fluid between the cylinders generates a velocity profile between them in a radial direction. Rotating Couette flow is quite an unusual case in that, for rarefied flows over surfaces where the gas-surface interaction is largely specular, a complete inversion of the velocity profile, compared to the standard Navier-Stokes results is possible [15]. That is to say, the degree of slip present can allow the flow to move more quickly over the stationary outer cylinder than over the rotating inner cylinder, which is entirely counter-intuitive. Rarefaction effects are the cause of this unusual phenomenon. The low momentum accommodation coefficient of specular flows implies that the momentum of molecules impinging the cylinders is largely reversed. Those molecules that have collided with the rotating cylinder will therefore retain most of their momentum. When the gap between the cylinders is sufficiently small, molecules reflected from the rotating inner cylinder will, on average, have their next intermolecular collisions close to the outer wall, causing the flow nearer the outer cylinder to be faster than the flow near the stationary wall.

Isothermal Couette flow between rotating cylinders is a case in which no reasonable solution may be obtained using the constitutive scaling technique unless the coupled velocity-viscosity terms described in Eq. (4.12) are retained in the momentum equations. In the case of a rotating inner cylinder and a stationary outer cylinder, direct simulation Monte Carlo (DSMC) molecular dynamics simulations predict an inverted tangential velocity profile for some rarefied flows, i.e. the gas velocity increases with radial distance from the moving cylinder [15]. This case has been investigated previously in order to compare results obtained using Eq. (3.7) in place of Eq. (3.6), however the constitutive-scaling approach has not

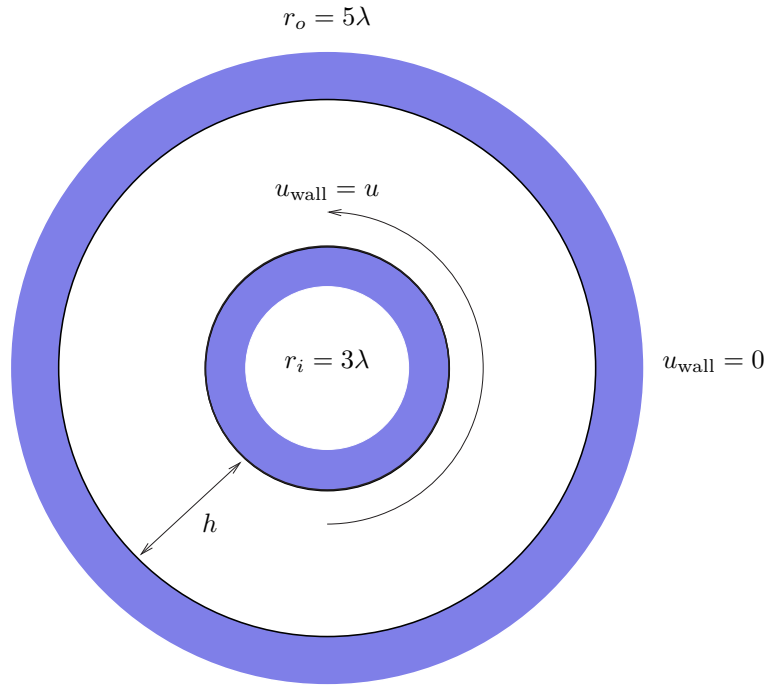


Figure 5.23: Schematic of Couette flow between concentric cylinders.

previously been applied to this problem [16, 20].

Figure 5.24 illustrates results for tangential velocity in the rotating Couette flow problem. The inner and outer cylinders are concentric, with respective radii of 3λ and 5λ , where λ is the mean free path of the gas flowing between the cylinders, which is argon at standard temperature and pressure [75]. The tangential momentum accommodation coefficient, $\sigma_U = 0.1$. The figure compares the velocity profile predictions of several numerical models with DSMC data. Both no-slip and conventional slip (Eq. (3.6)) simulations fail to predict inversion of the velocity profile. Maxwell's original slip equation, in this case Eq. (3.7), is seen to predict an inverted velocity profile, although it cannot capture the form of the DSMC results. When the constitutive-scaling method (shown as the solid line) is applied, not only is good general agreement with Maxwell's original slip condition observed, but the shape of the velocity profile is seen to approach that of the DSMC data. The slight dip in the profile near the inner wall and the reduction in gradient towards the outer cylinder can clearly be seen. Quantitative

agreement with the DSMC remains poor, but it should be noted that such high Knudsen number cases ($Kn = 0.5$), represent the very edge of applicability for even scaled continuum models, and close numerical agreement is not expected.

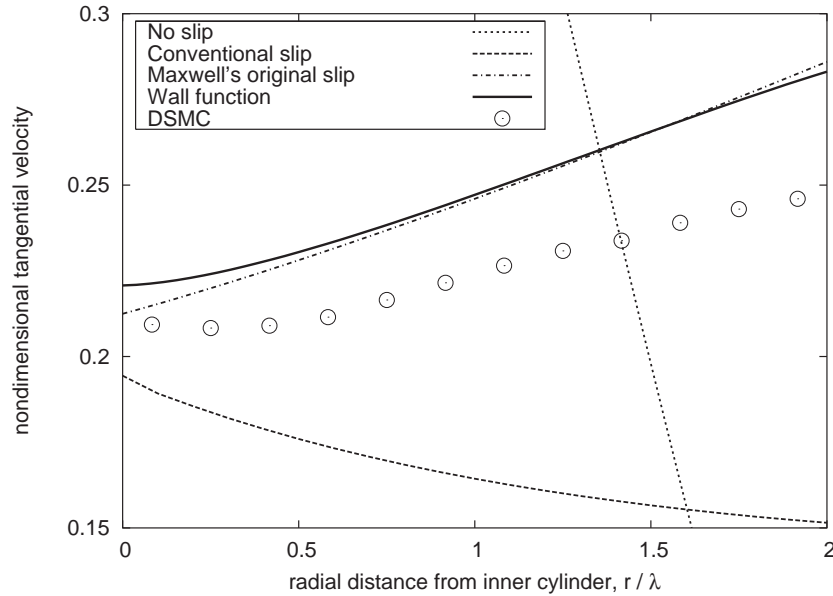


Figure 5.24: Velocity profiles in cylindrical Couette flow non-dimensionalised by the tangential velocity of the inner cylinder. Comparison of no slip ($\cdot\cdot\cdot$), conventional slip ($- -$), Maxwell’s original slip ($- \cdot -$), constitutive-scaling in CFD (—) and DSMC data (\circ).

5.6 Summary

In this chapter, verification analyses have been carried out comparing OpenFOAM results for Maxwell’s slip boundary condition and constitutive scaling to analytical solutions for planar Poiseuille and Couette flows. The numerical results were observed to match the analytical solutions closely, ensuring that the functions implemented in the code operate correctly. Validation analyses have also been conducted, comparing results from OpenFOAM to DSMC data and experimental data for flow in several different configurations. Overall, the results indicate that the constitutive scaling method is able to satisfactorily capture the key effects of gas rarefaction, slip and the Knudsen layer, for incompressible and

isothermal cases. The next stage in the development process of constitutive scaling in CFD is the extension of the method to fully compressible flows, and the inclusion of heat transfer effects.

Chapter 6

Compressible flows

6.1 Introduction

Gas microflows are often compressible, both in the traditional sense that it is possible for the local Mach number to be large, i.e. the flow is compressible, and also in the sense that large pressure and density gradients are commonly found in rarefied flows, i.e. the fluid is compressible. Both “types” of compressibility lead to coupling of the momentum and energy equations, as the ratio of a fluid’s kinetic energy to its internal energy becomes large. This ratio is represented by the Mach number, Ma , and when dealing with rarefaction in compressible flows, it is common to redefine Knudsen number as a function of the Mach number [81]:

$$Kn = \sqrt{\frac{\gamma\pi}{2}} \frac{Ma}{Re}. \quad (6.1)$$

This compressible definition of Kn is also a function of the specific heat ratio, γ , and the Reynolds number, Re , which is commonly low in microflows where viscous dissipation effects are enhanced by large surface-area to volume ratios. This increased degree of viscous dissipation can substantially alter the impact of compressibility on a fluid flow. For example, in some microsystems where flow approaches the local speed of sound, smooth regions of sonic flow develop, rather than discontinuous shock waves [82, 83]. Rarefaction effects can also be seen to counteract compressibility effects; the introduction of slip boundary conditions, for instance, reduces shear stress and hence viscous work at system bound-

aries [74].

In order to accurately model compressible rarefied flows, a CFD simulation must therefore solve both the energy and momentum equations in a coupled fashion and also incorporate rarefaction effects. For continuum models, both velocity slip and temperature jump boundary conditions must be included, in addition to models for Knudsen layers observed in both velocity and temperature fields. Constitutive scaling of the thermal Knudsen layer has been proposed previously, however, it has not to date been applied either to cases where both momentum and energy exchanges are present, nor has it been applied in a generalised CFD framework [36, 45].

In this chapter, an OpenFOAM solver suitable for compressible rarefied flows is described and the performance of two published constitutive scaling models implemented within it is analysed [12, 17]. Half-space problems are used to assess the implementation of the scaling models, which are compared to kinetic theory data for validation and then contrasted to each other [4, 6]. The scaling approach is then applied to an industrially relevant application, compressible micro-Couette flow, and OpenFOAM results are compared to available DSMC data [18]. This case study includes a detailed critical analysis of the constitutive scaling method, which focuses in particular on the relationship between momentum and energy transfer in constitutive scaling, and on the selection of appropriate boundary conditions for high- Kn compressible flows.

6.2 Compressible solvers in OpenFOAM

Several compressible flow solvers are available in the OpenFOAM software distribution, each tailored to a specific type of compressible flow [70]. The rhoSonicFoam solver has been selected as the most appropriate application to use as the basis for a compressible microflows solver, as it has been partially redeveloped for analysing rarefied flows in hypersonic-aerodynamics applications [13, 71, 84].

The rhoSonicFoam solver is a pressure-density-based application for lami-

nar compressible flows, and solves governing equations of continuity, momentum (posed in terms of mass-flux) and total energy. These equations are solved in a segregated manner, followed by a PISO-style pressure correction loop. For gas microflows, however, the solver requires substantial modification — primarily as the release version is inviscid. The governing equations implemented therefore do not contain diffusive terms, or sources of mechanical power and heat flux. The inviscid-flow assumption is valid for some high-speed compressible flows, but it is not appropriate for microscale flows, which are almost exclusively internal flows dominated by the effects of bounding surfaces. A viscous version of `rhoSonicFoam`, which also includes diffusive terms in the governing equations and is known as `rhoEsonicFoam`, has been produced as part of another non-equilibrium flow project undertaken at the University of Strathclyde [71, 84]. The `rhoEsonicFoam` solver also features boundary conditions more appropriate to non-equilibrium flows, including Maxwell’s velocity slip condition [10].

In the following sections, a summary of the differences between `rhoSonicFoam` and `rhoEsonicFoam` is given, alongside a general description of how the solvers operate. Then, further changes made as part of the work of this thesis to `rhoEsonicFoam` are described, before details of how the new code is used to implement constitutive scaling for compressible gas microflows are given.

6.2.1 Compressible solver: `rhoSonicFoam`

The compressible solver `rhoSonicFoam` released with OpenFOAM (in this case version 1.3) initially solves for density, ρ , using the continuity equation:

$$\frac{\partial \rho}{\partial t} + \nabla \cdot \mathbf{U}(\rho) = 0. \quad (6.2)$$

The inviscid momentum and energy equations in the solver are formulated implicitly and solved for mass flux $\rho\mathbf{U}$ and total energy ρE ;

$$\frac{\partial (\rho\mathbf{U})}{\partial t} + \nabla \cdot \mathbf{U}(\rho\mathbf{U}) = -\nabla p, \quad (6.3)$$

$$\frac{\partial(\rho E)}{\partial t} + \nabla \cdot \mathbf{U}(\rho E) = -\nabla \cdot \mathbf{U}p. \quad (6.4)$$

The temperature field is then extracted from the solution to this form of the energy equation using the definition of total energy [85]:

$$\rho E = \rho c_v T + \frac{(|\rho \mathbf{U}|)^2}{2\rho}, \quad (6.5)$$

$$\therefore T = \frac{\rho E - \frac{1}{2\rho}(|\rho \mathbf{U}|)^2}{\rho c_v}. \quad (6.6)$$

The perfect gas law is given by

$$p = \rho RT, \quad (6.7)$$

where R is the gas constant, and this expression is used to determine a pressure field from the continuity equation prediction for density. The perfect gas law is a statistical description of microscopic behaviour which represents the macroscopic behaviour of gases. Although a statistical average taken only in the non-equilibrium Knudsen layer could theoretically differ from the ideal gas approximation, where flow properties in slip- and transitional- Kn flows are averaged over full systems, the perfect gas law should remain valid.

Next, momentum fluxes on cell-face areas are calculated, and a pressure equation combining the continuity equation and the perfect gas law is formulated in terms of pressure and the momentum fluxes. The solution to this pressure equation is used as a corrector for the continuity equation. The momentum equation is also corrected, based on the momentum fluxes used in the pressure equation. When reasonable convergence for pressure and momentum flux is obtained iteratively, the velocity field is determined by dividing the momentum-equation solution for mass flux $\rho \mathbf{U}$ by the continuity equation solution for density ρ . Thus, by solving implicitly for p , $\rho \mathbf{U}$ and ρE , solutions for ρ , \mathbf{U} and T are obtained.

Boundary conditions are applied to individual analyses following OpenFOAM's standard case structure, and specified in terms of p , \mathbf{U} and T . These conditions

are then interpreted by the code as boundary conditions for the equations posed in terms of ρ , $\rho\mathbf{U}$ and ρE . Velocity slip and temperature jump conditions are not implemented in the `rhopSonicFoam` release.

6.2.2 Modified solver: `rhopEsonicFoam`

Redevelopment of the `rhopSonicFoam` solver by C.J. Greenshields undertaken as a part of [71] has transformed the publicly released code into a new solver, `rhopEsonicFoam`. The primary difference between `rhopSonicFoam` and `rhopEsonicFoam` lies in the formulation of the governing equations, where `rhopEsonicFoam` includes viscous terms. The new solver also includes more refined mapping of boundary conditions between standard macroscopic quantities and the solution variables, and a wider range of boundary conditions, including Maxwell's velocity slip condition, has been implemented [10, 11]. A choice of three viscosity models is also available in `rhopEsonicFoam`: Sutherland's law, the power law and the standard Newtonian fluid model [70].

The basic solution procedure used in `rhopEsonicFoam` follows that outlined above for `rhopSonicFoam`, and the solvers use identical continuity equations. The momentum and energy equations, however, are implemented in viscous form. The momentum equation in `rhopEsonicFoam` is

$$\frac{\partial(\rho\mathbf{U})}{\partial t} + \nabla \cdot \mathbf{U}(\rho\mathbf{U}) - \nabla \cdot \boldsymbol{\tau} = -\nabla p, \quad (6.8)$$

where the divergence of the shear stress, $\nabla \cdot \boldsymbol{\tau}$, is a diffusive term. Typically, the Newtonian shear-stress tensor, given by Eq. (4.11), is formulated explicitly in terms of velocity.

In order to introduce the normally explicit shear stress term into the implicit form of the momentum equation, an equivalent expression in terms of mass flux $\rho\mathbf{U}$ is defined [71]. To recap briefly, the N-S-F stress tensor is

$$\boldsymbol{\tau} = \mu\nabla\mathbf{U} + \mu\nabla\mathbf{U}^T - \frac{2}{3}\mu\text{tr}(\nabla\mathbf{U})\mathbf{I},$$

where terms with multiple components of \mathbf{U} are fully explicit, and may be grouped together in a new term, $\boldsymbol{\tau}_{\text{mc}}$, giving

$$\boldsymbol{\tau} = \mu \nabla \mathbf{U} + \boldsymbol{\tau}_{\text{mc}}. \quad (6.9)$$

Substituting kinematic viscosity, ν , for dynamic viscosity, μ , and using the expression $\mu = \nu \rho$, the first term of the shear stress tensor can be expanded into implicit and explicit components as follows:

$$\begin{aligned} \boldsymbol{\tau} &= \nu \rho \nabla \mathbf{U} + \boldsymbol{\tau}_{\text{mc}} \\ &= \nu \nabla (\rho \mathbf{U}) - \nu (\nabla \rho) \mathbf{U} + \boldsymbol{\tau}_{\text{mc}} \\ &= \nu \nabla (\rho \mathbf{U}) - \nu \nabla (\rho \mathbf{U}) + \mu \nabla \mathbf{U} + \boldsymbol{\tau}_{\text{mc}}. \end{aligned} \quad (6.10)$$

The divergence of the stress tensor in this form is then substituted back into the momentum equation. The identical terms in the last line of Eq. (6.10) are not cancelled in the final implementation, as one term is implicit and the other explicit — the original $\mu \nabla \mathbf{U}$ term has simply been expanded into implicit and explicit component parts [71]. OpenFOAM automatically places implicit terms into a matrix of coefficients for the equation to be solved, and explicit terms are collated in a source-term matrix. The presence of the implicit part of the shear stress term in the solution matrix improves convergence as it boosts the matrix's diagonal component.

In the `rhopEsonicFoam` code, the momentum equation given by Eq. (6.8) is implemented in the following form.

<pre> fvVectorMatrix rhoUEqn (fvm::ddt(rhoU) + fv::gaussConvectionScheme<vector> (mesh, phiv, rhoUScheme) .fvmDiv(phiv, rhoU) - fvm::laplacian(DrhoU, rhoU) + fvc::laplacian(DrhoU, rhoU) - fvc::laplacian(mu, U) - fvc::div(tauMC)); solve(rhoUEqn == -fvc::grad(p)); </pre>	<p>Momentum equation</p> $\frac{\partial(\rho\mathbf{U})}{\partial t}$ $+\nabla\cdot\mathbf{U}(\rho\mathbf{U})$ $-\nabla\cdot\nu\nabla(\rho\mathbf{U})$ $+\nabla\cdot\nu\nabla(\rho\mathbf{U})$ $-\nabla\cdot\mu\nabla\mathbf{U}$ $-\nabla\cdot\boldsymbol{\tau}_{mc}$ $=$ $-\nabla p$
--	--

Terms labelled `fvm::` are fully implicit terms, while those beginning `fvc::` are explicit. All source terms are included in the main body of the equation, with the exception of the pressure-gradient source term $-\nabla p$, which is included in the `solve` command.

The energy equation in `rhoPEsonicFoam` is also modified from the inviscid `rhoPSonicFoam` version given by Eq. (6.4). The energy equation in `rhoPEsonicFoam`, in terms of total energy ρE , is given by

$$\frac{\partial(\rho E)}{\partial t} + \nabla\cdot\mathbf{U}(\rho E) = -\nabla\cdot\mathbf{U}p + \nabla\cdot\kappa\nabla T + \nabla\cdot(\boldsymbol{\tau}\cdot\mathbf{U}), \quad (6.11)$$

where $\kappa\nabla T$ represents heat flux and $(\boldsymbol{\tau}\cdot\mathbf{U})$ is mechanical power flux, and both terms are explicit. As outlined for the momentum equation above it is helpful to be able to express some part of these source terms in implicit form. Following procedures laid down in [71], this is accomplished by using the definitions of Prandtl number,

$$\text{Pr} = \frac{\mu C_p}{\kappa}, \quad (6.12)$$

and specific heat ratio, $c_P = \gamma c_v$, to express the divergence of the heat flux in terms of internal energy e :

$$\nabla \cdot \kappa \nabla T = \nabla \cdot \left(\frac{\gamma \nu}{\text{Pr}} \right) \nabla \rho e. \quad (6.13)$$

The divergence of the translational part of the mechanical power flux $(\boldsymbol{\tau} \cdot \mathbf{U})_{\text{trans}}$ is then re-written in terms of kinetic energy:

$$\nabla \cdot (\boldsymbol{\tau} \cdot \mathbf{U})_{\text{trans}} = \nabla \cdot 2\nu \nabla \left(\frac{|\rho \mathbf{U}|^2}{2\rho} \right). \quad (6.14)$$

The diffusive coefficients of these two equations are $\gamma\nu/\text{Pr}$ and 2ν , and are approximately equal when $\gamma/\text{Pr} \approx 2$. As this condition is appropriate for many gas flows, the diffusive coefficients of heat and translational power flux can be replaced with a single coefficient term, D , multiplied by kinetic viscosity, ν . The definition of total energy given in Eq. (6.5) is then used to combine the heat flux and translational power flux into a single, implicit, total energy term:

$$\nabla \cdot D\nu \nabla (\rho E) = \nabla \cdot \left(\frac{\gamma \nu}{\text{Pr}} \right) \nabla \rho e + \nabla \cdot 2\nu \nabla \left(\frac{|\rho \mathbf{U}|^2}{2\rho} \right). \quad (6.15)$$

Then, in the same way that the shear stress tensor was separated into equal implicit and explicit component parts above and introduced into the momentum equation (see Eq. (6.10)), this implicit total energy term may be introduced to the energy equation by subtracting an equivalent explicit term and the original term. The energy equation is then implemented in `rhoEsonicFoam` as follows.

```

fvScalarMatrix rhoEEqn
(
    fvm::ddt(rhoE)
    + mvConvection.fvmDiv(phiv, rhoE)
    ==
    - mvConvection.fvcDiv(phiv, p)
    + fvm::laplacian(DrhoE, rhoE)
    - fvc::laplacian(DrhoE, rhoE)
    + fvc::laplacian(k, T, "laplacian(k,T)")
    + fvc::div
    (
        fvc::interpolate(mu)*mesh.magSf()
        *(fvc::snGrad(U) & fvc::interpolate(U))
    )
    + fvc::div
    (
        (
            (mesh.Sf() & fvc::interpolate(tauMC))
            & fvc::interpolate(U)
        )
    )
);

solve(rhoEEqn);

```

Energy equation

$$\partial(\rho E)/\partial t$$

$$+\nabla \cdot \mathbf{U}(\rho E)$$

$$=$$

$$-\nabla \cdot \mathbf{U}p$$

$$+\nabla \cdot D\nu\nabla(\rho E)$$

$$-\nabla \cdot D\nu\nabla(\rho E)$$

$$+\nabla \cdot \kappa\nabla T$$

$$+\nabla \cdot \mu\nabla\mathbf{U} \cdot \mathbf{U}$$

$$+\nabla \cdot (\boldsymbol{\tau}_{mc} \cdot \mathbf{U})$$

Again, `fvm::` terms are implicit terms and `fvc::` terms are explicit. The pressure correction loop that follows the energy equation in the solution procedure is identical to that used in the publicly released version of `rhoPsonicFoam`.

The range of boundary conditions implemented in `rhoEsonicFoam` includes Maxwell's velocity slip condition, incorporating the effects of thermal creep, as described by Eq. (3.8), and Smoluchowski's temperature jump condition as given in Eq. (3.9). As `rhoEsonicFoam` is designed to solve the momentum and energy equations with viscosity as a temperature dependent property only, i.e. the N-S-F

equations without constitutive scaling, dynamic viscosity and thermal conductivity are always assigned a spatially-constant value. The slip and jump boundary conditions are therefore implemented in terms of constant viscosity and Prandtl number, Pr , rather than the mean free path. As discussed in section 4.4.1, this relies on the velocity profile conforming to a Maxwellian equilibrium distribution, which limits the solver’s applicability to cases where $Kn \lesssim 0.1$ and Knudsen layer structure represents an insignificant proportion of the flow.

6.2.3 Compressible microflows solver

To implement constitutive scaling in `rhoEsonicFoam` and extend its applicability to transitional- Kn flows, further modifications must be made to the solver. Firstly, the effective viscosity models that are used to introduce the scaling must be implemented in the code. This is carried out in a similar manner to that described in section 4.4, and a range of effective viscosity models are available. For non-isothermal compressible cases, the thermal conductivity, which linearly relates heat flux and temperature gradient in the N-S-F equations must also be scaled, see Eq. (4.8). For this to be possible, thermal conductivity must be introduced to the solver as a variable field, with switches determining its value depending on whether or not constitutive scaling is used, and also on the constitutive-scaling model chosen. Appropriate effective thermal conductivity models have therefore been introduced in the solver, and the value of thermal conductivity is now calculated and updated alongside the viscosity models as part of the code’s main iterative loop.

Thermal conductivity and dynamic viscosity are related to each other by the Prandtl number Pr , which is given by Eq. (6.12). Consequently, the manner in which μ and κ are scaled relative to each other can be as influential on the simulation as the shape of the scaling functions used for individual fields. Two of the foremost constitutive-scaling schemes published, which each treat Prandtl number differently, are currently implemented in the modified `rhoEsonicFoam`

solver, although the framework of the solver is such that in future other models can easily be incorporated as they become available.

6.3 Constitutive scaling models

The currently implemented models are those proposed by Lockerby *et al.* [12] and Reese *et al.* [17], which will be referred to here as model A and model B, respectively. The main difference between the models is the relationship between their constitutive scaling functions for shear stress and for heat flux, that is to say, how combined viscosity and conductivity scaling affect Pr.

6.3.1 Model A

In model A, the scaling function given in Eq. (4.6) is taken alongside the dynamic viscosity to form an effective viscosity term that varies with normal distance to the nearest solid surface, i.e.

$$\mu_{\text{eff}_A} = \frac{\mu}{f(n/\lambda)}, \quad (6.16)$$

where the subscript *A* refers to a quantity used in model A. This is the constitutive scaling model that has been applied in earlier chapters of this thesis, and which has been tested in its isothermal form on several standard benchmark micro-flows [12, 14, 36].

Model A uses the definition of Prandtl number, which describes the relationship between momentum diffusivity and energy diffusivity, and is given in Eq. (6.12), to define its expression for scaling the thermal conductivity, κ . Given the hard-sphere, monoatomic gas model condition of a constant $\text{Pr} = 2/3$, then

$$\kappa_{\text{eff}_A} = \frac{\mu_{\text{eff}_A} c_p}{\text{Pr}} = \frac{3}{2} \mu_{\text{eff}_A} c_p. \quad (6.17)$$

So, in model A the relative magnitudes of the momentum and energy diffusivities are preserved from the original molecular model. In the modified rhoPESonic-

Foam solver, a fixed Pr value is established when model A is used, and the thermal conductivity field is calculated from this value in accordance with Eq. (6.17).

6.3.2 Model B

Constitutive scaling functions for Knudsen layers of both momentum and energy were recently proposed in [17, 45], using kinetic theory data from a wide literature survey to determine effective values of both dynamic viscosity and thermal conductivity. The effective quantities are presented in similar general form, with the original constitutive constants scaled by normal distance to the nearest wall and the appropriate accommodation coefficient for tangential momentum or energy, corresponding to that used in the velocity slip/temperature jump equations.

From [45], the replacement constitutive relationship for momentum (i.e. effective viscosity) is:

$$\mu_{\text{eff}_B}(n) = \frac{\mu}{1 - A_{KP} (D_{KP} \cdot \sigma_U + E_{KP}) \left(1 + \frac{\sqrt{\pi} n}{2 \lambda}\right)^{A_{KP}-1}}, \quad (6.18)$$

and the scaling function for energy (i.e. effective thermal conductivity) is:

$$\kappa_{\text{eff}_B}(n) = \frac{\kappa}{1 - A_{TJ} (D_{TJ} \cdot \sigma_T + E_{TJ}) \left(1 + \frac{\sqrt{\pi} n}{2 \lambda}\right)^{A_{TJ}-1}}. \quad (6.19)$$

The subscripts *KP* and *TJ* refer to Kramers' problem and the temperature jump problem, which were the kinetic-theoretical case studies used in the curve-fitting to derive the scaling functions; *A*, *D* and *E* are constants generated in the curve-fitting process, listed in Table 6.1 for the hard-sphere molecular model. Note that in this model the diffusivities of momentum and energy are not both scaled in the same way. As a result, any effective Prandtl number that were defined using those quantities would be non-constant. When model B is used in the modified `rhoEsonicFoam` solver, thermal conductivity is defined using Eq. (6.19) and an effective Prandtl number is then calculated from the scaled viscosity and thermal conductivity using Eq. (6.12). This is in contrast to using a constant Pr value

to define the thermal conductivity scaling from the viscosity scaling, and is the fundamental difference between models A and B.

μ -scaling	A_{KP}	D_{KP}	E_{KP}	σ_U
Coeff. value	-2.719	-0.293	0.531	1.0
κ -scaling	A_{TJ}	D_{TJ}	E_{TJ}	σ_T
Coeff. value	-2.142	-0.745	1.295	1.0

Table 6.1: Coefficients used in Eqs. (6.18) and (6.19) to define the scaling functions of model B.

It should be noted that the scaled diffusive quantities in both model A and model B are purely effective values, and were not intended by the original proponents of constitutive scaling to be used to define physical values of, for example, mean free path or Prandtl number. Rather, the original viscosity and thermal conductivity should be used to define physical quantities. Within a CFD framework, however, it is important that physical quantities are retrievable from the scaled model. For example, in the hard-sphere model approximation of monoatomic gases, flows incorporating both momentum and energy fluxes may be shown to have a constant Prandtl number, $Pr = 2/3$ [86]. If this value is not recovered using the “true” velocity or temperature profiles produced by the scaling approach, it is possible that this is due to a physical inconsistency in the scaling model.

Comparing Models A and B: Figures 6.1 and 6.2 illustrate the variation of effective dynamic viscosity μ_{eff} and effective thermal conductivity κ_{eff} with normal distance from a planar wall. The scaled quantities are compared to nominal constant values of μ and κ respectively. Model A scales consistently for both dynamic viscosity and thermal conductivity, producing effective quantities 0.59 times their original value at the wall, and reaching the full value of the original quantity outside the Knudsen layer region. Model B is seen to apply different

scaling to each quantity, resulting in wall values of $\mu_{\text{eff}} = 0.62\mu$ and $\kappa_{\text{eff}} = 0.47\kappa$, and again reaching the full original value outwith the near-wall region of the flow.

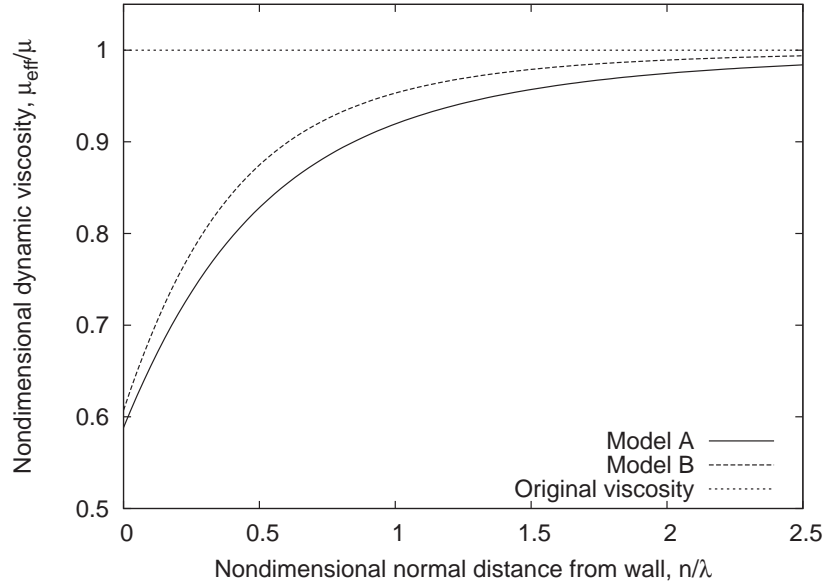


Figure 6.1: Effective viscosities provided by the scaling models, compared to (constant) nominal viscosity.

Figure 6.3 shows the ratio of effective viscosity to effective thermal conductivity predicted by each scaling model, which is directly comparable to the effective Prandtl number (i.e. Pr from Eq. (6.12), but using effective quantities and without the specific heat at constant pressure c_p as a coefficient). In the hard-sphere molecular model, only translatory exchanges of energy are present, leading to a fixed ratio of momentum to thermal energy exchange for a fixed collision time, which in turn leads to the constant Prandtl number condition. What the figure illustrates is that using model B effectively induces a difference between the magnitude of momentum exchange and energy exchange in any given collision. This violates the constant Prandtl number condition of the hard-sphere gas model — which was the model from which the function in Eq. (6.19) was derived. As such, model B may be inappropriate for use in cases where both momentum and energy exchange are considered. In isothermal or isoflux cases, however, model B could still represent a legitimate form of constitutive scaling.

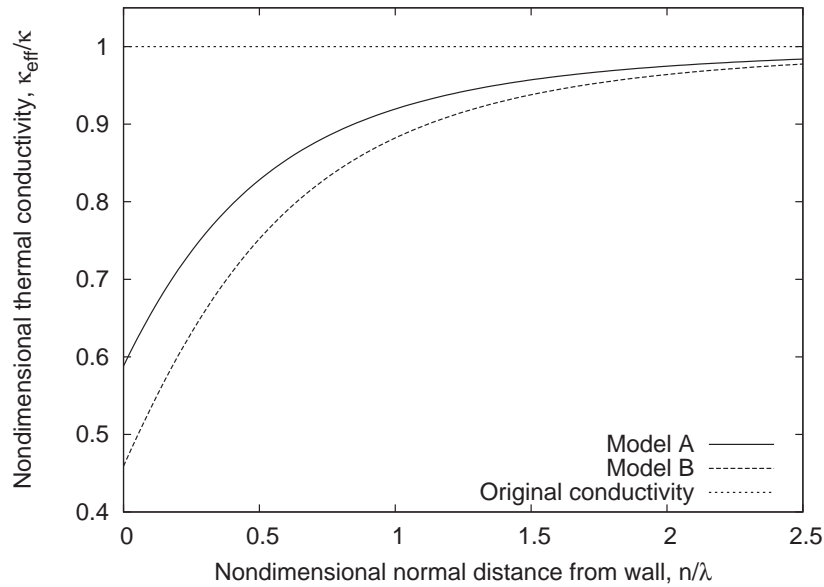


Figure 6.2: Effective thermal conductivities provided by the scaling models, compared to (constant) nominal thermal conductivity.

6.4 Half-space problems

In rarefied flows, velocity slip and temperature jump arise within the Knudsen layer as the difference in the average molecular properties of the wall and those of the gas at the wall. The Knudsen layer thickness is the average distance over which these discontinuities would be equilibrated in a quiescent gas (or in an unheated gas for the thermal case). The Knudsen layer regions are illustrated schematically in Figs. 4.1 (shown in section 4.1) and 6.5 as extending $\approx 2\lambda$ from the planar surface.

6.4.1 Kramers' problem

Kramers' problem was introduced briefly in Chapter 4, and is defined as the incompressible, isothermal flow of a gas in a half-space under a constant shear stress that is applied tangentially to a stationary planar wall. The shear stress generates a linear velocity profile normal to the wall, except in the near-wall Knudsen layer region where an increase in strain-rate is observed. This momentum Knud-

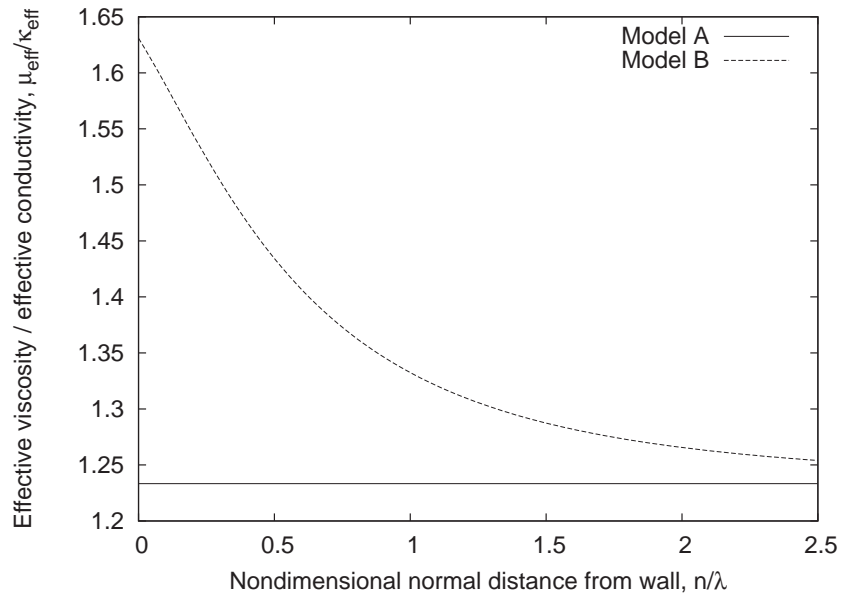


Figure 6.3: Ratio of effective viscosity to effective thermal conductivity (ratio of momentum to energy diffusivity) provided by the scaling models.

sen layer arises due to incomplete accommodation of momentum between the gas and the surface.

Kramers’ problem is a very simple model of flow in, for example, microscale comb-drives, where oscillating parts induce shear stresses in gas surrounding the device. The drag force between surfaces depends directly on the surface-normal velocity gradient, which can be substantially altered by rarefaction.

Although relatively few experimental results are available for constant-shear problems, there are many reliable kinetic theory solutions in the published literature. Typically, these solutions report a velocity defect, rather than a velocity profile, varying with normal distance to the stationary wall. Velocity defect is taken to be the difference between a standard N-S-F solution to the problem, with a “fictitious” macroslip coefficient applied to Maxwell’s slip boundary condition, typically $\zeta_{\text{slip}} = 1.146$, and the true velocity profile in the Knudsen layer [6].

In the derivation of model B, the concept of velocity defect was used to define a dimensionless function $S(n/\lambda)$ describing the spatial structure of the Knudsen layer [45]. This is effectively a shape defect term, describing Knudsen layer

changes in the near-wall profiles of given macroscopic quantities of interest, such as velocity or temperature. The profile defects are curve-fit from a wide range of data to establish the coefficients given in Table 6.1. By re-casting Eq. (4.6) in the form of Eqs. (6.18) and (6.19), it is possible to express model A in the form of model B, using coefficient values of $A = -2$, $D = 0$ (i.e. the model A function is not accommodation-coefficient dependent) and $E = 0.35$. Combining Eqs. (9) and (11) given in [17], a general equation for the shape defect is established as

$$S(n/\lambda) = (D\sigma + E) \left(1 + \frac{\sqrt{\pi} n}{2 \lambda} \right)^A, \quad (6.20)$$

where σ is the surface accommodation coefficient of either tangential momentum or energy, and the $\sqrt{\pi}/2$ term is introduced to convert between those authors' definition of mean free path and the definition used here, Eq. (2.2). Using the dimensionless shape defect, $S(n/\lambda)$, it is possible to compare both constitutive scaling models directly to the kinetic theory data presented in [6], as shown in Fig. 6.4.

It is obvious from Fig. 6.4 that the Knudsen layer predicted by model B is much closer to the kinetic theory data than the structure predicted by model A. This would imply that, at least in this particular case, model B would be expected to give more accurate results when applied as a scaling relationship to the N-S-F equations. It is noteworthy, however, that very close to the wall even the curve-fit of model B fails to capture accurately the gradient of the shape defect, which determines, in practice, the shape of the Knudsen layer.

6.4.2 The temperature jump problem

The temperature jump problem (Fig. 6.5) is a constant heat flux in a half-space, applied normally to a planar wall in a quiescent gas. In the thermal Knudsen layer near the solid surface the temperature gradient increases, reflecting the incomplete exchange of thermal energy between the gas and the wall. Although limited to diffusive effects, this type of problem is representative of some specialist cool-

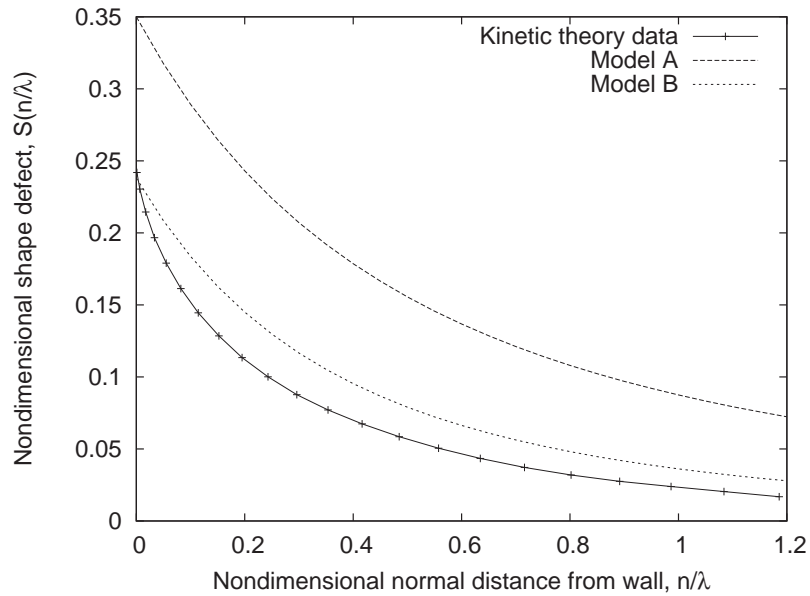


Figure 6.4: Knudsen layer shape defect predicted for Kramers’ problem: kinetic theory data (points connected by solid line) compared to model A (dashed line) and model B (dotted line).

ing applications, and of recently published experiments which attempt to quantify gas-surface interactions by measuring thermal accommodation coefficients [87].

The thermal Knudsen layer structures predicted by the constitutive scaling models for the temperature jump problem are shown in Fig. 6.6, in comparison to kinetic theory data from [4]¹. Again, the shape defect predicted by model B would seem to provide a much better representation of the thermal Knudsen layer, as observed through the temperature profile. Model A provides a realistic estimate of the shape defect gradient, i.e. the form of the thermal Knudsen layer, but under-predicts the extent of the Knudsen layer (the magnitude of the shape defect).

Considered together, Figs. 6.4 and 6.6 illustrate that kinetic models, which only consider transfer of momentum or energy, not both, appear to predict different Knudsen layer structures [4, 6]. This difference is the source of the vari-

¹Very few data points are given in Loyalka’s paper. However, it remains one of the most reliable available sources of data for the temperature jump problem.

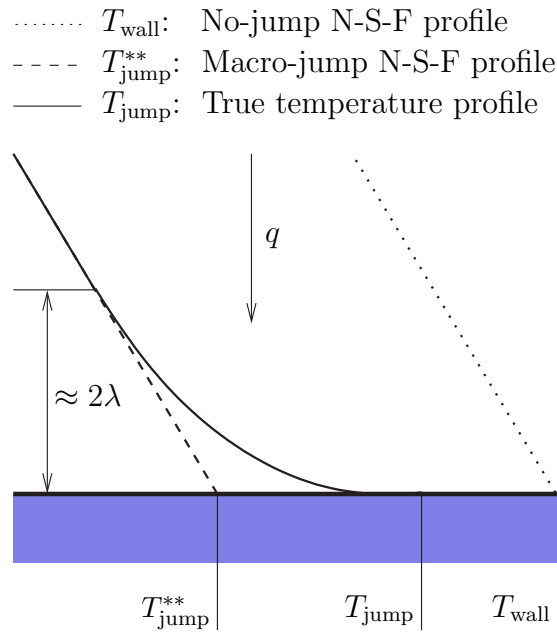


Figure 6.5: Schematic of the temperature jump problem showing constant applied heat flux, q ; traditional, no-jump N-S-F solution (T_{wall} : dotted line), N-S-F solution with second order macro-jump boundary condition (T_{jump}^{**} : dashed line) and true temperature profile (T_{jump} : solid line).

ation in Prandtl number that occurs in model B. To maintain the monoatomic, hard-sphere constant Prandtl number of $2/3$, a single Knudsen layer structure, applicable to both momentum and energy transfer, is required — such as that shown by model A. The model A trace in Figs. 6.4 and 6.6 is roughly equidistant between the Kramers’ problem and temperature jump problem profiles, with a gradient that reasonably represents both kinetic theory solutions. It is perhaps for this reason that model A appears to produce reasonable results across a range of flow configurations [12, 14, 36], although its original derivation was from an isothermal Kramers’ problem case [3].

6.4.3 Summary

In analysing Kramers’ problem and the temperature jump problem, the functions implemented in OpenFOAM to apply constitutive scaling have been assessed. The impact of each model on the relationship between energy and momentum

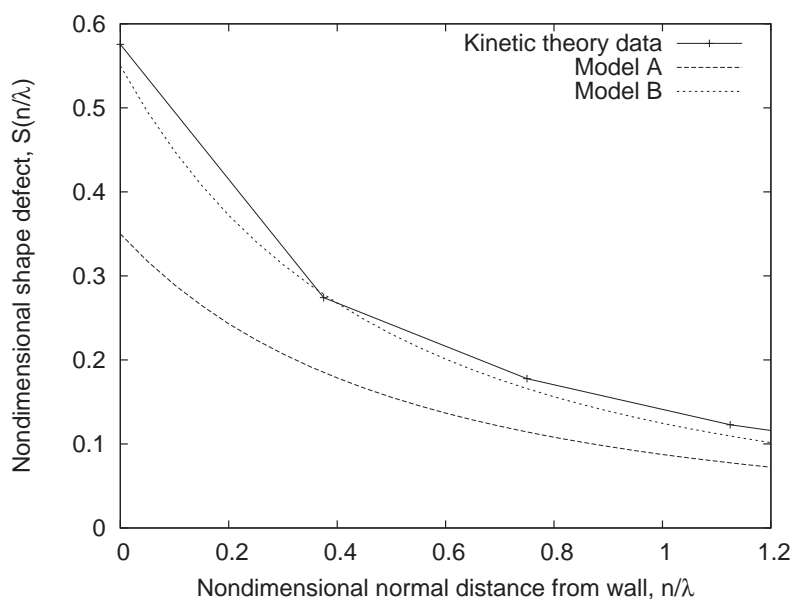


Figure 6.6: Knudsen layer shape defect predicted for the temperature jump problem: kinetic theory data (points connected by solid line) compared to model A (dashed line) and Model B (dotted line).

diffusivity has also been discussed. In order to validate the `rhoEsonicFoam` solver and investigate the potential impact of introducing a non-constant effective Prandtl number with model B, the implemented constitutive scaling functions must be applied to a more complex case where energy and momentum are exchanged simultaneously.

6.5 Compressible micro-Couette flow

As a validation exercise, the modified `rhoEsonicFoam` solver is used to simulate high-speed Couette flow of argon gas in 2D microchannels. The Couette flow problem is essentially a 1D flow, but is solved in CFD as a 2D planar flow in a channel. All of the constitutive-scaling models and solvers are implemented fully in 3D in OpenFOAM, however, to enable other more general problems to be investigated in the future.

This Couette flow would be typical of those found in computer hard-disks, where it is important to be able to quantify the position of the disk-reading head

over the data-storing platter. The drag force experienced by the reader-head and other macroscopic fields such as velocity can be substantially altered by gas rarefaction.

The 2D channel configuration for Couette flow is shown in Fig. 6.7. The upper wall remains stationary and the lower wall moves in the positive x -direction at Mach 1 (with the local speed of sound calculated using the wall temperature), generating a constant tangential shear stress. The pressure in planar Couette flow also remains constant, hence, compressibility effects in this configuration arise from changes in density that occur due to viscous heating increasing the temperature of the flow. The simulated channel length is a minimum of $60\mu m$, and flow is fully developed in the centre of the system. The channel height in the y -direction is varied in order to determine the Knudsen number of the case. For validation purposes, results from OpenFOAM are compared to DSMC data up to a Kn -value of 0.5, which is relatively high for any type of continuum solution [18]. Then, in order to investigate the behaviour of the constitutive scaling models beyond the limits of their applicability, a further, high- Kn case is of 0.8 is also analysed. The different channel heights used are given in Table 6.2, with corresponding Kn values and Reynolds numbers. The Kn values are determined using Eq. (6.1), with Mach number defined as $Ma = \mathbf{U}/\sqrt{\gamma RT}$ and Reynolds number defined as

$$Re = \frac{\mathbf{U}_{Ma=1}H}{\nu}, \quad (6.21)$$

where ν is the kinematic viscosity, H is the height of the channel, and $\mathbf{U}_{Ma=1}$ is the velocity of the moving wall at $Ma = 1$, i.e. maximum velocity in the system.

Argon gas at a temperature of 300K is used as the working fluid, with both wall temperatures fixed at 300K. Gas properties are determined using [75]. The use of argon makes [18] a particularly appropriate source of validation data: it is a monoatomic gas, which is in keeping with the assumptions of molecular behaviour inherent in the velocity slip and temperature jump conditions [8], and in the

Kn	0.01	0.1	0.2	0.5	0.8
$H (\times 10^{-6}\text{m})$	7.09	0.709	0.3545	0.1418	0.0886
Re	162.71	16.27	8.14	3.25	2.03

Table 6.2: Table of channel heights used to vary Kn in Couette flow simulations, with corresponding Reynolds numbers for each case.

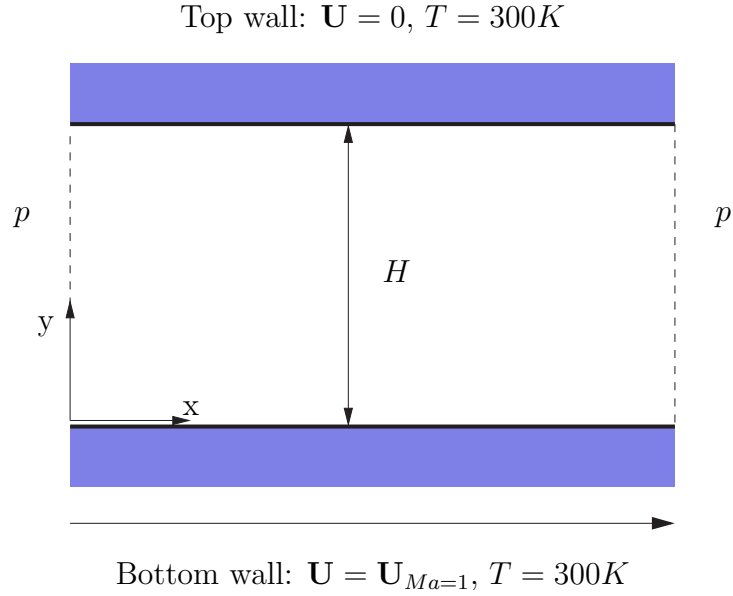


Figure 6.7: Couette flow configuration and nomenclature for the compressible CFD analysis; $\mathbf{U}_{Ma=1}$ is the velocity applied to move the lower wall at the local speed of sound.

derivation of the constitutive scaling relationships from hard-sphere molecular force interaction models [12, 17].

At the channel ends, a fixed-value boundary condition on pressure is used, $p = 101.325\text{kPa}$, and the temperature and velocity gradients normal to the (parallel) inlet and outlet faces are set to zero. Velocity slip and temperature jump boundary conditions (Eqs. 3.8 and 3.9) are used at the channel walls; tangential accommodation coefficients of momentum and energy are fixed at $\sigma_U = \sigma_T = 1$, with the slip/jump coefficients $\zeta_{\text{slip}} = \zeta_{\text{jump}} = 0.8$. Structured hexahedral meshes, tested to ensure grid-independent results, are used in all cases. The cell den-

sity increases towards the channel walls, in order to capture the Knudsen layer structure accurately.

In combining the transport of both energy and momentum, this shear-driven case exposes several limitations of model B.

- The relative diffusivities of energy and momentum for the monoatomic hard-sphere model must be fixed by the condition $\text{Pr} = 2/3$ — Model B violates this condition and is therefore, strictly, inappropriate for application to this case.
- Model B is not only more computationally intensive than model A, as two effective quantities are calculated, but it is also less numerically stable. This is due to the relative magnitudes of the diffusive terms in the momentum and energy equations being altered by scaling viscosity and thermal conductivity with different functions. This makes achieving converged solutions more difficult in a segregated analysis, limiting in practice the maximum Courant number that can be used, and greatly increasing overall computational effort.
- For this case, the velocity profiles produced by model B are near-identical to those of model A, as illustrated in Fig. 6.8. Temperature results from model B are somewhat less accurate than those from model A (in comparison to DSMC), however, as is illustrated in Fig. 6.9. In compressible Couette flow, a temperature increase is observed in the channel due to viscous heating. Whilst it is important to note that both models capture the same type of temperature profile as that predicted by DSMC, with a similar magnitude of the peak (channel-centre) temperature, there are differences between the model results and the DSMC data. These may be attributed to a) the fact that both models are derived from linear problems, so may not be applicable to Couette flow where the temperature profile is parabolic, and b) that DSMC is able to capture other rarefaction effects, such as tangential heat

fluxes, which the present models cannot. (The latter fact may be expected to result in more pronounced divergences between these models and DSMC in simulations of more complicated flow systems.)

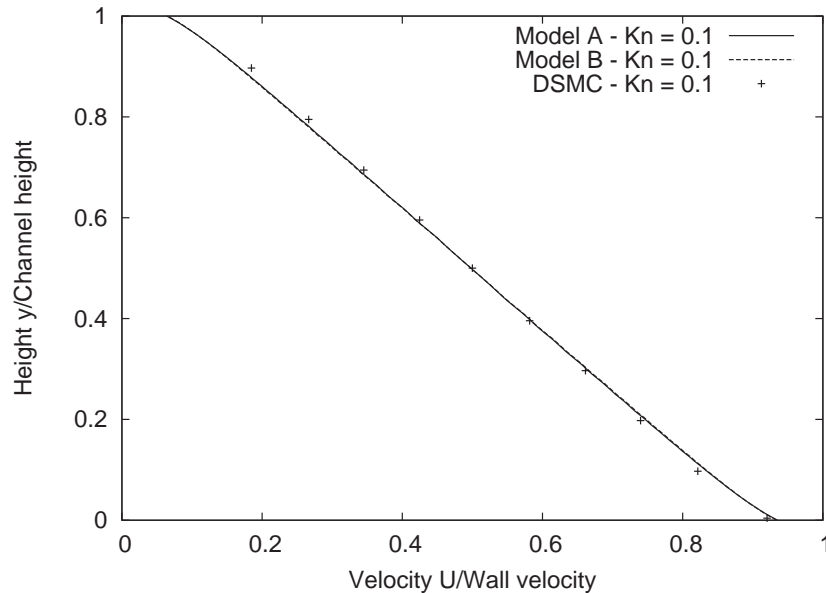


Figure 6.8: Micro-Couette velocity profiles predicted by model A, Model B and DSMC for $Kn = 0.1$.

Considering these factors, and the limited applicability of model B in terms of recovering a constant Prandtl number physically, validation results reported below are taken from model A simulations only.

Figure 6.10 shows the cross-channel velocity profiles predicted using the OpenFOAM implementation of model A for a range of Kn values (shown as lines), compared to the corresponding DSMC data (shown as points) from [18]. Velocity is non-dimensionalised by the velocity of the moving lower wall; the spatial position in the y -direction is non-dimensionalised by the appropriate channel height. As the figure illustrates, the Knudsen layer structure is represented relatively well by the CFD, although as Kn increases the deviation from the DSMC data does become more appreciable.

Figure 6.11 shows temperature profiles in the lower half of the channel for the

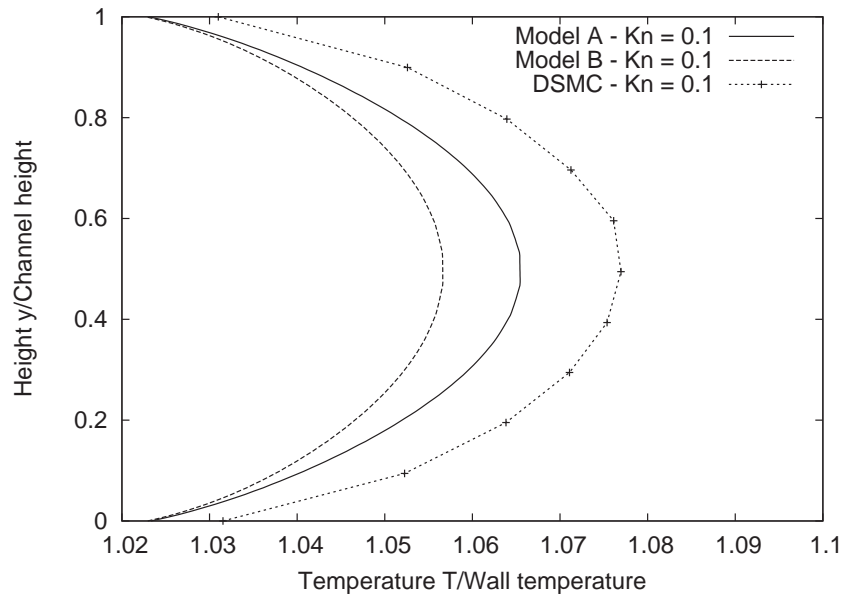


Figure 6.9: Micro-Couette temperature profiles predicted by model A, Model B and DSMC for $Kn = 0.1$.

compressible Couette flow case. Results obtained using model A are compared to results from the standard form of the N-S-F equations. First, the no-slip, no-jump boundary conditions common to macroscale CFD are used; then, these are replaced with slip and jump boundary conditions from Eqs. (3.8) and (3.9). Temperature is non-dimensionalised by the fixed wall temperature. Results are shown for two key Kn values, 0.01 and 0.1, which are close to the centre and the upper limit of the slip-flow regime, respectively [2]. The no-slip/no-jump model is shown as a single solid line, which is the same for both of these Kn values, given that the N-S-F equations fail to predict altered flow profiles with increasing Kn .

The introduction of slip and jump boundary conditions improves the performance of the N-S-F model, but nonlinear Knudsen layer effects remain beyond its scope. As shown in Fig. 6.11, at the lower limit of the slip regime, the difference between the N-S-F with slip/jump boundary conditions and the constitutive-scaling model is small, and only practically observed as a very slightly increased temperature gradient close to the wall. At this Kn , the scaled equations and

the N-S-F equations return near-identical temperature jump values at the wall. As Kn increases to 0.1, the difference between the standard N-S-F model and model A becomes marked, with model A predicting lower temperatures across much of the flow, and a noticeably smaller temperature jump at the wall. The temperature gradient is also seen to increase near the wall, reflecting the presence of a thermal Knudsen layer — an effect not captured by the unscaled N-S-F equations, regardless of the boundary conditions applied. This illustrates that even for flows with Kn values traditionally considered to be part of the slip regime, the structure of the Knudsen layer can significantly impact macroscopic quantities of interest. When Kn approaches the upper limit of the slip regime and tends towards the lower limit of the transition regime, it is important that numerical models should capture Knudsen layer behaviour.

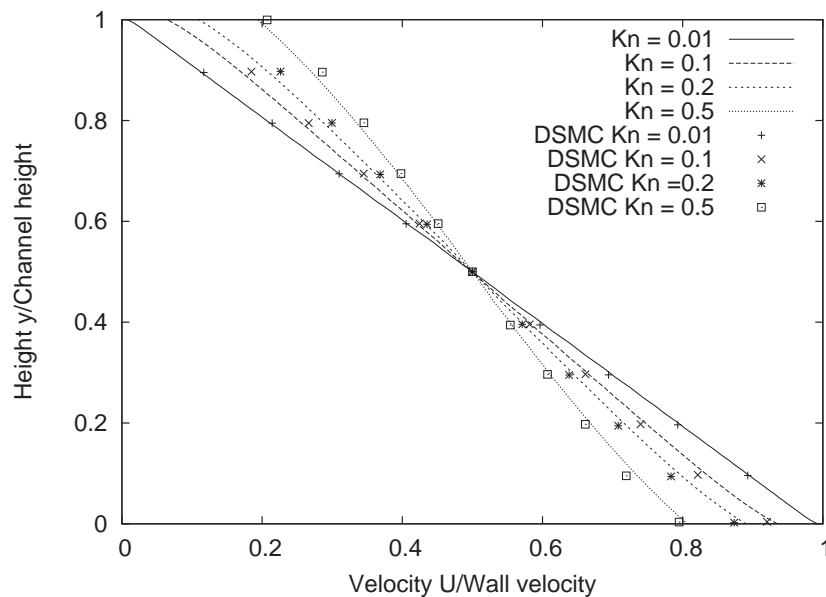


Figure 6.10: Compressible micro-Couette flow velocity profiles; comparison of model A results (lines) to DSMC data (points).

6.5.1 Discussion

One of the primary advantages of constitutive-relation scaling is that it is relatively straightforward to implement but is able to capture some of the trends

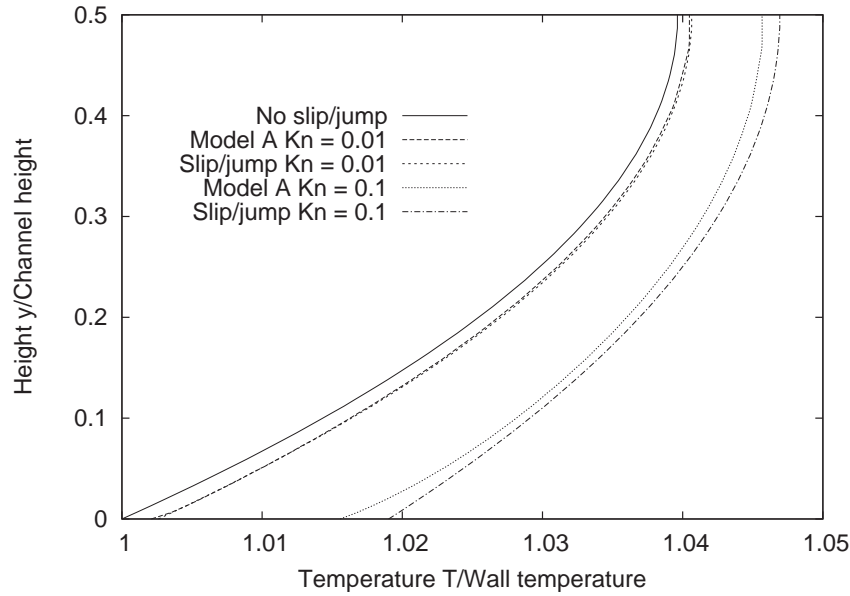


Figure 6.11: Compressible micro-Couette flow temperature profiles predicted by model A.

associated with the complex non-equilibrium physics of the Knudsen layer. As shown above, when applied to lower Kn transitional flows, constitutive scaling can offer greatly improved accuracy over simple N-S-F solutions, and capture the behaviour of Knudsen layers to some extent [18]. This performance improvement does not provide accuracy of the order of discrete or kinetic methods, however it can substantially improve continuum-simulation predictions of macroscopic quantities of interest, such as mass flowrate [37].

In this chapter a fully compressible implementation of the constitutive scaling approach in conventional CFD has been validated with a reasonable degree of success. The method could, however, be advanced with the derivation of new scaling models, in place of the models A and B investigated here. Both of these models are phenomenological in nature, as they are curve-fit from pre-existing (and case-specific) Knudsen layer solutions using other independent methods. They are also derived from kinetic solutions that use only the hard-sphere molecular model. A physical analysis of near-wall intermolecular interactions, and deriving scaling functions from more complex force-interaction laws (e.g. soft-spheres),

would provide a more general model.

Certain physical flow features, such as wall-normal shear stresses or tangential heat fluxes, and the Knudsen minimum, also seem to be beyond the scope of existing constitutive scaling within an N-S-F framework. While replacing the scaled N-S-F equations with a higher-order continuum model is a potential alternative to this technique, no single higher-order equation set has, as yet, demonstrated universal superiority [37]. Higher-order models also require additional boundary conditions, which can be difficult to obtain or prescribe.

While isothermal flow over spheres, Couette flow between rotating cylinders and flow through channels with venturi-type constrictions have all been successfully analysed previously using model A [12, 14, 36], it is important to explore the applicability of the model. For example, Fig. 6.12 shows the temperature profile predicted by model A for the micro-Couette flow case, with results for the high Kn -value of 0.8 included. The CFD initially shows higher maximum temperatures and a more linear profile as Kn increases, comparable to the data available in [18, 88]. But lower maximum temperatures start to appear as $Kn \rightarrow 0.5$, as the Knudsen layers from opposite sides of the channel begin to interact with each other, and boundary slip/jump effects increase. The scaling method effectively prescribes a velocity/temperature gradient dependent only on normal distance from a surface, and may not properly account for this physical coupling between Knudsen layers. It also makes use of Maxwell's and Smoluchowski's phenomenologically-derived boundary conditions for gas-solid interactions and, as Kn increases, slip/jump effects become dominant, magnifying errors arising at the system boundaries [3].

The temperature profiles produced are, of course, accommodation-coefficient dependent. In order to isolate the slip/jump effects, the compressible micro-Couette flow case detailed above has been reassessed using both model A (the N-S-F equations scaled using Eqs. 6.16 and 6.17) and the standard unscaled N-S-F equations, with different combinations of tangential accommodation coefficients

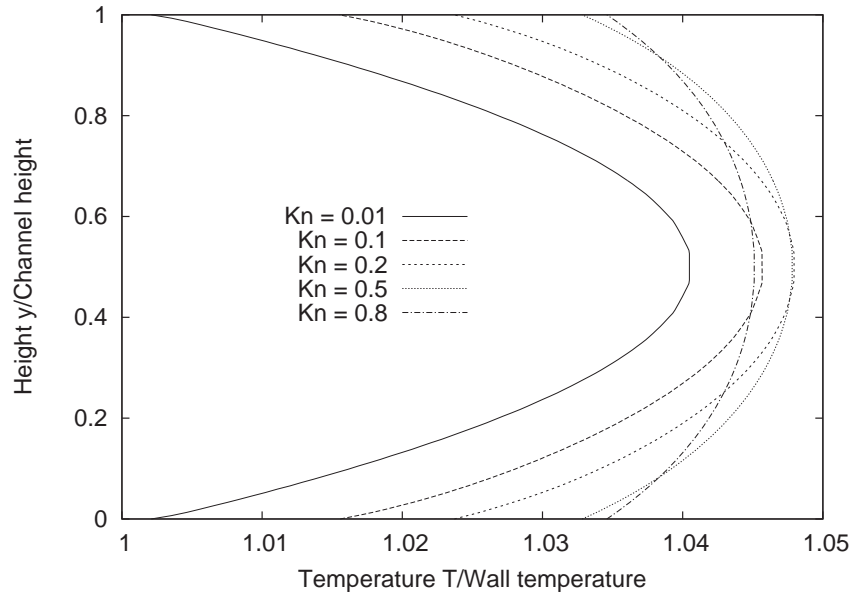


Figure 6.12: Temperature profiles predicted by model A, with high- Kn results.

for energy and momentum. Two different values of accommodation coefficient are used, first $\sigma = 1$ for comparison to Xue's DSMC [18], then $\sigma = 0.8$, a value typical of argon flows in silicon channels [79]. For both simulation types, four combinations of σ_U and σ_T are used:

$$\begin{aligned} \sigma_U &= 1 & \sigma_T &= 1, \\ \sigma_U &= 0.8 & \sigma_T &= 1, \\ \sigma_U &= 1 & \sigma_T &= 0.8, \\ \sigma_U &= 0.8 & \sigma_T &= 0.8. \end{aligned}$$

In the model A cases, microslip coefficients of $\zeta_{\text{slip}} = \zeta_{\text{jump}} = 0.8$ are used, and in the N-S-F analyses, the standard values of $\zeta_{\text{slip}} = \zeta_{\text{jump}} = 1$ are applied.

Figure 6.13 shows results from model A at Kn values of 0.2, 0.5 and 0.8 when $\sigma_U = \sigma_T = 0.8$, comparable to the high- Kn results shown in Fig. 6.12 where $\sigma_U = \sigma_T = 1$. The decrease in the accommodation coefficients is seen to increase

the temperature jump at the wall, and the crossover of the maximum temperature predictions has occurred at a much lower Kn . Therefore, even for relatively small changes in the tangential accommodation coefficients, large variations in the results of numerical analyses can be observed. As several recent studies have shown low accommodation coefficients to be practically realisable — e.g. σ_U values as low as 0.52, arguably, for carbon nanotubes [89] — different accommodation coefficients, and the accuracy with which they are determined in experimental cases, are likely to have an important effect on many types of continuum models for rarefied gas flow.

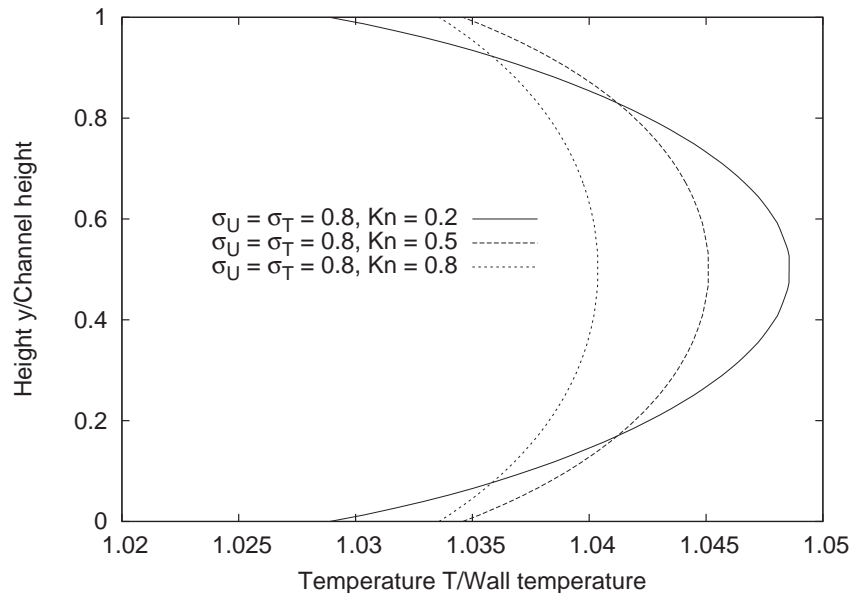


Figure 6.13: Temperature profiles predicted by model A; results as Kn increases while $\sigma_U = \sigma_T = 0.8$.

Also of interest is the interaction between the two types of accommodation coefficient. In N-S-F analyses at high Kn it was found that when energy and momentum accommodation coefficients were equal, at either 0.8 or 1, the predicted temperature jump at the channel walls was relatively similar, as is the predicted maximum temperature at the channel centre. However, if one accommodation coefficient is set to 0.8 and the other to 1, the behaviour of the simulation can be significantly altered.

To illustrate, Fig. 6.14 shows how the maximum predicted temperature (the temperature at the channel centre) varies with Kn . Each accommodation coefficient combination displays a definite peak in the predicted temperature, occurring in the range of Kn values between about 0.15 and 0.45. The largest maximum temperatures are predicted when the energy accommodation coefficient is at its lowest value of $\sigma_T = 0.8$, with momentum accommodation coefficient $\sigma_U = 1$. Conversely, when the momentum accommodation coefficient is $\sigma_U = 0.8$, and the energy accommodation remains at $\sigma_T = 1$, the maximum predicted temperature is at its lowest.

As shown in Fig. 6.14, these highest and lowest maximum temperature profiles are equidistant from the “reference” state where $\sigma_U = \sigma_T = 1$. This implies that energy and momentum are assumed to be exchanged at the same rate when Maxwell’s and Smoluchowski’s boundary conditions are used simultaneously, which is unlikely to be true of any physical system. For example, returning to the earlier discussion of Prandtl number, we know the momentum diffusivity to be only a proportion of the energy diffusivity, and momentum is exchanged at a faster rate than energy [3]. Accommodation coefficients are not physical properties of a surface, but rather they arise from the interaction between gas and wall molecules, and little is really known about the complex physics of gas flow in near-surface regions. It is therefore likely that more physically-based boundary conditions, such as Langmuir’s slip model, based on surface chemistry, would be better suited to many practical micro-engineering flow simulations [52].

6.5.2 Summary

By simulating compressible micro-Couette flow with constitutive scaling in OpenFOAM, it has been shown that the approach has some merit for practical applications. It is simple to apply, is implemented in an extensible framework and validation of the results produced with available DSMC data, shown in Figs. 6.8–6.10, inspires confidence in its ability to incorporate key rarefaction effects, to

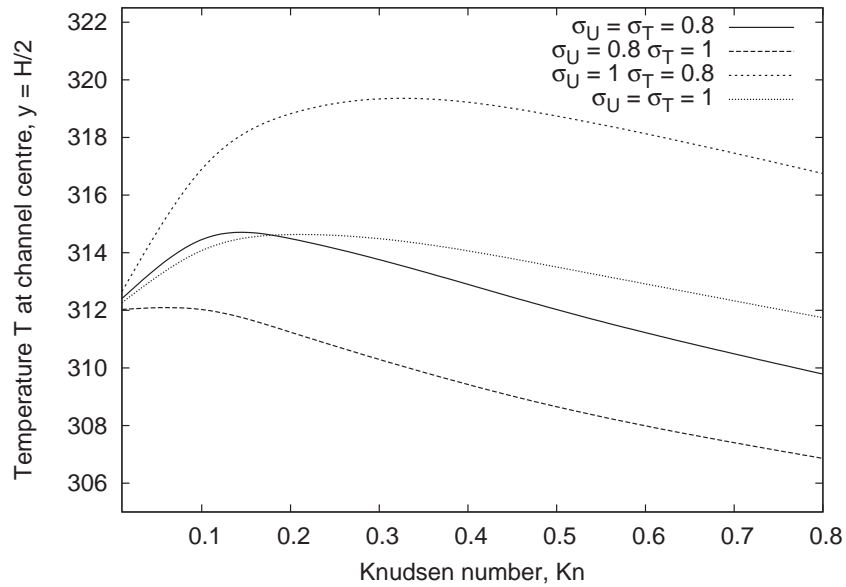


Figure 6.14: Predicted temperature (in K) at the centre of the channel in compressible micro-Couette flow (i.e. the maximum temperature), plotted against Knudsen number.

some extent, in continuum simulations. That said, there are some limitations to the method, particularly for application to compressible flows. As demonstrated, considerable care must be taken in choosing the correct models for the effective quantities, scaling coefficients and boundary conditions. The computationally-inexpensive nature of constitutive scaling in CFD when compared to discrete methods, and its ability to reproduce key rarefaction effects, suggest that the approach has the potential to become a useful tool for design applications. This will be particularly true for more complex 3D microflow configurations, to which very few discrete or kinetic models may be practically applied [26].

Chapter 7

A new approach to constitutive-scaling

In this thesis, constitutive scaling has been shown to be an efficient and effective method of including gas rarefaction effects in continuum fluid dynamics simulations. However, in its present form, constitutive scaling is dependent on detailed kinetic theory solutions providing appropriate functions with which to create an effective viscosity (or thermal conductivity) [12, 17]. Although it has been shown that it is possible to apply current constitutive models successfully to some cases beyond the limits of their original derivations, it would be beneficial if scaling functions could be derived in more general form.

Rarefaction is most commonly classified using a standard definition of Kn , given by Eq. (1.1) for incompressible flows and by Eq. (6.1) for compressible flows. In some systems, it is possible to have a low global value of Kn , but for areas of the flow to be locally rarefied [27]. This occurs particularly in compressible flows, where large density gradients can cause local rarefaction. Local rarefaction can be characterised using a local Knudsen number:

$$Kn_{\text{local}} = \frac{\lambda}{\theta} \frac{\partial \theta}{\partial x}, \quad (7.1)$$

where θ is a macroscopic variable and $\partial\theta/\partial x$ is its gradient in an arbitrary direction [27]. Current constitutive scaling functions presented in [12, 17] are dependent only on variation of effective viscosity and effective thermal conductivity

with the equilibrium mean free path of gas, λ , and normal distance to the nearest bounding surface. In cases where the global Kn -value is low but Kn_{local} is large, these scaling functions will predict only a thin Knudsen layer at system boundaries, which does not capture the true extent of rarefaction in the system. This limitation of the current form of constitutive scaling could perhaps be alleviated by using a more general model for rarefaction-based scaling in gas flows.

In this chapter, a new methodology for determining constitutive scaling functions empirically is proposed and an initial test-case is presented. The case is used to demonstrate how effective quantities may be related to local parameters of a system, and the potential for development of this new approach is discussed.

7.1 Identifying a scaling function

In applying an effective viscosity to alter the relationship between shear stress and strain-rate, constitutive scaling is effectively “distorting” an N-S-F velocity profile to incorporate a Knudsen layer. By considering the features that characterise Knudsen layers in a given flow configuration, such as increased strain-rate or temperature gradient near system boundaries, then it is possible to determine functions that describe mathematically how an N-S-F velocity or temperature profile should be altered to include key Knudsen layer effects. For example, pressure-driven flow in channels has a parabolic velocity profile whilst shear-driven flow is largely linear. The mathematical functions describing the difference between these solutions and their rarefied counterpart flows (found using DSMC or similar) are therefore very different. Scaling the N-S-F equations based on case-specific differences in shape between rarefied and non-rarefied profiles, rather than a single fixed function of distance to the nearest wall, is constitutive scaling from a different perspective. In theory, this approach could be used to derive more general constitutive scaling functions, expressed in terms of system parameters such as geometry, flow conditions and Knudsen number, Kn .

To test this hypothesis, a simple Poiseuille flow case is considered. The case

comprises isothermal, pressure-driven flow through a 2D rectangular channel, where the Kn -value of the system may be varied by altering the channel height, $2h$. The analytical solution to the Navier-Stokes equations for this flow, with or without slip at the system boundaries, gives a parabolic velocity profile. For no slip at the system boundaries

$$u_{\text{N-S}}(y) = \frac{1}{\mu} \frac{dp}{dx} \left(\frac{y^2}{2} - hy \right), \quad (7.2)$$

where μ is a constant dynamic viscosity, dp/dx a longitudinal pressure gradient, h the half-channel height and y the cross-channel position. For Poiseuille flow in channels, velocity profiles incorporating the Knudsen layer are not perfectly parabolic; the gradient of the velocity is steeper within one to two mean free paths of the channel walls than that predicted by the Navier-Stokes equations. To replicate this Knudsen layer shape it is proposed that an elliptical function be added to Eq. (7.2). The general expression describing an ellipse is

$$\frac{(x - x_0)^2}{a^2} + \frac{(y - y_0)^2}{b^2} = 1, \quad (7.3)$$

where (x_0, y_0) is the origin of the ellipse and a and b are its major and minor axes respectively, as shown in Fig. 7.1. Positioning the ellipse such that its origin is at $(0, h)$ in the centre of the Poiseuille flow channel, the shape of the ellipse as a function of its height y is given by

$$x(y) = \sqrt{a^2 - \frac{a^2(y - h)^2}{h^2}}. \quad (7.4)$$

To relate the dimensions of the ellipse to those of the parabolic velocity profile, its half-height b is equated with the half-channel height h , and its major axis a is equated to the peak velocity given by the parabolic profile, $u_{\text{N-S}}(h)$. A velocity-type profile that would be described by the ellipse can therefore be expressed as

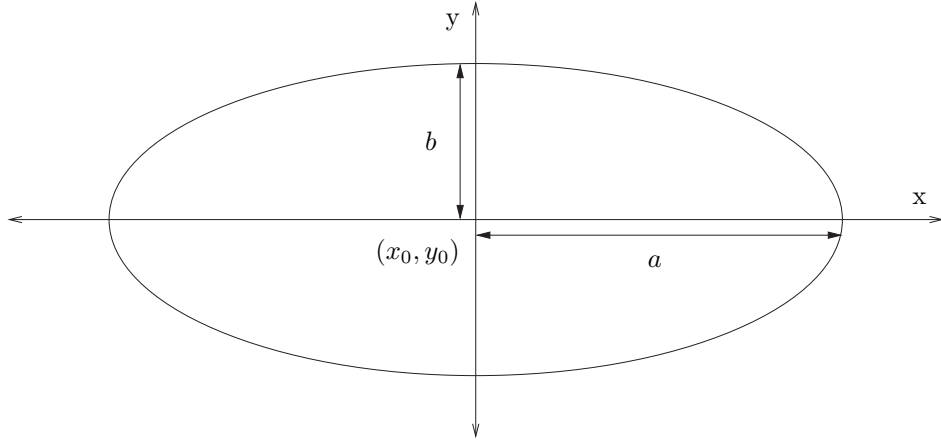


Figure 7.1: Schematic of an ellipse showing its centre (x_0, y_0) , major axis a and minor axis b .

$$u_{\text{el}}(y) = \sqrt{u_{\text{N-S}}(h)^2 - \frac{u_{\text{N-S}}(h)^2 (y - h)^2}{h^2}}. \quad (7.5)$$

Although this elliptical profile could perhaps represent a Knudsen layer shape, in that it is steeper than the parabolic function at the walls, the profile is a fixed shape constrained on the channel dimensions and a single peak velocity. Rather than replacing one profile with the other, then, it is proposed that the elliptic and parabolic profiles are combined, i.e. the parabolic Navier-Stokes velocity profile can be modified by distorting it using only some portion of the elliptical shape. A composite velocity profile with Knudsen layer features can then be produced using the original Navier-Stokes velocity profile, some proportion of the elliptical profile, and an appropriate slip velocity, which in this case will be determined by Maxwell’s slip model [10]. Such a function can expressed generally as

$$u_{\text{total}}(y) = u_{\text{N-S}}(y) + f(u_{\text{el}}(y)) + u_{\text{slip}}(0), \quad (7.6)$$

where $f(u_{\text{el}}(y))$ is a function that expresses the proportion of the elliptical profile included in the final velocity profile, and the slip velocity u_{slip} is a constant evaluated at the channel wall.

As the “correct” function $f(u_{\text{el}}(y))$ to use to replicate a true Knudsen layer

shape is not known *a priori*, a scaling factor Ω is introduced to the elliptical profile. Where the profile is scaled by a coefficient Ω_1 ,

$$u_1(y) = \Omega_1 \cdot \sqrt{u_{\text{N-S}}(h)^2 - \frac{u_{\text{N-S}}(h)^2 (y-h)^2}{h^2}}. \quad (7.7)$$

This direct relationship incorporates some proportion of a scaled elliptical shape in the final velocity profile. By scaling the elliptical profile using several different coefficients, Ω_1 , Ω_2 and Ω_3 , the likelihood of finding a satisfactory elliptical shape to add to the Navier-Stokes velocity profiles is increased. The ellipses are extended/compressed along their major axes, allowing greater flexibility in matching their shapes to a Knudsen layer velocity profile. The total proposed velocity profile for each scaled ellipse can be expressed in the general form of Eq. (7.6):

$$u_{\text{total}}(y)_1 = u_{\text{N-S}}(y) + u_1(y) + u_{\text{slip}}(0), \quad (7.8)$$

$$u_{\text{total}}(y)_2 = u_{\text{N-S}}(y) + u_2(y) + u_{\text{slip}}(0), \quad (7.9)$$

$$u_{\text{total}}(y)_3 = u_{\text{N-S}}(y) + u_3(y) + u_{\text{slip}}(0). \quad (7.10)$$

The proposed velocity profiles are then compared to that obtained using the original constitutive scaling function proposed by Lockerby *et al.* and given by Eq. (4.6) [12]. Coefficients Ω_{1-3} are found that best fit velocity profiles $u_{\text{total}}(y)_{1-3}$ to the original scaling function. These values are determined, simply by eye, to be $\Omega_1 = 0.12$, $\Omega_2 = 0.1225$ and $\Omega_3 = 0.1$. In a final implementation, the values would be chosen using an iterative goal-seeking method to produce minimum error when compared to the macroscopic quantity of interest.

Eq. (4.6) is taken to represent a true Knudsen layer shape in this initial test case. In practice, any reliable source of information about the shape of the Knudsen layer could be used for this curve-fitting process, such as DSMC data,

kinetic theory solutions or experimental results, and ideally the correct profile would be determined using data from a variety of independent sources. As the original scaling model has been validated for incompressible Poiseuille flow in channels at a variety of Kn -values, however, it is reasonable to use that function here as a first approximation to the desired Knudsen layer velocity profile [12].

Figure 7.2 shows the elliptically-scaled velocity profiles from Eqs. (7.8)–(7.10) for a Poiseuille flow where $Kn = 0.1$. The working fluid is argon gas at 300K, whose properties are determined using [75]. The flow is driven by a pressure gradient $dp/dx = -57.1536 \times 10^6 N/m^3$. In all cases Maxwell’s Eq. (3.5) using a microslip coefficient of $A_1 = 0.8$ is used to determine $u_{\text{slip}}(0)$. For convenience, the slip velocity has been calculated here using the velocity gradient of the unscaled Navier-Stokes solution at the wall, although it is anticipated that in practice the elliptical scaling method would make use of the mean-free-path-based slip implementation described in section 4.4.1. The tangential momentum accommodation coefficient, σ_U , for the velocity slip is taken to be 1.

All of the elliptically-scaled velocity profiles shown in Fig. 7.2 return the microslip velocity at the channel wall as expected, although they predict slightly different maximum velocities at the channel centre. Model 2 shows the highest peak velocity, closely followed by model 1. Mass flowrates for these velocity profiles can be calculated using Eq. (5.5). The mass flowrate obtained by integrating the analytical expression for Poiseuille flow scaled using Lockerby *et al.*’s function, Eq. (5.4), is $\dot{m} = 1.948 \times 10^{-7} kg/s$. Model 3 produces a mass flowrate for this case of $1.917 \times 10^{-7} kg/s$, which is the least accurate of the three models compared to the original constitutive scaling function. Model 2 is the most accurate in this case, with $\dot{m} = 1.949 \times 10^{-7} kg/s$, and model 1 gives $\dot{m} = 1.946 \times 10^{-7} kg/s$.

Figures 7.3–7.5 compare the elliptical velocity profiles individually to the Navier-Stokes solution for Poiseuille flow with Maxwell’s velocity slip condition, and to the constitutive scaling function proposed in [12]. In Figs. 7.3 and 7.4, elliptical models 1 and 2 match the original scaling model’s velocity gradient well

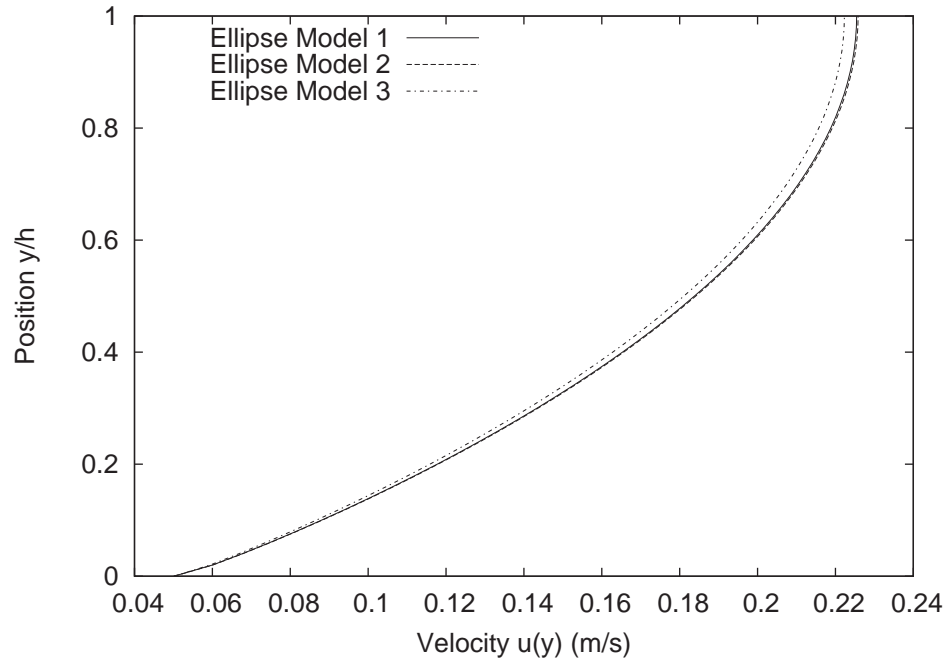


Figure 7.2: Velocity profiles from three newly proposed elliptical constitutive-scaling models for Poiseuille flow in a microchannel where $Kn = 0.1$. Position y across the channel is non-dimensionalised by the half-channel height.

in the near-wall region, up to approximately $y = 0.05$, which is roughly half of the thickness of the Knudsen layer. Further from the wall, just beyond the Knudsen layer, the elliptical models more closely resemble the Navier-Stokes slip-velocity profile, then towards the channel's centre they return to following the original scaling function. In Fig. 7.3, model 1 is closer to the N-S-F slip-velocity profile when $0.15 < y < 0.4$, whilst for model 2 in Fig. 7.4 this behaviour occurs slightly closer to the wall, where $0.1 < y < 0.3$.

Model 3, shown in Fig. 7.5, predicts a maximum velocity that lies between the slip-velocity profile and that of the original constitutive scaling function. For this $Kn = 0.1$ case, the average errors in the velocity profiles (when compared to the solution given by Eq. (5.4)) are -1.198% , -1.023% and -2.615% for models 1 – 3 respectively, which implies that all of the elliptical models underpredict the mass flowrate in the channel by a small amount.

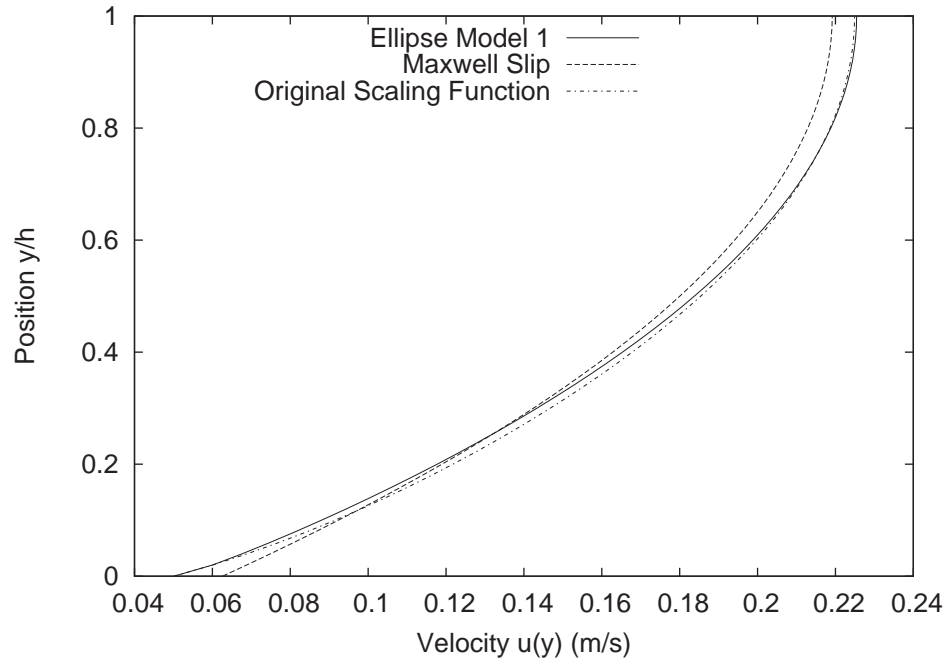


Figure 7.3: Elliptical model 1 compared to a Navier-Stokes solution with slip boundary conditions and the constitutively scaled Navier-Stokes profile given by Eq. (5.4), for Poiseuille flow in a microchannel where $Kn = 0.1$. Position y across the channel is non-dimensionalised by the half-channel height.

7.2 Extracting effective viscosity

Whilst it is true that the elliptical distortions described above can simply be added to the Navier-Stokes solution in the method outlined, if the new models are to be used in a constitutive scaling framework, it would be preferable to express them in terms of the effective viscosities with which they relate shear stress and strain-rate. Not only is this more representative of how the distorted shapes would be physically imposed on a flow, but it will also eventually enable the elliptical functions to integrate with the existing implementation of constitutive scaling in OpenFOAM.

To determine functions for effective viscosity that correspond to the elliptical models for this test case, the momentum equation is used. For 1D Poiseuille flow this is given by

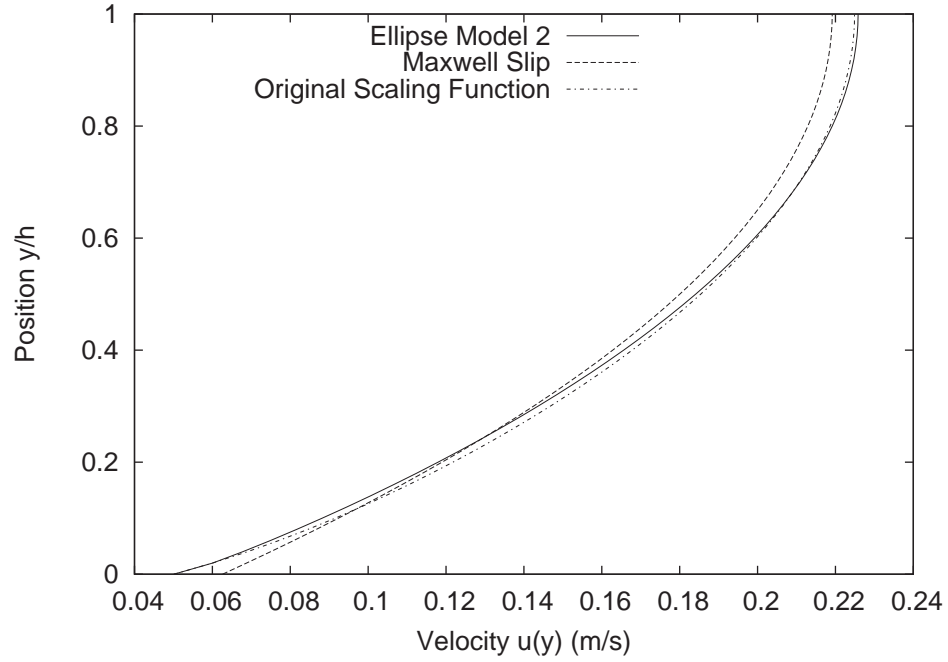


Figure 7.4: Elliptical model 2 compared to a Navier-Stokes solution with slip boundary conditions and the constitutively scaled Navier-Stokes profile given by Eq. (5.4), for Poiseuille flow in a microchannel where $Kn = 0.1$. Position y across the channel is non-dimensionalised by the half-channel height.

$$\frac{d}{dy} \left(\mu(y) \frac{du}{dy} \right) = \frac{dp}{dx}, \quad (7.11)$$

which can be solved and rearranged to find the effective viscosity as a function of the velocity gradient:

$$\mu(y) = \frac{dp/dx (y - h)}{du/dy}. \quad (7.12)$$

The velocity gradient is then obtained by differentiating the analytical expressions for the elliptical velocity profiles:

$$\frac{du}{dy}_{1-3} = \frac{d}{dy} (u_{N-S}(y)) + \frac{d}{dy} (u_{1-3}(y)) + \frac{d}{dy} (u_{slip}(0)). \quad (7.13)$$

As was the case in the original implementation of constitutive scaling, the effective viscosity is related to the actual viscosity, μ , by:

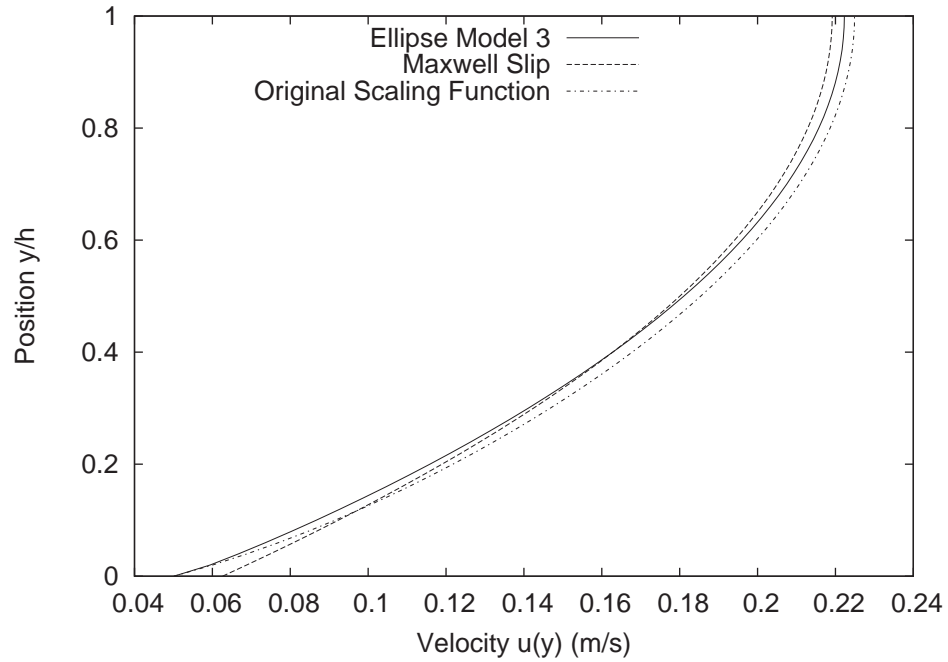


Figure 7.5: Elliptical model 3 compared to a Navier-Stokes solution with slip boundary conditions and the constitutively scaled Navier-Stokes profile given by Eq. (5.4), for Poiseuille flow in a microchannel where $Kn = 0.1$. Position y across the channel is non-dimensionalised by the half-channel height.

$$\mu(y) = \frac{\mu}{\phi}. \quad (7.14)$$

Substituting in the analytical solution to Eq. (7.13) and simplifying, the scaling function ϕ can be shown to be

$$\phi = 1 + \frac{h \cdot \Omega}{2\sqrt{-(y^2 - 2hy)}}. \quad (7.15)$$

Figure 7.6 compares the effective viscosity of elliptical models 1–3, normalised by the actual viscosity, to that of the original constitutive scaling model. What is immediately noticeable about the effective viscosity profiles is that the elliptical models and the original effective viscosity function produce quite different results. The elliptical models all have similar effective viscosities, which have much steeper gradients than the original profile, and which eventually plateau at a lower viscosity than Lockerby *et al.*'s model.

Failure to recover the original viscosity beyond the Knudsen layer region represents a weakness in the elliptical scaling models, although, the impact of the discrepancy would seem to be limited as the elliptical models produce a velocity profile that replicates the original model to within 1 – 2% average error. It is also likely that this error could be mostly eradicated using a different system of coefficients Ω_{1-3} . The reasonable mass flowrate and velocity profiles obtained from the current models suggest that the approach remains viable in spite of the differences observed in Fig. 7.6.

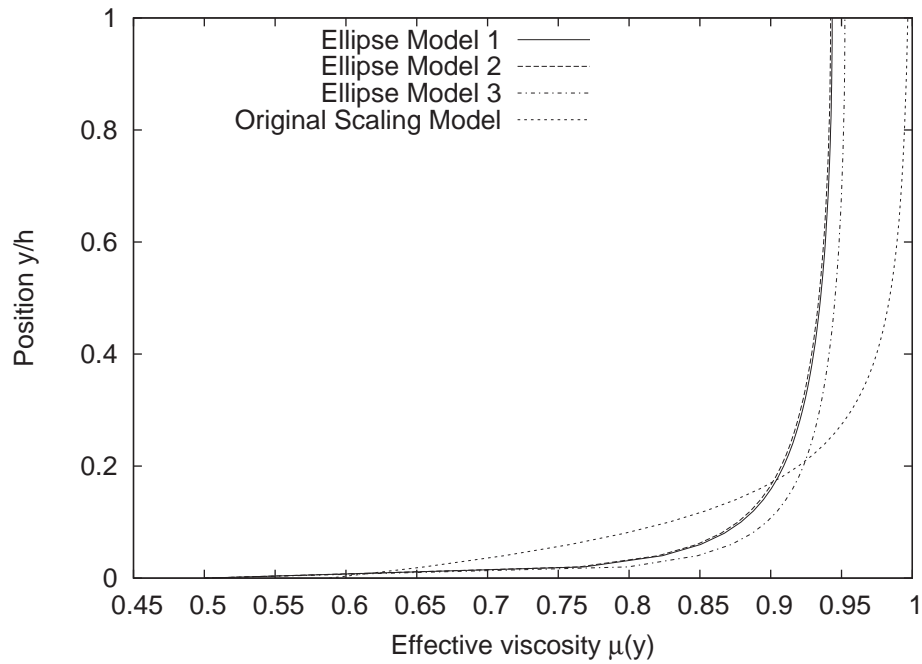


Figure 7.6: Effective viscosity for the three elliptical scaling models compared to the effective viscosity of the original constitutive scaling model. Position y across the channel is non-dimensionalised by the half-channel height.

7.3 Incorporating Kn

It has been demonstrated above that combining the equation of an ellipse with the Navier-Stokes solution for simple 1D Poiseuille flow can replicate with reasonable accuracy Knudsen layers produced by applying constitutive scaling. Effective

viscosity functions can then be extracted from these elliptically scaled models for implementation in a standard constitutive scaling process. At present, however, the new functions are independent of Kn , which limits their applicability. In order to develop these new scaling models further, it would be desirable to relate them to the degree of rarefaction in the system.

One simple method of incorporating Knudsen number is to replace the scaling coefficients Ω_{1-3} with functions of Kn . Returning to the Poiseuille flow test case above, where $Kn = 0.1$ and the Ω -coefficients were defined such that the elliptically scaled models replicated a known Knudsen layer shape for that case, it is possible to define new scaling parameters:

$$\Omega_1(Kn) = \Omega_1 \cdot Kn = 1.2Kn, \quad (7.16)$$

$$\Omega_2(Kn) = \Omega_2 \cdot Kn = 1.225Kn, \quad (7.17)$$

$$\Omega_3(Kn) = \Omega_3 \cdot Kn = Kn. \quad (7.18)$$

Introducing $\Omega(Kn)$ is an important step in the development of the elliptical effective viscosity models. With elliptical models based on system geometry, the original Navier-Stokes solution and Kn , it should be possible to capture changes in the rarefaction of the system brought on by both geometry changes and changes in the flow conditions, which is a desirable feature of a constitutive scaling scheme.

Figure 7.7 shows the absolute percentage error between the velocity profiles produced by the elliptical scaling models when $Kn = 0.1$ and the solution to Eq. (5.4) for Poiseuille flow. Based on average error, the most accurate model for this case is model 2, which has a peak error approximately one mean free path from the channel wall of 3.5%. In the centre of the channel the average error reduces to less than 0.5%. Although it is not desirable that the maximum error occurs in the Knudsen layer region, it is worth noting that the magnitude of the error is relatively small. For example, the error between the Navier-Stokes velocity

profile with slip boundaries is 25% when compared to the original constitutive scaling model in the same near-wall region.

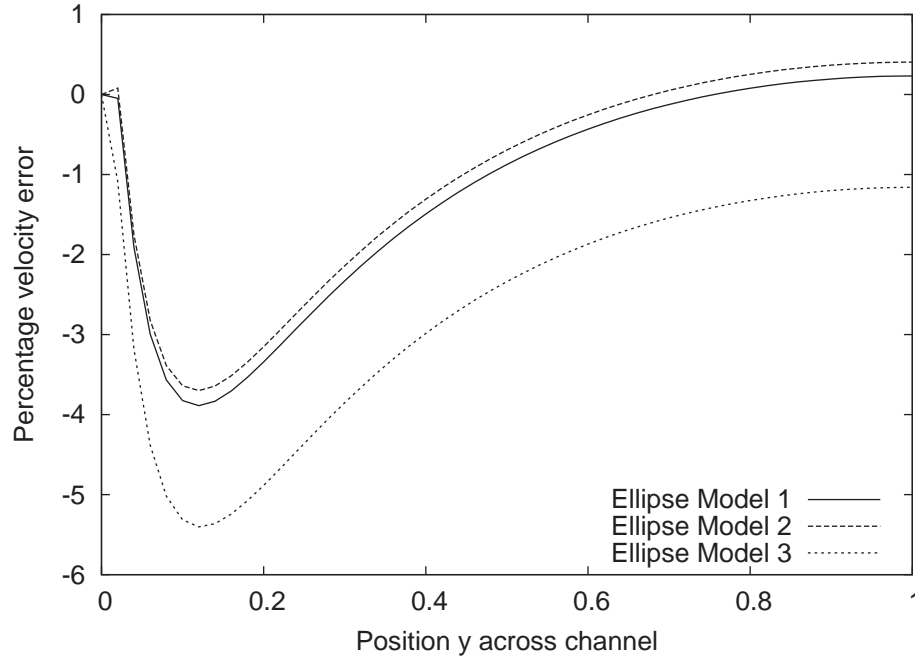


Figure 7.7: Errors between velocity profiles of elliptical scaling models and Eq. (5.4) for $Kn = 0.1$, shown at non-dimensional positions across half a microchannel whose wall is positioned at $y = 0$.

To develop an elliptical-scaling function for the Navier-Stokes equations that is valid for a range of Kn -values, the cross-channel errors between the three elliptical models and the velocity profile given by Eq. (5.4) are considered for Poiseuille flows with varying degrees of rarefaction. The elliptical models contain scaling coefficients $\Omega(Kn)_{1-3}$, and the range of Knudsen numbers analysed is $0.025 < Kn < 0.5$: the upper slip flow and lower transition flow regimes. Figure 7.8 illustrates the cross-channel error profiles when $Kn = 0.075$. Model 2 continues to produce the lowest average error in the velocity, -0.41% , however the performance of model 1 is noticeably worse than it had been for $Kn = 0.1$. In fact, as Kn changes, the velocity-profile errors produced by the three different elliptical models vary greatly.

Figure 7.9 shows the average error between the elliptical velocity profiles and

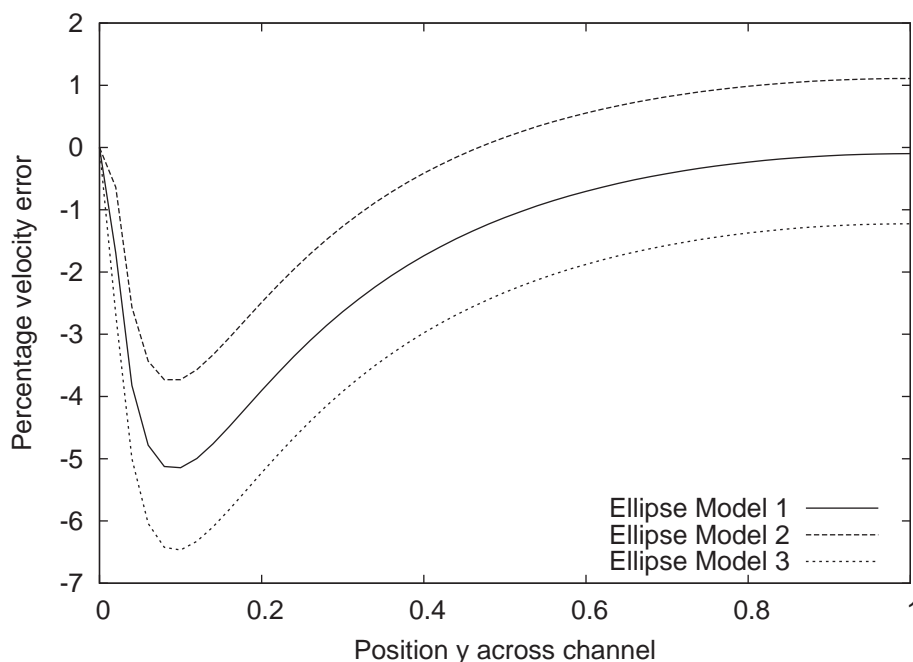


Figure 7.8: Errors between velocity profiles of elliptical scaling models and Eq. (5.4) for $Kn = 0.075$, shown at non-dimensional positions across half a microchannel whose wall is positioned at $y = 0$.

the original constitutive scaling model as Kn varies. From the figure it is clear that no single model is always the most accurate; distinct transitions occur at $Kn = 0.1, 0.2$ and 0.35 . Below $Kn = 0.1$, elliptical model 2 produces the most accurate velocity profile and, hence, mass flowrate. In the region $0.1 < Kn < 0.2$, model 1 produces a lower average error than the other profiles, but when $0.2 < Kn < 0.35$ model 3, which was the least accurate model for $Kn = 0.1$, produces the lowest average error. Finally, beyond $Kn = 0.35$, the error produced by models 1 and 3 rises whereas the error produced by model 2 reaches a steady plateau at a value of approximately -2.25% .

Although model 2 is not the most accurate model across the entire range of Kn -values studied, it produces a consistently low level of error throughout. The magnitude of the average error is also steady in the lower transitional- Kn regime, where the behaviour of the Knudsen layer has the greatest impact on the flow. The final effective viscosity expression for model 2 is given by

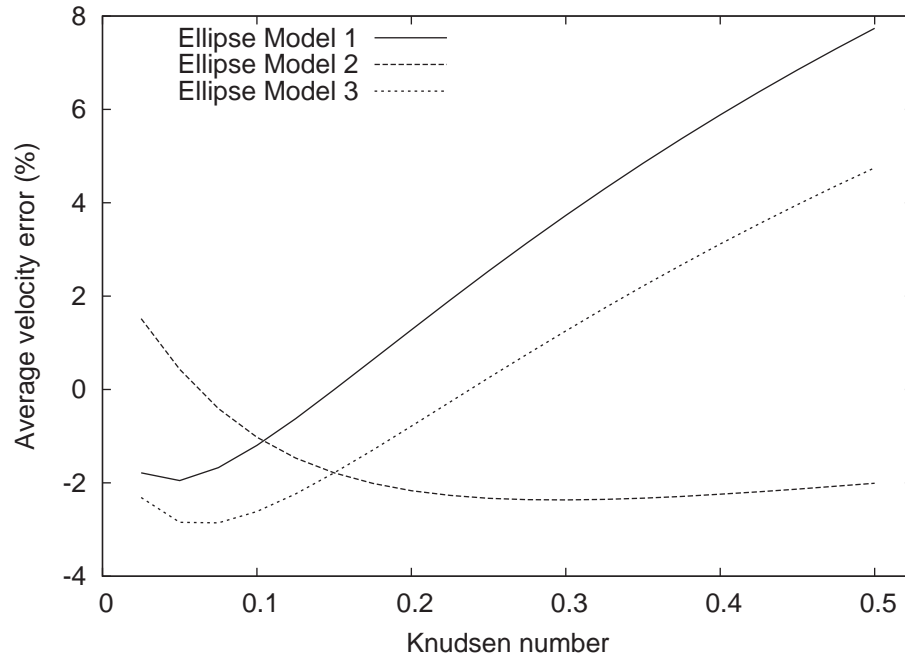


Figure 7.9: Average percentage error between velocity profiles from three elliptical scaling models and Eq. (5.4), shown versus Knudsen number, Kn .

$$\mu(y) = \mu \cdot \left(1 + \frac{h \cdot 1.225Kn}{2\sqrt{-(y^2 - 2hy)}} \right)^{-1}. \quad (7.19)$$

7.4 Discussion

Obviously this has been a preliminary case study, and in using the scaling model proposed in [12] as the target Knudsen layer shape, it has succeeded in producing only a replica of another numerical model, rather than a true Knudsen layer profile. What the exercise demonstrates, however, is that simple approximations of a Knudsen layer's shape for a given velocity profile may be used to determine reasonably accurate Knudsen layer models, which can be shown to be valid across a range of Kn values. The process produces empirical expressions, which can be based on a small amount of information on the behaviour of the rarefied flow. The proposed methodology for determining scaling functions in this manner is therefore the most promising outcome of the study.

Summary of methodology

- A simple function representative of a macroscopic field is chosen.

For cases where an N-S-F solution exists, knowledge of basic Knudsen-layer behaviour and rarefaction in the flow can be used to determine an analytical function describing how its presence would be likely to alter that field. In this case, velocity has been used as an example.

- The analytical function is related to features of the system.

In this brief study, the channel height, peak predicted velocity of the Navier-Stokes flow and Kn are used, all of which are known local parameters. The degree of rarefaction has been defined using a global Kn value in this case, but a local definition could be applied in cases where steep gradients dominate the flow [27]. In theory any quantities representative of the system could be used.

- This analytical profile is “tuned” to reflect available data.

Crucially, this stage in the process can be carried out with very little data about the rarefied flow that is to be simulated. For example, in cases where no information is known about the velocity profile, a scaled model tuned to provide a Knudsen layer could be developed to minimise errors in mass flowrate data. The resulting shape of the Knudsen layer would become less exact, but prediction of the macroscopic quantities would still likely be improved over using a straightforward slip boundary condition, and would potentially be applicable to a greater range of Kn . Admittedly this is a phenomenological means of replicating rarefaction behaviour, but such approaches are already widely used in other areas of fluid dynamics to model flow features such as turbulence and combustion [46].

In cases where more detailed data are available, the accuracy of the method can obviously be greatly improved. In this preliminary assessment the coefficients in the elliptical equations were chosen manually to represent a known velocity

profile. For a final model, these would more likely be determined using numerical methods, with emphasis on minimising the error in the macroscopic quantity of interest.

- An effective viscosity is extracted from the chosen function.

Here this has been carried out analytically, although for more complex cases the expression for the Knudsen layer shape could be differentiated numerically and the effective viscosity field would become a solved-for variable. This process would be relatively straightforward as the total function for the quantity of interest in the rarefied flow comprises only the known analytical expression for the scaling part of the function, the classical N-S-F solution to the flow and the appropriate boundary conditions.

- The effective viscosity is applied using the standard constitutive scaling approach.

As has been outlined in other areas of this thesis, constitutive scaling is now implemented in a standardised numerical framework in the OpenFOAM CFD package. New models for effective quantities can therefore be integrated using existing templates, and with minimal difficulty.

7.4.1 Scope for future work

At this early stage, the local-parameters approach to constitutive scaling has been tested only on a single example case. The methodology developed, however, has the potential to be extended to more complex flows. This should be examined thoroughly with a more detailed study.

It is important that the proposed methodology be applied to various flow configurations at a range of Kn values, in order that its practicality be assessed. In the case study above, one effective viscosity model was found to consistently produce lower average errors than the others in the lower transition regime. In

other cases, perhaps no single model would be identifiable as superior across the Kn range. This problem could be overcome using a system of charts similar to, say, a Moody diagram, which relates relative surface roughness, friction coefficient and Reynolds number in pipe flows [90]. The equivalent for a complex constitutive scaling case approached with the methodology above could be to chart a range of geometric functions, i.e. the scaled ellipses above, as they vary with both Kn and a range of appropriate scaling coefficients, $\Omega(Kn)$ in the examples above. Having chosen a function representative of the Knudsen layer in their system, the end user would then be able to find appropriate coefficients for that function based upon the Kn -range they wish to analyse. Such an outcome would require substantial literature survey and involve considerable effort if many different flow conditions were to be considered. That said, it could provide a practical means of assessing a range of standardised microflow systems, particularly if it were implemented in a computational database structure, which could self-select the most appropriate scaling functions to use based on system geometry and operating conditions.

It would also be imperative to test the applicability of this new methodology to cases of non-isothermal, compressible flow. As discussed in Chapter 6, the definition of the effective viscosity and thermal conductivity in a scaling approach can substantially affect physical quantities such as Prandtl number. Currently, maintaining Prandtl number results in a sacrifice of accuracy in curve-fitting a scaling function, see Figs. 6.4 and 6.6. More accurate scaling profiles derived from isothermal or isoflux cases, however, cannot recreate physical behaviour in systems where both energy and momentum are exchanged, as explained in sections 6.4 and 6.5. The key potential benefit of the proposed methodology over traditional constitutive scaling methods in this instance would be that the scaling functions could be defined simultaneously for cases where both energy and momentum are exchanged. For example, an experimental investigation may measure temperature profiles in a flow, but not the velocity profiles. Were simple mass flowrate data also available for the experiments, then this basic information

could be used in tandem with the temperature data to provide constitutive scaling functions for both conductivity and viscosity. This would allow an appropriate balance of energy and momentum diffusivities to be maintained, whilst improving the accuracy of the Knudsen layer shapes predicted by the scaling.

7.4.2 Summary

At this stage in its development, constitutive scaling based on the local parameters of a microsystem is not superior to existing scaling models, it merely replicates their performance for a simple test case. Potentially, however, using the local parameters of a system to inform scaling of the constitutive relations could provide a more general approach to extending the N-S-F equations for rarefied flows. The methodology proposed has the scope to include local rarefaction, which could greatly improve results for cases where the global Kn -value is secondary to local gradients in causing rarefaction. This type of flow is common in small-scale, high-speed devices such as micronozzles, which are used in many practical applications, including propulsion and control of low-mass satellites [21, 82, 83].

Another potential advantage of this new scaling approach over traditional methods is that “composite” models could be developed for complex flow systems. For example, in a compressible-flow system where narrow pipework leads to a rapidly expanding section, models that scale viscosity or thermal conductivity based only on normal distance to the nearest wall, and equilibrium mean free path, would predict that rarefaction had a decreasing impact as flow reached the expansion. In reality, steep density gradients in the rapid expansion could produce a large increase in local Knudsen number. By using a blend of scaling models, individually tuned to each geometric section of the system, the local-parameters model would be better able to emulate the behaviour of the fluid flow.

Ultimately, the limitations of this proposed methodology lie in its empirical nature. As it is not possible to define a single, straightforward expression describ-

ing the shape of a Knudsen layer for any flow configuration, initial implementation of a model based on case-by-case scaling functions would be a complicated process. This type of scaling is also dependent on the quality of information input to the system; if detailed data on Knudsen layer structure are available, then very accurate results should be possible. Where information on the rarefied flow is unavailable or unreliable, this type of approach cannot be applied with any real confidence. Bearing in mind these limitations, the fact remains that a system of deriving constitutive-scaling relationships from basic knowledge of system geometry and Knudsen layer structure, the Navier-Stokes solution to the flow and minimal data about the rarefied flow, has been successfully demonstrated here. If the success of the method could be extended beyond this initial test case, the potential exists to produce continuum models for rarefied flows applicable to many microscale configurations.

Chapter 8

Conclusions

In microsystems, the characteristic dimensions of a device can approach the mean free path of a gas flowing within it, causing the flow to become rarefied. As the flow becomes rarefied, the continuum and equilibrium assumptions of macroscale fluid dynamics begin to break down. The loss of local thermodynamic equilibrium implies that the microscopic behaviour of the gas can affect the distribution of macroscopic quantities such as velocity, temperature and pressure, resulting in large gradients in these fields. A fluid containing large gradients cannot be considered to be continuous, which violates the underlying assumptions of differential calculus and the governing equations of fluid dynamics derived from it. As such, the N-S-F equations, the traditional method of analysing fluid flow and heat transfer at the macroscale, are not suitable for gas microflows.

The Boltzmann equation and the kinetic theory of gases may be used to accurately determine the behaviour of rarefied gas flows, but are applicable in practice only to 1- and 2-dimensional problems [26]. An equivalent to solving the Boltzmann equation is to use the numerical DSMC method, which averages macroscopic field variables from deterministic simulations of molecular interactions [27]. Given sufficient computational resources, the DSMC method may be used successfully to model flows in complex, practical geometry. The limiting factor on the application of DSMC is the requirement to reduce statistical scatter to produce accurate averaged quantities. For the low-speed flows common to

microdevices, the low signal-to-noise ratio can make DSMC prohibitively computationally expensive.

As many microscale devices are currently designed by trial and error, an efficient analytical tool for engineering design applications is required. One method of achieving this aim is to extend the N-S-F equations beyond the strict limits of their applicability into the slip- and transitional- Kn flow regimes. Two key aspects of gas rarefaction that cannot be captured using continuum N-S-F simulations are boundary discontinuities and the Knudsen layer. These surface phenomena are dominant in gas microflows, where the surface area-to-volume ratio is high.

Boundary discontinuities arise when the energy and momentum of a gas flow in contact with a surface are not fully transferred to the surface. When full accommodation takes place, it leads to the no-slip condition of macroscale flow, where the velocity and temperature of the gas at a solid boundary are equivalent to the velocity and temperature of the boundary. In rarefied flows, a smaller number of intermolecular collisions take place within a given timescale. If the timescale of convective transport in the system is much shorter than the diffusive relaxation time, in which gas molecules would reach an equilibrium with the wall, then on average molecules will flow through the system without their energy and momentum ever relaxing to that of the system boundaries. A number of boundary conditions describing velocity-slip and temperature-jump phenomena are available for continuum analyses of rarefied flow. The robust phenomenological model proposed by Maxwell for velocity slip, and its equivalent proposed by Smoluchowski for temperature, are the most widely used of these boundary conditions [10, 11]. These boundary conditions are accurate in many applications if they are applied within the limits of their original derivations. For curved surfaces an extra term must be added to the slip boundary condition to describe wall-normal variation of velocity [16, 20]. When both slip and jump conditions are applied together, the assumptions implicit in the slip equation about the relative

rate of exchange of energy and momentum must be taken into account [10].

The Knudsen layer is the near-wall region one to two mean free paths thick where local thermodynamic equilibrium is not maintained between a gas and its bounding surface. This region exists in gas flows at all scales, but is significant to the macroscopic behaviour of the flow only when the length scale of the mean free path approaches the length scale of the system. The Knudsen layer is characterised by strong departures from the linear constitutive relationships of the N-S-F equations for shear stress/strain-rate and heat flux/temperature-gradient. In rarefied flows the structure of the Knudsen layer can represent a significant proportion of a flow, and consequently affect its macroscopic behaviour [37].

Constitutive scaling, which replaces viscosity and thermal conductivity with effective values, is an efficient method of incorporating non-linear Knudsen layer effects in continuum fluid dynamics simulations. Several constitutive scaling models have been proposed in the academic literature, the foremost of which are functions presented in [12] and [17].

The constitutive scaling process and both of these published models have been implemented in the open-source computational fluid dynamics package OpenFOAM [13]. This is the first time that the constitutive scaling process has been implemented in a finite-volume CFD code. OpenFOAM was identified as a suitable framework for constitutive scaling as it is both flexible and highly extensible. The hierarchical structure of the code allows for extensive modification of the governing equations within it, whilst the benefits of a general notation and a stable numerical platform are retained.

Verification exercises comparing constitutive scaling in OpenFOAM to analytical solutions for incompressible flows have been carried out. For Poiseuille flow in micro channels no-slip, slip and constitutive scaling results were compared to analytical solutions. The largest discrepancy between the analytical and numerical results was found to be 0.031%. In contrast, the commercial CFD code Fluent was found to be entirely unable to resolve slip at system boundaries

when its interpretation of Maxwell's velocity boundary condition was applied. For shear-driven Couette flows, constitutive scaling in OpenFOAM was also verified using analytical solutions, with near-perfect agreement. From these verification exercises it is possible to conclude that the constitutive scaling method has been correctly implemented in OpenFOAM for incompressible flows.

Validation case studies were also undertaken using the incompressible OpenFOAM solver. For shear-driven flows constitutive scaling was shown to capture DSMC results for both velocity slip and Knudsen layer behaviour accurately at Kn -values in the lower transition regime, and is therefore proposed for use as a design tool within conservative approximate limits of $0.01 < Kn < 0.25$. For both planar and rotating shear flows, beyond the midpoint of the transition- Kn regime at $Kn > 0.5$, the OpenFOAM model was found to improve on standard N-S-F results, but could not quantitatively model the behaviour of the flow. When applied to pressure-driven flows in microchannels with orifice plate constrictions for validation, good agreement between OpenFOAM and experimental data for centreline pressure profiles and mass flowrates was obtained. Numerical results from the solver did not match experimental data available for venturi-type constrictions in microchannels, although it was postulated that this may be due to some discrepancy in the experimental findings.

It has been shown in this thesis that the constitutive scaling method may be applied to non-isothermal, compressible flows if the relationship between effective viscosity and effective thermal conductivity is defined. Two approaches have been proposed: to use a constant Prandtl number to define scaling for conductivity based on the value of Pr and the viscosity scaling, and to use separate curve-fit relationships from kinetic theory to scale viscosity and conductivity, with the consequence that the effective Pr value will be non-constant [12, 17]. For isothermal or isoflux cases, the latter approach produces more accurate results. When both energy and momentum are simultaneously exchanged by a fluid, as they are in compressible flows, the former approach, using a constant Prandtl number

condition, was found to be more effective. Both models have been implemented in a specially-modified compressible solver in OpenFOAM, which represents the first application of constitutive scaling to compressible cases.

Constitutive scaling using a constant Prandtl number condition to determine effective viscosity was used to analyse high-speed Couette flow between parallel plates. Results were compared to DSMC data, and it was shown that for Kn -values in the lower transition regime ($0.1 < Kn < 0.25$) the OpenFOAM simulations could accurately represent available data for velocity and temperature. In this regime it is proposed that scaling model A may be used in design applications for shear-driven compressible flows with reasonable confidence, and that model B could be used similarly where flows are quiescent and thermally-driven or isothermal in nature.

When Maxwell's velocity-slip boundary condition is applied in conjunction with Smoluchowski's temperature jump condition in compressible analyses, the relative magnitude of the tangential momentum accommodation coefficient, σ_U , and the energy accommodation coefficient, σ_T , was found to be significant. When momentum accommodation was set lower than energy accommodation by 20%, an increase in the temperature of the flow was observed, as compared to a reference state where $\sigma_U = \sigma_T$. When momentum accommodation was higher than energy accommodation, the maximum temperature predicted by the energy equation was reduced. As very low accommodation coefficients have been found experimentally to apply to some materials used in microsystems ($\sim 50\%$ departure from reference value of unity), this result highlights the need for caution in selection of accommodation coefficients for gas-surface interaction.

As an alternative to existing constitutive models, which are based on the equilibrium mean free path of a gas and distance to the nearest bounding surface, a new method of defining constitutive scaling functions based on local rarefaction parameters has been proposed. A test-case of Poiseuille flow in a rectangular channel was used to demonstrate that it is possible to determine new consti-

tutive scaling functions based on Kn , the system geometry and the unscaled Navier-Stokes solution to the flow. Currently, this method only replicates the performance of existing constitutive scaling models for isothermal flow, and has not been extensively tested. The methodology proposed for defining new scaling models, however, shows promise as a means of avoiding some of the weaknesses of traditional constitutive scaling methods, such as an inability to deal with rarefaction caused by local gradients of the flow.

8.1 Research contributions

A CFD tool for incompressible gas microflows The incompressible OpenFOAM solver `microIcoFoam` has been developed and tested using data from a range of available sources including analytical solutions, DSMC and experimental results. The solver fully includes the effects of non-constant viscosity in the momentum equation and shear stress tensor, and links the velocity profile obtained by constitutive scaling correctly to Maxwell's velocity slip condition using an effective mean free path approach. Verification work has demonstrated that this model is an accurate implementation of the constitutive scaling model proposed in [12]. Validation work carried out using the verified solver has contributed to the existing body of research in providing evidence that constitutive scaling is an effective method of analysing shear- and pressure-driven flows in several microflow configurations. The implementation of constitutive scaling in OpenFOAM has allowed the approach to be applied for the first time within a general, 3D numerical framework, extending its practical applicability for use as a design tool.

A CFD tool for compressible gas microflows Two constitutive scaling models [12, 17] have been implemented and tested in a modified version of the compressible OpenFOAM solver `rhoPEsonicFoam`. It was found that the constitutive scaling model presented in [12] was more appropriate for compressible

flows, as this model preserves the ratio of momentum and energy diffusivities characterised by the Prandtl number. The OpenFOAM model was validated using DSMC data for high-speed, shear-driven flow, and was shown to be effective in the slip and lower transitional- Kn flow regimes. Although further validation would be desirable, this type of configuration is common in practical applications such as hard-disk reader heads and comb drives, and hence represents a useful assessment of the capabilities of constitutive scaling in compressible CFD.

A detailed study of the constitutive scaling method for compressible flows In developing the compressible OpenFOAM solver, a detailed study of the implications of extending constitutive scaling to compressible flows was conducted. The limitations of both available constitutive scaling functions and the velocity-slip and temperature-jump boundary conditions were explored. It was found that maintaining a constant effective Prandtl number, which implies scaling effective viscosity and thermal conductivity using the same model, produces more accurate results for temperature profiles than using a separate conductivity model accurately curve-fitted to temperature data from an isoflux case. It was also highlighted that the choice of accommodation coefficient for the slip and jump boundary conditions can influence the macroscopic properties of a flow if the values chosen are inconsistent with the assumptions of energy-exchange rate that are implicit in Maxwell's slip model. This is significant for analysis of compressible microflows as accommodation coefficients are not physical properties, but representations of particular gas-surface interactions, and are notoriously difficult to define accurately.

A new methodology for determining constitutive scaling models In order to derive new constitutive scaling models, a methodology for developing scaling functions dependent on local system parameters has been defined. A test case was used to demonstrate the basic principles of the methodology: that simple analytical functions may be superimposed on Navier-Stokes solutions to represent

rarefaction effects if the impact of rarefaction on the macroscopic fields is known. Using this methodology, it is proposed that the constitutive scaling approach could be extended to include rarefaction effects that are currently beyond its scope, such as local rarefaction caused by the steep density gradients, for example, which can occur in highly compressible rarefied flows.

8.2 Scope for future work

There are three key areas of future work that would be recommended: further development and testing of the incompressible solver, more detailed validation of the compressible solver, and further investigation of the proposed methodology for defining new constitutive scaling functions for different flow configurations.

The scope for future development of the new scaling methodology has already been discussed in detail in section 7.4.1. To summarise briefly, the methodology should be applied to a range of simple flow configurations for which good quality experimental, DSMC or kinetic-theory data are available, in order to test its generality. A system of linking scaling profiles derived for similar systems to rarefaction parameters and the necessary scaling coefficients should be developed, either in chart or database form, so that as much information as possible is retained from the testing of each flow configuration for potential future applications of the method. Following verification of its efficacy, the method should be extended to non-isothermal, compressible flows.

Future work on the compressible solver for microflows should first include more detailed validation studies using the scaling model proposed in [12], particularly for pressure-driven flows. It would also be advantageous to make use of the general framework for viscosity and conductivity scaling that has been implemented in the solver to test new constitutive models as they become available. An interesting extension of the compressible solver would be to incorporate more complex, local rarefaction effects in the scaling model, in addition to the boundary rarefaction effects of the non-equilibrium Knudsen layer.

A final suggestion for future work is that the incompressible OpenFOAM solver be extended. Specifically, it would be advantageous to be able to solve the energy equation for incompressible flows. When the solver was originally developed, specific constitutive scaling relations for thermal conductivity were unavailable, and the technique was restricted to isothermal cases. As several models have been published in recent literature, including those applied in the compressible solver, it would be possible to use the implementation methods developed in this thesis to include them in the incompressible application. This would be beneficial as it would allow detailed evaluation of constitutive scaling for thermal analysis in gas microflows to be carried out.

Appendix A

Analytical solutions: Poiseuille flow

The Navier-Stokes-Fourier equations for incompressible 2D flows of Newtonian fluids are given below. They are expressed in Cartesian form with co-ordinates (x, y, z) having velocity components (u, v, w) . Time is denoted t , density ρ , pressure p and dynamic viscosity μ .

Conservation of mass:

$$\frac{\partial(\rho u)}{\partial x} + \frac{\partial(\rho v)}{\partial y} = 0. \quad (\text{A.1})$$

Momentum in x -direction:

$$\rho \left(\frac{\partial u}{\partial t} + u \frac{\partial u}{\partial x} + v \frac{\partial u}{\partial y} \right) = -\frac{\partial p}{\partial x} + \frac{\partial}{\partial y} \left(\mu \left(\frac{\partial u}{\partial x} + \frac{\partial u}{\partial y} \right) \right). \quad (\text{A.2})$$

Momentum in y -direction:

$$\rho \left(\frac{\partial v}{\partial t} + u \frac{\partial v}{\partial x} + v \frac{\partial v}{\partial y} \right) = -\frac{\partial p}{\partial y} + \frac{\partial}{\partial y} \left(\mu \left(\frac{\partial v}{\partial x} + \frac{\partial v}{\partial y} \right) \right). \quad (\text{A.3})$$

A.1 Poiseuille flow

Isothermal Poiseuille flow in a channel, as described in section 5.2, is a one-dimensional case, as the velocity profile across the channel is constant along its length. The only term acting along the length of the channel is the pressure

gradient, dp/dx , and for incompressible Navier-Stokes solutions viscosity μ is assumed to be constant. There is no velocity in the v -direction, and no variation of the velocity in the x -direction, so, to generate an analytical solution for the velocity profile, we reduce Eqs. (A.1) and (A.2) above to

$$\begin{aligned} \frac{\partial \psi}{\partial t} + u \frac{\partial \psi}{\partial x} + v \frac{\partial u}{\partial y} &= -\frac{\partial p}{\partial x} + \frac{\partial}{\partial y} \left(\mu \left(\frac{\partial \psi}{\partial x} + \frac{\partial u}{\partial y} \right) \right), \\ \therefore \frac{\partial p}{\partial x} &= \frac{\partial}{\partial y} \left(\mu \frac{\partial u}{\partial y} \right). \end{aligned} \quad (\text{A.4})$$

If the viscosity is assumed, for now, to be constant and uniform then

$$\frac{dp}{dx} = \mu \frac{d^2 u}{dy^2},$$

which gives

$$\frac{d^2 u}{dy^2} = \frac{1}{\mu} \frac{dp}{dx}.$$

This expression is integrated to find the velocity gradient,

$$\frac{du}{dy} = \int \frac{1}{\mu} \frac{dp}{dx} dy = \frac{1}{\mu} \frac{dp}{dx} y + C_1,$$

then integrated again to determine the general expression for the velocity profile:

$$u(y) = \int \left(\frac{1}{\mu} \frac{dp}{dx} y + C_1 \right) dy = \frac{1}{\mu} \frac{dp}{dx} \frac{y^2}{2} + C_1 y + C_2. \quad (\text{A.5})$$

To obtain specific velocity profiles from this general solution, boundary conditions are applied to determine the unknown constants of integration C_1 and C_2 .

No Slip For macroscale or non-rarefied flows, the no-slip condition is applied to bounding surfaces.

At $y = 0$, $u(y) = 0$:

$$u(0) = \frac{1}{2\mu} \frac{dp}{dx} \cdot 0^2 + C_1 \cdot 0 + C_2 = 0,$$

$$\therefore C_2 = 0.$$

At $y = h$, $du/dy = 0$:

$$\frac{du}{dy} = \frac{1}{\mu} \frac{dp}{dx} h + C_1 = 0,$$

$$\therefore C_1 = \frac{-h}{\mu} \frac{dp}{dx}.$$

So, using C_1 and C_2 we find from A.5:

$$u(y) = \frac{1}{\mu} \frac{dp}{dx} \left(\frac{y^2}{2} - hy \right). \quad (\text{A.6})$$

Maxwell Slip Maxwell's expression for isothermal velocity slip is

$$u_{\text{slip}} = -A_{\text{slip}} \left(\frac{2 - \sigma_U}{\sigma_U} \right) \frac{\lambda}{\mu} \tau, \quad (\text{A.7})$$

where τ is the shear stress at the surface and λ is the mean free path of the gas.

This boundary condition is applied to Eq. (A.5).

At $y = 0$, $u(y) = u_{\text{slip}}$:

$$u(0) = \frac{1}{2\mu} \frac{dp}{dx} \cdot 0^2 + C_1 \cdot 0 + C_2 = u_{\text{slip}},$$

$$\therefore C_2 = u_{\text{slip}} = -A_{\text{slip}} \left(\frac{2 - \sigma_U}{\sigma_U} \right) \frac{\lambda}{\mu} \tau.$$

The constant C_1 is determined as above using the condition that $du/dy = 0$ at $y = h$, the channel centre, so it remains

$$C_1 = \frac{-h}{\mu} \frac{dp}{dx}.$$

These results are then substituted into Eq. (A.5) to give the Poiseuille flow velocity profile incorporating Maxwell's slip boundary condition:

$$u(y) = \frac{1}{\mu} \frac{dp}{dx} \left(\frac{y^2}{2} - hy \right) - A_{\text{slip}} \left(\frac{2 - \sigma_U}{\sigma_U} \right) \frac{\lambda}{\mu} \tau. \quad (\text{A.8})$$

Constitutive Scaling As the constitutive scaling process introduces an effective viscosity that is a function of y rather than a constant, the Poiseuille-flow velocity profile incorporating scaling must be derived assuming non-constant viscosity, i.e. from Eq. (A.4) rather than Eq. (A.5). For an effective viscosity $\mu(y)$ that varies with normal distance y away from the wall,

$$\frac{\partial}{\partial y} \left(\mu(y) \frac{\partial u}{\partial y} \right) = \frac{\partial p}{\partial x}. \quad (\text{A.9})$$

This expression is then integrated twice to find the velocity gradient du/dy and the velocity profile $u(y)$:

$$\mu(y) \frac{du}{dy} = \int \frac{dp}{dx} dy = \frac{dp}{dx} y + C_1,$$

$$\frac{du}{dy} = \frac{y}{\mu(y)} \frac{dp}{dx} + \frac{C_1}{\mu(y)},$$

$$u(y) = \int \left(\frac{y}{\mu(y)} \frac{dp}{dx} + \frac{C_1}{\mu(y)} \right) dy. \quad (\text{A.10})$$

To obtain the velocity profile from this point, an analytical expression for the effective viscosity must be known. For the model proposed in [12], the effective viscosity is given by

$$\mu(y) = \mu \left(1 + \frac{7}{10 \left(1 + \frac{y}{\lambda} \right)^3} \right)^{-1}.$$

Substituting this expression into Eq. (A.10) and integrating, the general velocity profile for constitutive scaling is produced:

$$u(y) = \frac{1}{\mu} \frac{dp}{dx} \left(\frac{y^2}{2} + \frac{7\lambda^4}{20(\lambda+y)^2} - \frac{7\lambda^3}{10(\lambda+y)} \right) + \frac{C_1}{\mu} \left(y - \frac{7\lambda}{20 \left(1 + \frac{y}{\lambda} \right)^2} \right) + C_2 \quad (\text{A.11})$$

The velocity gradient in the channel centre is used to determine the coefficient of integration C_1 as, at $y = h$, $du/dy = 0$:

$$\frac{du}{dy} = \frac{h}{\mu(y)} \frac{dp}{dx} + \frac{C_1}{\mu(y)},$$

$$\therefore C_1 = -h \frac{dp}{dx}. \quad (\text{A.12})$$

As constitutive scaling is always applied in conjunction with slip boundary conditions, Maxwell's slip function, given by Eq. (A.7), is applied at the channel walls. At $y = 0$, $u(y) = u_{\text{slip}}$:

$$u(0) = \frac{1}{\mu} \frac{dp}{dx} \left(\frac{0^2}{2} + \frac{7\lambda^4}{20(\lambda+0)^2} - \frac{7\lambda^3}{10(\lambda+0)} \right) + \frac{C_1}{\mu} \left(0 - \frac{7\lambda}{20(1+\frac{0}{\lambda})^2} \right) + C_2 = u_{\text{slip}},$$

$$\frac{1}{\mu} \frac{dp}{dx} \left(\frac{7\lambda^4}{20\lambda^2} - \frac{7\lambda^3}{10\lambda} \right) + \frac{C_1}{\mu} \left(\frac{7\lambda}{20} \right) + C_2 = u_{\text{slip}},$$

$$\therefore C_2 = -\frac{1}{\mu} \frac{dp}{dx} \left(\frac{7\lambda^4}{20\lambda^2} - \frac{7\lambda^3}{10\lambda} \right) - \frac{C_1}{\mu} \left(\frac{7\lambda}{20} \right) + u_{\text{slip}}.$$

C_2 is found by substituting the expression in Eq. (A.12) for C_1

$$C_2 = \frac{1}{\mu} \frac{dp}{dx} \left(\frac{7\lambda^2}{20} - \frac{7\lambda h}{20} \right) + u_{\text{slip}}.$$

The coefficients of integration C_1 and C_2 are then substituted into Eq. (A.11) to find the velocity profile for Poiseuille flow with constitutive scaling and Maxwell's slip boundary condition:

$$u(y) = \frac{1}{\mu} \frac{dp}{dx} \left(\frac{y^2}{2} - hy - \frac{7\lambda^2}{20} \left(\left(\frac{1 + \frac{2y}{h} - \frac{h}{\lambda}}{(1 + \frac{y}{\lambda})^2} \right) - 1 + \frac{h}{\lambda} \right) \right) - A_{\text{slip}} \left(\frac{2 - \sigma_U}{\sigma_U} \right) \frac{\lambda}{\mu} \tau. \quad (\text{A.13})$$

Appendix B

Slip-flow in Fluent

Although its makers claim that the popular CFD package Fluent has boundary conditions implemented that are suitable for assessing slip/jump Kn -regime cases, in application to microflows, the package has several key weaknesses. From the perspective of gas microflow analysis, these are

- Fluent’s use of a Lennard-Jones characteristic length scale to determine the mean free path of a gas flow,
- The calculation of slip as a fixed-value quantity at the system boundary — this is less accurate than the mixed fixed-value/fixed-gradient approach used in OpenFOAM, and
- Fluent’s numerical implementation of Maxwell slip is incorrect, leaving the package incapable of correctly predicting boundary-slip/jump.

B.1 Mean free path calculation

Maxwell’s expression for velocity slip is dependent on the equilibrium mean free path of the gas [10]. In Fluent, the equilibrium mean free path λ_F is defined for the Lennard-Jones (L-J) potential model as

$$\lambda_F = \frac{k_B T}{\sqrt{2}\pi\sigma^2 p}, \quad (\text{B.1})$$

where k_B is Boltzmann's constant, T is the gas temperature, σ is the Lennard-Jones characteristic length and p is the gas pressure [76]. The Lennard-Jones potential model is a simple description of molecular interaction with both attractive (long-range) and repulsive (short-range) parts. Whilst the Lennard-Jones potential is a reasonably accurate description of the collision behaviour of noble gases, the characteristic length scale used to define its shape must be determined by curve-fit to experimental data. This length scale corresponds to the finite distance at which the inter-particle potential reduces to zero, i.e. the end of the attractive force, a quantity for which sources of accurate experimental data are not readily available. Thus, it is likely that many users will accept the default value of L-J characteristic length scale found in Fluent. Testing carried out in [91], however, illustrates that this default value is often inappropriate and can lead to large errors in final results. For example, an 8% error in the L-J length scale translates to velocity profile errors of almost twice that magnitude. Either the implementation of another force-interaction model, or the correlation of default L-J length scales to more commonly available material properties would solve this problem effectively.

B.2 Boundary condition accuracy

In finite-volume CFD, fluid properties are calculated at grid cell-centres and these values are then extrapolated to the external faces of the cells. At system boundaries, both the method of extrapolation of data from cell centre to cell face, and the type of boundary condition applied can impact results. Common boundary condition types for face values are fixed-value, fixed-gradient and weighted fixed-value/fixed-gradient blends. The choice of boundary condition type can directly affect the performance of velocity slip/temperature jump models.

In OpenFOAM, a fixed velocity gradient $\nabla_w \mathbf{u}$ on a boundary face is evaluated using the expression

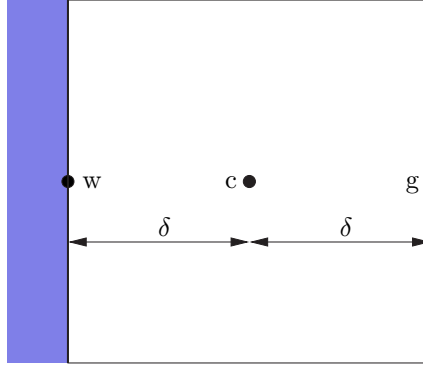


Figure B.1: Schematic of typical near-wall cell in 2D CFD.

$$\nabla_w \mathbf{u} = \frac{u_w - u_c}{\delta} |S_f|, \quad (\text{B.2})$$

where the subscripts w, c and g represent wall, cell-centre and gas values respectively, as illustrated in Fig. B.1, and S_f is the face area around the cell [69]. This expression is then rearranged to determine the gas velocity at the wall:

$$u_w = \frac{\delta}{|S_f|} \nabla_w \mathbf{u} + u_c, \quad (\text{B.3})$$

which is dependent on a fixed gradient specified by user input. In Maxwell slip, which is a mixed fixed value/fixed gradient condition, the fixed gradient value is calculated using the wall shear stress which, in turn, is calculated using the gradient of velocity field \mathbf{u} at the wall, $\nabla_w \mathbf{u}$. The shear stress is included in the main body of the solver, and is updated at each iteration of the solver. So, at each iteration a weighted blend of the fixed value and fixed gradient condition is updated, generating an accurate slip value at the wall face.

In Fluent, Maxwell's slip condition is incorporated as the Low Pressure Slip Boundary condition, and is given as [76]:

$$u_w - u_g = \frac{2 - \sigma}{\sigma} \lambda \frac{u_g - u_c}{\delta}, \quad (\text{B.4})$$

which implies that the boundary-slip value is being determined by a first order

approximation to the gradient over half of the wall-boundary cell. The boundary condition in this form is imposed by working out a gradient at each time step and extrapolating that gradient to give a fixed value (rather than a fixed gradient) at the boundary face. As the cell centre value changes, the calculated boundary-slip value will “lag” one iteration behind the cell centre and gas values. This method of implementation is considerably less accurate than the form of implementation used in OpenFOAM.

In addition, the gradient that fixes the wall-slip value in Fluent is approximated only to first order accuracy, and will hence vary directly with the cell half-width δ . Accordingly, the Fluent implementation of Maxwell slip will be very sensitive to near-wall cell size.

B.3 Maxwell’s slip condition

Further to the potential limitations in accuracy introduced by Fluent’s interpretation of Maxwell’s slip boundary condition, in practice, it can be shown that Fluent’s Low Pressure Boundary Slip condition entirely fails to represent velocity slip at system boundaries.

Although Eq. (B.4) itself is technically correct, the actual numerical implementation of the expression does not return any slip at bounding surfaces [91]. Instead, the gas velocity at the wall remains fixed at the wall speed. As illustrated in the sketched velocity profile shown in Fig. B.2, the velocity gradient between the first cell centre and the wall face is always returned by Fluent as $(u_{c_1} - u_{\text{wall}})/\delta$ rather than $(u_{c_1} - u_{\text{slip}})/\delta$. Crucially, the wall velocity u_{wall} is not equal to u_{slip} , which is the velocity of the gas at the wall. Wall velocity is a fixed constant value (most commonly zero), which is defined by the user in Fluent as part of the case setup.

As the figure illustrates, this forced reduction of the gas velocity at the wall to the fixed wall velocity that is observed in Fluent has two key effects on results [91]. Firstly, in its current form, the Low Pressure Boundary Slip condition fails

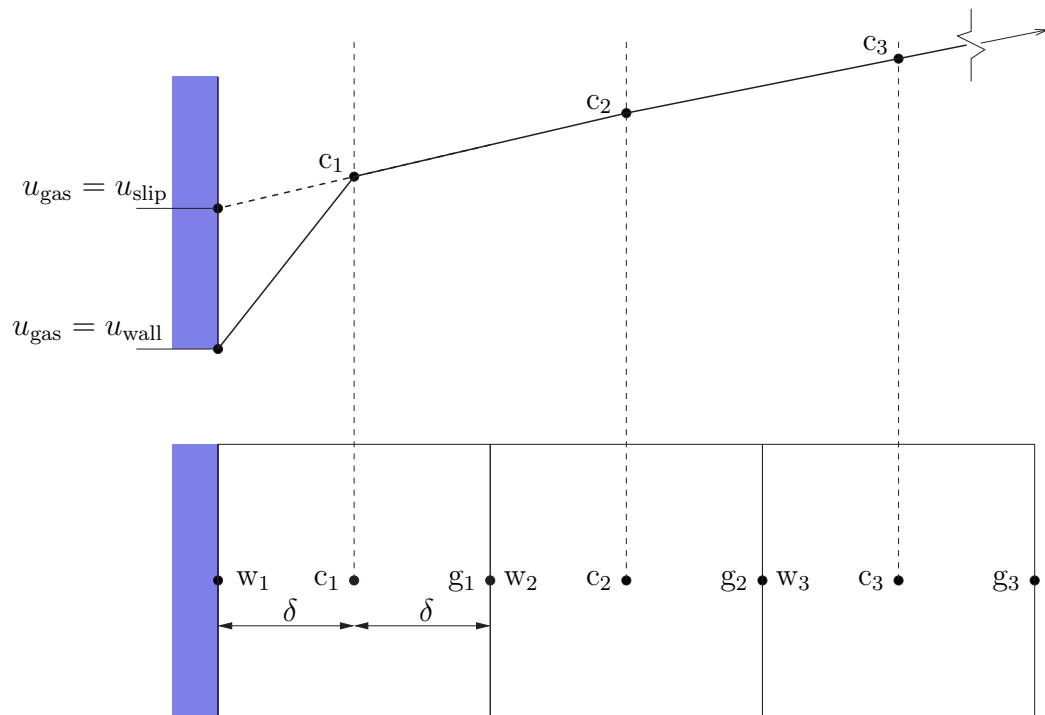


Figure B.2: Top: sketch of a typical near-wall velocity profile returned by Fluent. In the nearest cell to the wall, the velocity gradient is always manipulated in order to return the velocity of the fluid at the wall, u_{gas} , to the wall velocity, u_{wall} . This is incorrect — the gas at the wall should be assigned the calculated slip velocity u_{slip} . Bottom: arrangement of near-wall cells corresponding to the sketched velocity profile, with cell-centre positions marked.

to capture the gas slip velocity at the wall, as the gas at the wall is mistakenly assigned the velocity of the wall. This is obviously unacceptable. Secondly, in order to reduce the error in velocity profiles and mass flowrates calculated when this boundary condition is used, the size of the cell nearest the wall must be reduced until its influence on macroscopic quantities is negligible. This can significantly, and unnecessarily, increase computational expense. Ultimately, refining the computational grid near bounding surfaces reduces the impact of the error that no slip is calculated in Fluent, but it does not eradicate the primary problem that no slip velocity is recovered by Fluent at the wall.

At the most basic level velocity slip is defined as a difference in the velocity of a gas at a surface and the velocity of the surface itself, however, when this issue was raised with Fluent’s support, the following response was given — “as the wall is not moving Fluent shows zero velocity for wall” [92]. This is a serious misconception of the physics of slip flow, which leads to incorrect results being returned by Fluent when this boundary condition is used. It is intended to continue to press Fluent to resolve this issue, with the aim of having the implementation fixed in future releases of the software.

Interestingly, it is possible to work around this issue in Fluent by making use of the fixed, user-specified wall velocity. If the value of slip at the wall is calculated independently, which may or not be possible depending on flow configuration and geometry, it can be used as the fixed wall velocity. Because Fluent unfailingly reports no slip at the wall, the velocity of the gas at the wall will then be reported as the “correct” slip velocity. Obviously this is not an ideal solution, and it is not possible to implement it in all but the simplest of cases, however, it does allow Fluent to be used to analyse simple cases in the lower slip flow regime more reliably.

Appendix C

Analytical solutions: Couette flow

Couette flow in a channel, as described in section 5.3, is a one-dimensional case, as the velocity profile across the channel is constant along its length. There is no velocity in the v -direction, and no variation of the velocity in the x -direction, so, to generate an analytical solution for the velocity profile, we reduce Eqs. (A.1) and (A.2) from appendix A to

$$\begin{aligned} \frac{\partial \psi}{\partial t} + u \frac{\partial \psi}{\partial x} + v \frac{\partial u}{\partial y} &= - \frac{\partial p}{\partial x} + \frac{\partial}{\partial y} \left(\mu \left(\frac{\partial \psi}{\partial x} + \frac{\partial u}{\partial y} \right) \right), \\ \therefore \frac{\partial}{\partial y} \left(\mu \frac{\partial u}{\partial y} \right) &= 0. \end{aligned} \quad (\text{C.1})$$

If the viscosity is assumed, for now, to be constant and uniform then

$$\mu \frac{d^2 u}{dy^2} = 0.$$

This expression is integrated to find the velocity gradient,

$$\mu \int \frac{d^2 u}{dy^2} dy = \mu \frac{du}{dy} + C_1 = 0,$$

then integrated again and rearranged to determine the general expression for the velocity profile:

$$\mu \int \frac{du}{dy} dy + \int C_1 dy = \mu u(y) + C_1 y + C_2 = 0,$$

$$u(y) = -\frac{C_1 y}{\mu} - \frac{C_2}{\mu}. \quad (\text{C.2})$$

To obtain specific velocity profiles from this general solution, boundary conditions are applied to determine the unknown constants of integration C_1 and C_2 .

No Slip For macroscale or non-rarefied flows, the no-slip condition is applied to bounding surfaces, and the velocity of the gas at a wall's surface is taken to be the velocity of the wall. In the verification cases the lower wall velocity is u_1 and the upper wall velocity is u_2 , and the condition $u_1 = -u_2$ is imposed.

At $y = 0$, $u(y) = u_1$:

$$u(0) = -\frac{C_1}{\mu} \cdot 0 - \frac{C_2}{\mu} = u_1,$$

$$\therefore C_2 = -\mu u_1.$$

At $y = h$, $u(y) = 0$:

$$u(h) = -\frac{C_1}{\mu} \cdot h + u_1 = 0,$$

$$\therefore C_1 = \frac{\mu u_1}{h}.$$

So, using C_1 and C_2 we find from Eq. (C.2):

$$u(y) = u_1 \left(\frac{y}{h} - 1 \right). \quad (\text{C.3})$$

Maxwell Slip Maxwell's expression for isothermal slip velocity, u_{slip} , is given by Eq. (A.7) from appendix A. In Couette-type flows, the introduction of a slip condition dependent on the velocity gradient can become problematic, as the velocity gradient changes with the amount of slip at the wall, creating a circular dependency. As such, it is most convenient to use iterative methods to determine the correct slip at system boundaries¹, but an analytical solution given in terms of that slip velocity may still be derived.

At $y = 0$, $u(y) = u_1 + u_{\text{slip}}$, where $u_1 = -u_2$:

$$u(0) = -\frac{C_1}{\mu} \cdot 0 - \frac{C_2}{\mu} = -u_2 + u_{\text{slip}},$$

$$\therefore C_2 = \mu(u_2 - u_{\text{slip}}).$$

At $y = h$, $u(y) = 0$:

$$u(h) = -\frac{C_1}{\mu} \cdot h - (u_2 - u_{\text{slip}}) = 0,$$

$$\therefore C_1 = \frac{\mu}{h}(u_{\text{slip}} - u_2).$$

So, using C_1 and C_2 we find from Eq. (C.2):

$$u(y) = -\frac{y}{h}(u_{\text{slip}} - u_2) - (u_2 - u_{\text{slip}}),$$

$$u(y) = u_2 \left(\frac{y}{h} - 1 \right) - u_{\text{slip}} \left(\frac{y}{h} - 1 \right). \quad (\text{C.4})$$

Constitutive Scaling When constitutive scaling is applied viscosity is no longer constant and particular solutions must be derived from Eq. (C.1) with the viscosity given as a function of distance from the nearest wall, y :

¹Details of the type of numerical procedure used are given in appendix D.

$$\frac{\partial}{\partial y} \left(\mu(y) \frac{\partial u}{\partial y} \right) = 0. \quad (\text{C.5})$$

Integrating and rearranging to find an expression for the velocity gradient

$$\int \frac{d}{dy} \left(\mu(y) \frac{du}{dy} \right) dy = \mu(y) \frac{du}{dy} + C_1 = 0,$$

$$\therefore \frac{du}{dy} = -\frac{C_1}{\mu(y)}.$$

This expression is then integrated to give a general expression for the velocity profile $u(y)$:

$$u(y) = \int \frac{du}{dy} dy = -C_1 \int \frac{1}{\mu(y)} dy. \quad (\text{C.6})$$

To obtain the exact velocity profile, an analytical expression for the effective viscosity must be known. For the model proposed in [12], the effective viscosity is given by

$$\mu(y) = \frac{\mu}{f(y/\lambda)} = \mu \left(1 + \frac{7}{10 \left(1 + \frac{y}{\lambda} \right)^3} \right)^{-1}.$$

Substituting this expression into Eq. (C.6) and integrating, the general Couette flow velocity profile for constitutive scaling is produced:

$$u(y) = -\frac{C_1 y}{\mu} + \frac{7\lambda C_1}{20\mu \left(1 + \frac{y}{\lambda} \right)^2} + C_2. \quad (\text{C.7})$$

Applying a slip boundary condition at the lower channel wall, we know that at $y = 0$, $u(y) = -u_2 + u_{slip}$ (for $u_1 = -u_2$):

$$u(0) = -\frac{C_1}{\mu} \cdot 0 + \frac{7\lambda C_1}{20\mu} + C_2 = -u_s + u_{slip},$$

$$\therefore C_2 = -u_2 + u_{slip} - \frac{7\lambda C_1}{20\mu}. \quad (\text{C.8})$$

As the condition $u_1 = -u_2$ is imposed on the flow, the velocity profile must change sign at the channel centre, giving the boundary condition $u(y) = 0$ at $y = h$. Substituting Eq. (C.8) for C_2 into the general solution Eq. (C.7) gives

$$u(h) = -\frac{C_1}{\mu} \cdot h + \frac{7\lambda C_1}{20\mu \left(1 + \frac{h}{\lambda}\right)^2} - u_2 + u_{slip} - \frac{7\lambda C_1}{20\mu} = 0,$$

$$\therefore C_1 = \frac{u_2 - u_{slip}}{\left(-\frac{h}{\mu} + \frac{7\lambda}{20\mu \left(1 + \frac{h}{\lambda}\right)^2} - \frac{7\lambda}{20\mu}\right)}.$$

This result is then used in Eq. (C.8) to find C_2 :

$$C_2 = -u_2 + u_{slip} - \frac{7\lambda(u_2 - u_{slip})}{\left(-20h + \frac{7\lambda}{\left(1 + \frac{h}{\lambda}\right)^2} - 7\lambda\right)}.$$

These expressions for C_1 and C_2 are then substituted into the general expression Eq. (C.7) to find the exact solution for the velocity profile. The simplified final expression is

$$u(y) = \frac{(u_2 - u_{slip}) \left(\frac{-20y}{7\lambda} + (1 + y/\lambda)^{-2} - 1\right)}{\frac{-20h}{7\lambda} + (1 + h/\lambda)^{-2} - 1} - u_2 + u_{slip}. \quad (\text{C.9})$$

For ease of implementation in computational programmes such as Microsoft Excel (in which the analytical solutions in chapter 5 are calculated) this expression is further “simplified” to

$$u(y) = \frac{y(u_2 - u_{slip})(34\lambda^2 + 47\lambda y + 20y^2)(\lambda + h)^2}{h(\lambda + y)(34\lambda^2 + 47\lambda h + 20h)} - u_2 + u_{slip}. \quad (\text{C.10})$$

Appendix D

Microflows in Matlab

Using the Matlab programming language and numerical finite-difference schemes for differentiation, the momentum equations can be solved for simple, isothermal 1D flows including constitutive scaling [93, 94]. The major steps in this numerical process are outlined below. Outline solution procedures are given for both Couette flow and Poiseuille flow, where a common non-dimensionalisation scheme proposed in [95] is used throughout.

Non-dimensionalisation scheme

$$\begin{aligned}\hat{T} &= \frac{Tc_p}{c_1^2} & c_1^2 &= \gamma RT & \hat{y} &= \frac{p_1 y}{\mu_1 c_1} & (D.1) \\ \hat{\mu} &= \frac{\mu}{\mu_1} & \hat{p} &= \frac{p}{p_1} & \hat{u} &= \frac{u_1}{c_1} \\ \mu_1 &= \alpha T_1^s & c_p &= \frac{5}{2}R & \gamma &= \frac{5}{3}\end{aligned}$$

Quantities with “peaks” are non-dimensional, and the subscript 1 refers to a quantity at the channel wall. The velocity is directly proportional to temperature, i.e. $s = 1$ with α some constant value. The specific heat at constant pressure is c_p , R is the gas constant, c_1 is the local speed of sound at the wall and γ is the ratio of specific heats.

D.1 Couette flow

The momentum equation for planar Couette flow is expanded using the chain rule:

$$\frac{d}{dy} \left(\mu \frac{du}{dy} \right) = \frac{d\mu}{dy} \frac{du}{dy} + \mu \frac{d^2u}{dy^2} = 0. \quad (\text{D.2})$$

Using the scheme above, this expression may be non-dimensionalised to

$$\frac{d\hat{T}}{d\hat{y}} \frac{d\hat{u}}{d\hat{y}} + \hat{T} \frac{d^2\hat{u}}{d\hat{y}^2} = 0. \quad (\text{D.3})$$

First-order finite difference schemes are then used to represent $d\hat{u}/d\hat{y}$ and $d^2\hat{u}/d\hat{y}^2$:

$$\frac{d\hat{u}}{d\hat{y}} = \frac{u_{i+1} - u_{i-1}}{2d\hat{y}},$$

$$\frac{d^2\hat{u}}{d\hat{y}^2} = \frac{u_{i+1} - 2u_i + u_{i-1}}{d\hat{y}^2},$$

where u_i represents the velocity at the i^{th} node on a regular grid, and $d\hat{y}$ the height of the channel. These expressions are substituted into Eq. (D.3), which is then rearranged in terms of the velocities at each node:

$$u_{i-1} \left(\frac{-d\hat{T}}{d\hat{y}} \frac{1}{2d\hat{y}} + \frac{\hat{T}}{d\hat{y}^2} \right) + u_i \left(\frac{-2\hat{T}}{d\hat{y}^2} \right) + u_{i+1} \left(\frac{d\hat{T}}{d\hat{y}} \frac{1}{2d\hat{y}} + \frac{\hat{T}}{d\hat{y}^2} \right) = 0. \quad (\text{D.4})$$

The coefficients of the velocities contain terms in \hat{T} and $d\hat{T}/d\hat{y}$. Using the non-dimensionalisation scheme above, the dimensionless temperature at the channel walls is found to be a constant, $\hat{T} = 3/2$ for monoatomic gases. The temperature gradient is determined using a first-order finite difference scheme similar to that used for to describe the velocity gradient. The node velocities are then determined by multiplying a matrix of boundary conditions $[b]$, which is zero at all nodes except the wall nodes, by the inverse of the matrix of coefficients, $[A]$:

$$[u] = [A]^{-1} [b]. \quad (\text{D.5})$$

The boundary condition matrix is zero for all non-wall nodes, and for no-slip Couette flow, includes only $b = V$ at the moving wall and $b = 0$ at the stationary wall as boundary values. For example, for a Couette flow case across a single node i bounded by $i - 1$ and $i + 1$, we would see

$$\begin{bmatrix} u_{i-1} \\ u_i \\ u_{i+1} \end{bmatrix} \begin{bmatrix} A_{i-1} & A_i & A_{i+1} \end{bmatrix} \begin{bmatrix} b_{i-1} = 0 \\ b_i \\ b_{i+1} = V. \end{bmatrix}$$

To modify the solution to include slip, only the boundary conditions are changed, i.e. $b_{i-1} = u_{\text{slip}}$ and $b_{i+1} = V - u_{\text{slip}}$.

It is also possible to include the effects of constitutive scaling in these Matlab solutions, by replacing the implicitly linear expression for shear stress with a scaled function. In Couette flow, the velocity gradient at any point in the flow may be expressed in terms of shear stress,

$$\frac{du}{dy} = \frac{-\tau}{\mu} = \frac{-\mu V}{2h}, \quad (\text{D.6})$$

where h is the channel height. Constitutive scaling operates on the relationship between shear stress and strain rate, hence, Eq. (D.6) may be scaled using

$$\frac{du}{dy} = \frac{-\tau\psi}{\mu} = \frac{-\tau}{\mu} \left(1 + \frac{7}{10 \left(1 + \frac{y}{\lambda} \right)^3} \right), \quad (\text{D.7})$$

where ψ represents the scaling function proposed in [12]. This expression for the velocity gradient is then substituted into Eq. (D.3), giving

$$\frac{d\hat{T}}{d\hat{y}} \left(\frac{-\tau\psi}{\mu} \right) + \hat{T} \left(\frac{d}{d\hat{y}} \left(\frac{-\tau\psi}{\mu} \right) \right) = 0. \quad (\text{D.8})$$

The Couette flow shear stress, τ , and the constitutive scaling function are then substituted into Eq. (D.8), and the equation is rearranged to give an expression for $d\hat{T}/d\hat{y}$:

$$\frac{d\hat{T}}{d\hat{y}} = \frac{21V\hat{T}}{10h \left(1 + \frac{y}{\lambda}\right)^4 \lambda \left(\frac{V}{2h} + \frac{7V}{20h\left(1 + \frac{y}{\lambda}\right)^3}\right)} \quad (\text{D.9})$$

When this expression is used in place of a finite-difference scheme for $d\hat{T}/d\hat{y}$ in the matrix of coefficients $[A]$, by substitution into Eq. (D.4), constitutive scaling is successfully integrated into the velocity profile.

D.2 Poiseuille flow

Following a process similar to that outlined above, constitutively-scaled Poiseuille flow can also be analysed in Matlab. The dimensionless momentum equation for this case is

$$\hat{\mu} \frac{d^2 \hat{u}}{d\hat{y}^2} + \frac{d\hat{\mu}}{d\hat{y}} \frac{d\hat{u}}{d\hat{y}} = \frac{d\hat{p}}{d\hat{x}}, \quad (\text{D.10})$$

where \hat{x} is the dimensionless length of the channel. Replacing $\hat{T} = 3/2$ and $\hat{\mu} = \frac{2}{3}\hat{T}$, and using a first order finite difference scheme for the velocity gradient we have

$$\hat{T} \left(\frac{u_{i+1} - 2u_i + u_{i-1}}{d\hat{y}^2} \right) + \frac{d\hat{T}}{d\hat{y}} \left(\frac{u_{i+1} - u_{i-1}}{2d\hat{y}} \right) = \frac{3}{2} \frac{d\hat{p}}{d\hat{x}}. \quad (\text{D.11})$$

This expression is then rearranged to find the velocity coefficients:

$$u_{i-1} \left(\frac{\hat{T}}{d\hat{y}^2} - \frac{d\hat{T}}{d\hat{y}} \frac{1}{2d\hat{y}} \right) + u_i \left(\frac{-2\hat{T}}{d\hat{y}^2} \right) + u_{i+1} \left(\frac{\hat{T}}{d\hat{y}^2} + \frac{d\hat{T}}{d\hat{y}} \frac{1}{2d\hat{y}} \right) = \frac{3}{2} \frac{d\hat{p}}{d\hat{x}}. \quad (\text{D.12})$$

The constitutively-scaled velocity gradient for 1D Poiseuille flow is given by

$$\frac{du}{dy} = \frac{-\tau\psi}{\mu} = \frac{1}{\mu} \frac{dp}{dx} (y - h) \left(1 + \frac{7}{10 \left(1 + \frac{y}{\lambda}\right)^3} \right), \quad (\text{D.13})$$

where ψ again represents the scaling function proposed in [12]. This expression is substituted into Eq. (D.10), which can then be rearranged to give an expression for $d\hat{T}/d\hat{y}$. This is then substituted in turn into Eq. (D.12) to integrate constitutive scaling into the final velocity profile.

The primary advantages of using Matlab to integrate constitutive scaling in numerical models are that it is relatively straightforward to accomplish for cases whose analytical solutions are known, and allows flow conditions/geometry to be varied quickly and simply to analyse different “analytical” cases for verification. The method can also be applied to the energy equation for these simple 1D flows, allowing thermal analyses to be conducted. The obvious disadvantage of this approach is that analytical solutions to the problem must be used to generate the results, ruling out its use in all but the simplest of cases. Also, for the end user, the procedures followed to integrate constitutive scaling in Matlab are vastly more complex than simply choosing to apply constitutive scaling in a CFD package, which further limits the applicability of these finite-difference models for engineering applications.

References

- [1] A.H. Epstein, S.D.Senturia, O. Al-Midani, G. Anathasuresh, A. Ayon, K. Breuer, K.S. Chen, F.F. Ehrich, E. Esteve, and L. Frechette. Micro-heat engines, gas turbines and rocket engines — the MIT microengine project. *Proceedings of AIAA Fluid Dynamics Conference, CO, USA, AIAA-1997-1773*, 1997.
- [2] M. Gad el Hak. The fluid mechanics of microdevices — The Freeman Scholar lecture. *Journal of Fluids Engineering*, 121:5–33, 1999.
- [3] C. Cercignani. *Mathematical Methods in Kinetic Theory*. Plenum Press, 2nd edition, 1990.
- [4] S.K. Loyalka. Temperature jump: rigid-sphere gas with arbitrary gas/surface interaction. *Nuclear Science and Engineering*, 108:69–73, 1991.
- [5] C. Cercignani and M. Lampis. Kinetic model for gas-surface interaction. *Transport Theory and Statistical Physics*, 1:101–114, 1971.
- [6] C. Cercignani. *Knudsen Layers: Theory and Experiment*, in *Recent Developments in Theoretical and Experimental Fluid Dynamics*, U. Muller, K.G. Rosner and B. Schmidt eds. Springer-Verlag, 1979.
- [7] M.N. Kogan. *Rarefied Gas Dynamics*. Plenum Press, 1969.
- [8] E.H. Kennard. *Kinetic Theory of Gases*. McGraw-Hill Book Company Inc., 1938.

- [9] S. Chapman and T.G. Cowling. *The Mathematical Theory of Non-Uniform Gases*. Cambridge University Press, 1970.
- [10] J.C. Maxwell. On stresses in rarified gases arising from inequalities of temperature. *Philosophical Transactions of the Royal Society of London, Part 1*, 170:231–256, 1879.
- [11] M. von Smoluchowski. Über wärmeleitung in verdünnten gasen. *Annalen der Physik und Chemie*, 64:101–130, 1898.
- [12] D.A. Lockerby, J.M. Reese, and M.A. Gallis. Capturing the Knudsen layer in continuum-fluid models of nonequilibrium gas flows. *AIAA Journal*, 43(6):1391–1393, 2005.
- [13] OpenFOAM. <http://www.openfoam.org>.
- [14] L. O’Hare, T.J. Scanlon, and J.M. Reese. Gas flow through microscale orifice plates. *Proceedings of ASME ICNMM2006, Limerick, Ireland, ICNMM2006–96193*, 2006.
- [15] K.W. Tibbs, F. Baras, and A.L. Garcia. Isothermal slip flow over curved surfaces. *Physical Review E*, 56:2282–2283, 1997.
- [16] D.A. Lockerby, J.M. Reese, D.R. Emerson, and R.W. Barber. Velocity boundary condition at solid walls in rarefied gas calculations. *Physical Review E*, 70:017303, 2004.
- [17] J.M. Reese, Y. Zheng, and D.A. Lockerby. Computing the near-wall region in gas micro- and nanofluidics: critical Knudsen layer phenomena. *Journal of Computational and Theoretical Nanoscience*, 4(4):807–813, 2007.
- [18] H. Xue, H. Ji, and C. Shu. Prediction of flow and heat transfer characteristics in micro-Couette flow. *Microscale Thermophysical Engineering*, 7:51–68, 2003.

- [19] J.C. Maxwell. On the dynamical theory of gases. *Philosophical Transactions of the Royal Society of London*, 157:49–88, 1867.
- [20] R.W. Barber, Y. Sun, X.J. Gu, and D.R. Emerson. Isothermal slip flow over curved surfaces. *Vacuum*, 76:73–81, 2004.
- [21] G.E. Karniadakis and A. Beskok. *Micro Flows: Fundamentals and Simulation*. Springer, 2002.
- [22] L. O’Hare and J.M. Reese. Numerical models of gas flow and heat transfer in microscale channels: capturing rarefaction behaviour using a constitutive scaling approach. *Proceedings of ASME ICNMM2007, Puebla, Mexico*, ICNMM2007–30097, 2007.
- [23] J.M. Reese, M.A. Gallis, and D.A. Lockerby. New directions in fluid dynamics: non-equilibrium aerodynamic and microsystem flows. *Philosophical Transactions of the Royal Society of London A*, 361:2967–2988, 2003.
- [24] P.L. Bhatnagar, E.P. Gross, and M. Krook. A model for collision processes in gases i. small amplitude processes in charged and neutral one-component systems. *Physical Review*, 94(3):511–525, 1954.
- [25] A. Frangi, A. Frezzotti, and S. Lorenzani. On the application of the BGK kinetic model to the analysis of gas-structure interactions in MEMS. *Computers and Structures*, 85:810–817, 2007.
- [26] C. Cercignani. *Rarefied Gas Dynamics: From Basic Concepts to Actual Calculations*. Cambridge University Press, 2001.
- [27] G.A. Bird. *Molecular Gas Dynamics and the Direct Simulation of Gas Flows*. Clarendon Press, 1994.
- [28] W. Wagner. A convergence proof for Bird’s direct simulation Monte Carlo method for the Boltzmann equation. *Journal of Statistical Physics*, 66:1011–1044, 1992.

- [29] L.L. Baker and N.G. Hadjiconstantinou. Variance reduction for Monte Carlo solutions of the Boltzmann equation. *Physics of Fluids*, 17:051703, 2005.
- [30] J.N. Moss, R.N. Gupta, and J.M. Price. DSMC simulations of OREX entry conditions. NASA Technical Note 111621, NASA, 1995.
- [31] J.N. Moss, R.N. Gupta, and J.M. Price. DSMC simulations of Apollo capsule aerodynamics for hypersonic rarefied conditions. *Proceedings of 9th AIAA ASME Joint Thermophysics and Heat Transfer Conference, San Francisco, CA, USA*, AIAA Paper 2006-3577, 2006.
- [32] D. Burnett. The distribution of molecular velocities and the mean motion in a non-uniform gas. *Proceedings of the London Mathematical Society*, 40:382–435, 1935.
- [33] R. Balakrishnan. An approach to entropy consistency in second order hydrodynamic equations. *Journal of Fluid Mechanics*, 503:201–245, 2004.
- [34] X. Zhong, R.W. MacCormack, and D.R. Chapman. Stabilization of the Burnett equations and application to hypersonic flows. *AIAA Journal*, 31:1036–1043, 1993.
- [35] S. Jin and M. Slemrod. Regularization of the Burnett equations via relaxation. *Journal of Statistical Physics*, 103:1009–1033, 2001.
- [36] L. O’Hare, D.A. Lockerby, J.M. Reese, and D.R. Emerson. Near-wall effects in rarefied gas micro-flows: some modern hydrodynamic approaches. *International Journal of Heat and Fluid Flow*, 28:37–43, 2007.
- [37] D.A. Lockerby, J.M. Reese, and M.A. Gallis. The usefulness of higher-order constitutive relations for describing the Knudsen layer. *Physics of Fluids*, 17:100609, 2005.
- [38] H. Grad. On the kinetic theory of rarefied gases. *Communications on Pure and Applied Mathematics*, 2:331–407, 1949.

- [39] H. Struchtrup. Some remarks on the equations of Burnett and Grad. *Transport in Transition Regimes*, IMA Volume 135, Springer, 2003.
- [40] S. Mizzi, R.W. Barber, D.R. Emerson, J.M. Reese, and S.K. Stefanov. A phenomenological and extended continuum approach for modelling non-equilibrium flows. *Continuum Mechanics and Thermodynamics*, 19(5):273–283, 2007.
- [41] H. Struchtrup and M.Torrilhon. Regularization of Grad’s 13 moment equations: derivation and linear analysis. *Physics of Fluids*, 15(9):2668–2680, 2003.
- [42] T. Thatcher, Y. Zheng, and H. Struchtrup. Boundary conditions for Grad’s 13 moment equations. Accepted for publication in *Progress in Computational Fluid Dynamics*, 2007.
- [43] M.Torrilhon and H. Struchtrup. Boundary conditions for regularized 13-moment equations for micro-channel-flows. *Journal of Computational Physics*, (227):1982–2011, 2008.
- [44] M.Torrilhon and H. Struchtrup. Gas micro-flow modeling based on regularized 13 moment equations. *Proceedings of MNHT 2008, ASME Micro/Nanoscale Heat Transfer International Conference, Tainan, Taiwan*, (MNHT2008-52274), 2008.
- [45] Y. Zheng, J.M. Reese, T.J. Scanlon, and D.A. Lockerby. Scaled Navier-Stokes-Fourier equations for rarefied gas flow and heat transfer phenomena in micro- and nanosystems. *Proceedings of ASME ICNMM2006, Limerick, Ireland*, ICNMM2006–96066, 2006.
- [46] H.K. Versteeg and W. Malalasekera. *An Introduction to Computational Fluid Dynamics: The Finite Volume Method*. Pearson Prentice Hall, 2nd edition, 2007.

- [47] Kundt and Warburg. Ueber reibung und wärmeleitung verdünnter gase. *Annalen der Physik und Chemie*, 155:337–366, 1875.
- [48] R.M. Inman. Heat transfer for laminar slip flow of a rarefied gas between parallel plates with unsymmetrical wall heat flux. NASA Technical Note D-2421, NASA, 1964.
- [49] L. O’Hare, J.M. Reese, and T.J. Scanlon. Evaluating constitutive scaling models for application to compressible microflows. *International Journal of Heat and Mass Transfer*, (51):1281–1292, 2008.
- [50] F. Sharipov. Application of the Cercignani-Lampis scattering kernel to calculations of rarefied gas flows. II. Slip and jump coefficients. *European Journal of Mechanics B/Fluids*, 22:133–143, 2003.
- [51] I. Langmuir. Surface chemistry. *Chemical Review*, 13(2):147–191, 1933.
- [52] R.S. Myong, J.M. Reese, R.W. Barber, and D.R. Emerson. Velocity slip in microscale cylindrical Couette flow: the Langmuir model. *Physics of Fluids*, 17:087105, 2005.
- [53] S. Yuhong, W.K. Chan, and L. Ningyu. A slip model with molecular dynamics. *Journal of Micromechanics and Microengineering*, 12(3):316–322, 2002.
- [54] S.A. Schaaf and P.L. Chambre. *Flow of Rarefied Gases*. Princeton University Press, 1961.
- [55] C. Cercignani. Higher order slip according to the linearized Boltzmann equation. Institute of Engineering Research Report AS-64-19, UCLA, Berkeley, 1964.
- [56] N.G. Hadjiconstantinou. Comment on Cercignani’s second-order slip coefficient. *Physics of Fluids*, 15(8):2352–2354, 2003.

- [57] R.G. Deissler. An analysis of second-order slip flow and temperature jump boundary conditions for rarefied gases. *International Journal of Heat and Mass Transfer*, 7:681–694, 1964.
- [58] C. Aubert and S. Colin. High-order boundary conditions for gaseous flows in rectangular microducts. *Microscale Thermophysical Engineering*, 5(1):41–54, 2001.
- [59] D.A. Lockerby and J.M. Reese. Near-wall scaling of the Navier-Stokes constitutive relations for accurate micro gas flow simulations. *Proceedings of ASME ICNMM2007, Puebla, Mexico*, ICNMM2007–30061, 2007.
- [60] W. Gaede. The external friction of gases. *Annalen der Physik*, 41(7):289–336, 1913.
- [61] M. Knudsen. Molecular current of hydrogen through channels and the heat conductor manometer. *Annalen der Physik*, 35(7):389–396, 1911.
- [62] M. Fichman and G. Hetsroni. Viscosity and slip in gas flow in microchannels. *Physics of Fluids*, 17:123102, 2005.
- [63] C.R. Lilley and J.E. Sader. Velocity gradient singularity and structure of the velocity profile in the Knudsen layer according to the Boltzmann equation. *Physical Review E*, 76:026315, 2007.
- [64] T. Ohwada, Y. Sone, and K. Aoki. Numerical analysis of the shear and thermal creep flows of a rarefied gas over a plane wall on the basis of the linearized Boltzmann equation for hard-sphere molecules. *Physics of Fluids A: Fluid Dynamics*, 1(9):1588–1599, 1989.
- [65] S.K. Loyalka and K.A. Hickey. Velocity slip and defect: hard sphere gas. *Physics of Fluids A: Fluid Dynamics*, 1(3):612–614, 1989.

- [66] S.K. Loyalka and K.A. Hickey. The Kramers problem: velocity slip and defect for a hard sphere gas with arbitrary accommodation. *Zeitschrift für Angewandte Mathematik und Physik (ZAMP)*, 41(2):245–253, 1990.
- [67] S.K. Loyalka and K.A. Hickey. Unified solutions to classical flow problems based on the BGK model. *Zeitschrift für Angewandte Mathematik und Physik (ZAMP)*, 54(3):517–534, 2001.
- [68] C. Cercignani, A. Frangi, S. Lorenzani, and B. Vigna. BEM approaches and simplified kinetic models for the analysis of damping in deformable MEMS. *Engineering Analysis with Boundary Elements*, 31:451–457, 2007.
- [69] OpenFOAM 1.4.1 Programmer’s Guide. <http://www.openfoam.org>, 2007.
- [70] OpenFOAM 1.4.1 User Guide. <http://www.openfoam.org>, 2007.
- [71] C.J. Greenshields. Notes on the nonequilibrium hypersonic flow project. Technical report, University of Strathclyde, 2006.
- [72] D.A. Lockerby. Matlab files for calculating Couette and Poiseuille flows with modified constitutive-relations. *Personal communication*, 2004–2005.
- [73] Guide for the validation and verification of computational fluid dynamics simulations. AIAA guide, 1998.
- [74] A. Beskok, G.E. Karniadakis, and W. Trimmer. Rarefaction and compressibility effects in gas microflows. *Journals of Fluids Engineering*, 118:448–456, 1996.
- [75] G.F.C. Rogers and Y.R. Mayhew. *Thermodynamic and Transport Properties of Fluids*. Blackwell, 5th edition, 1995.
- [76] Fluent. *Fluent 6.3 User’s Guide — 14.2.2 Theory*. Fluent Inc.

- [77] M.J. McNenly, M.A. Gallis, and I.D. Boyd. Empirical slip and viscosity model performance for microscale gas flow. *International Journal for Numerical Methods in Fluids*, 49:1169–1191, 2005.
- [78] X. Li, W.Y. Lee, M. Wong, and Y. Zohar. Gas flow in constriction microdevices. *Sensors and Actuators*, 83:277–283, 2000.
- [79] E.B. Arkilic. *Measurement of the mass flow and tangential momentum accommodation coefficient in silicon micromachined channels*. PhD thesis, M.I.T., 1997.
- [80] E.B. Arkilic, M.A. Schmidt, and K.S. Breuer. Gaseous slip flow in long microchannels. *Microelectromechanical Systems*, (6):167–178, 1997.
- [81] S. Colin. Rarefaction and compressibility effects on steady and transient gas flows in microchannels. *Microfluid Nanofluid*, 1:268–279, 2005.
- [82] P.F. Hao, Y.T. Ding, Z.H. Yao, F. He, and K.Q. Zhu. Size effect on gas flow in micro nozzles. *Journal of Micromechanics and Microengineering*, 15:2069–2073, 2005.
- [83] M. Buoni, D. Dietz, K. Aslam, and V.V. Subramaniam. Simulation of compressible gas flow in a micronozzle: Effects of walls on shock structure. *35th AIAA Thermophysics Conference, Anaheim, CA, USA*, AIAA – 2001 – 3073, 2001.
- [84] C.J. Greenshields and J.M. Reese. Some consequences of non-local-equilibrium in hypersonic aerodynamic flows. *Proceedings of European Conference for Aerospace Sciences (EUCASS), Moscow, Russia*, Symposium 2: 2.10.03, 2005.
- [85] F.M. White. *Fluid Mechanics*. McGraw-Hill Professional, 2003.

- [86] L. Mieussens and H. Struchtrup. Numerical comparison of Bhatnagar-Gross-Krook models with proper Prandtl number. *Physics of Fluids*, 16(8):2797–2813, 2004.
- [87] D.J. Rader, J.N. Castaneda, J.R. Torczynski, T.W. Grasser, and W.M. Trott. Measurements of thermal accommodation coefficients. Technical report, Sandia National Laboratories, 2005.
- [88] K. Nanbu. Analysis of the Couette flow by means of the new direct-simulation method. *Journal of the Physical Society of Japan*, 52:1602–1608, 1983.
- [89] S.M. Cooper, B.A. Cruden, M. Meyyappan, R. Raju, and S. Roy. Gas transport characteristics through a carbon nanotubule. *Nano Letters*, 4(2):377–381, 2004.
- [90] B.R. Munson, D.F. Young, and T.H. Okiishi. *Fundamentals of Fluid Mechanics*. John Wiley, third edition, 1998.
- [91] W. Nicholls and L. O’Hare. Fluent slip model performance for micro-scale Poiseuille and Couette flow. Technical report, University of Strathclyde, 2007.
- [92] Fluent Inc. Re: Low pressure slip. E-mail communication with Fluent technical support, August 2007.
- [93] Matlab. <http://www.mathworks.com>.
- [94] S.C. Chapra and R. Canale. *Numerical Methods for Engineers: With Software and Programming Applications*. McGraw-Hill Higher Education, 4th edition, 2001.
- [95] D.A. Lockerby and J.M. Reese. High-resolution Burnett simulations of micro Couette flow and heat transfer. *Journal of Computational Physics*, 188(2):333–347, 2003.